A study on buoyancy-driven flows: Using particle image velocimetry for validating the Fire Dynamics Simulator

Andreas Meunders

Member of the Helmholtz Association

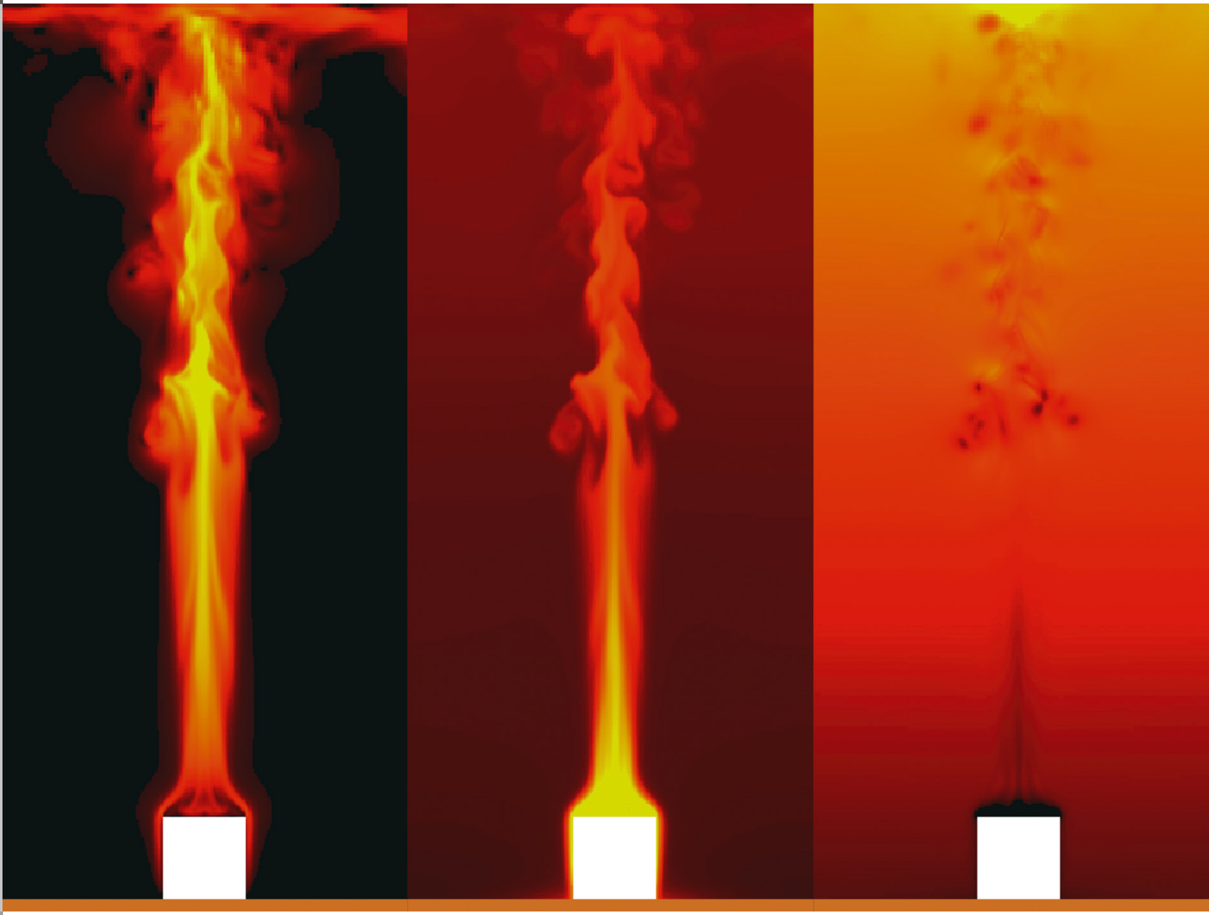

IAS Series
Band / Volume 31
ISBN 978-3-95806-173-6

JÜLICH
FORSCHUNGSZENTRUM

Schriften des Forschungszentrums Jülich
IAS Series Band / Volume 31

Die Dissertation kann wie folgt zitiert werden:

urn:nbn:de:hbz:468-20161005-143323-8
[http://nbn-resolving.de/urn/resolver.pl?urn=urn%3Anbn%3Ade%3Ahbz%3A468-20161005-143323-8]

Forschungszentrum Jülich GmbH
Institute for Advanced Simulation (IAS)
Jülich Supercomputing Centre (JSC)

A study on buoyancy-driven flows: Using particle image velocimetry for validating the Fire Dynamics Simulator

Andreas Meunders

Schriften des Forschungszentrums Jülich
IAS Series Band / Volume 31

ISSN 1866-1807 ISBN 978-3-95806-173-6

Bibliographic information published by the Deutsche Nationalbibliothek.
The Deutsche Nationalbibliothek lists this publication in the Deutsche Nationalbibliografie; detailed bibliographic data are available in the Internet at http://dnb.d-nb.de.

Publisher and Distributor: Forschungszentrum Jülich GmbH
Zentralbibliothek
52425 Jülich
Tel: +49 2461 61-5368
Fax: +49 2461 61-6103
Email: zb-publikation@fz-juelich.de
www.fz-juelich.de/zb

Cover Design: Grafische Medien, Forschungszentrum Jülich GmbH

Printer: Grafische Medien, Forschungszentrum Jülich GmbH

Copyright: Forschungszentrum Jülich 2016

Schriften des Forschungszentrums Jülich
IAS Series Volume 31

D 468 (Diss., Wuppertal, Univ., 2016)

ISSN 1866-1807
ISBN 978-3-95806-173-6

Persistent Identifier: urn:nbn:de:0001-2016091517

The complete volume is freely available on the Internet on the Jülicher Open Access Server (JuSER) at www.fz-juelich.de/zb/openaccess.

This is an Open Access publication distributed under the terms of the Creative Commons Attribution License 4.0, which permits unrestricted use, distribution, and reproduction in any medium, provided the original work is properly cited.

Abstract

The aim of this thesis is to design and carry out bench-scale laboratory experiments specifically designed for the validation of fire models, and to use the experimental data for a validation study of the Fire Dynamics Simulator (FDS). The focus of the experiments is on one of the key components of fire models, the modeling of buoyancy-driven flows. The experimental setup is simplified by neglecting pyrolysis and combustion and its objective is to achieve high precision and reproducibility. Therefore, an electrically heated block of copper is used as a heat source and particle image velocimetry (PIV) is applied for measuring the flow velocities. Two different setups are investigated: an undisturbed open buoyant plume above the heat source, and a buoyant spill plume emerging from a compartment opening.

Depending on the setup, different characteristic values of the flow are evaluated. For the undisturbed buoyant plume setup, maximum velocities in the plume, plume widths and flow integrals are determined. Furthermore, a centerline analysis is carried out in order to localize the transition from laminar to turbulent flow as a function of the Grashof number. The obtained values lie in the range $4 \times 10^8 < Gr < 2 \times 10^9$ and therefore agree well with previous studies. For the buoyant spill plume compartment setup, position and maximum velocity of the outflow as well as volume flows in front of the opening are compared. The heat flows out of the opening cannot be measured directly and are therefore estimated based on the available data.

The validation study with FDS leads to mixed results. For the open plume setup, generally a good agreement is achieved. Provided that a sufficiently fine resolution is used, the important flow characteristics are reproduced in the simulations. With the spill plume setup, significant differences between experiments and simulations are observed. In order to analyze them in detail, modifications of the experiments are required. Therefore, in conclusion of the study, areas of potential improvements for future experiments and the suitability of PIV for this kind of experiment are discussed.

Zusammenfassung

Das Ziel der Arbeit besteht in der Planung und Durchführung von Experimenten im Labormaßstab zur Validierung von Brandsimulationsprogrammen. Die erhobenen Daten werden anschließend für die Validierung des Fire Dynamics Simulator (FDS) genutzt. Der Fokus der Experimente liegt auf auftriebsgetriebenen Strömungen, einem zentralen Element für Brandsimulationen. Durch den Ausschluss von Pyrolyse und Verbrennung werden die Experimente vereinfacht und eine höhere Genauigkeit und Wiederholbarkeit erreicht. Zu diesem Zweck wird ein elektrisch beheizter Kupferblock als Wärmequelle eingesetzt und die Strömungsgeschwindigkeiten mittels particle image velocimetry (PIV) gemessen. Zwei unterschiedliche Aufbauten werden untersucht, einerseits der freie Auftriebsstrahl über der Wärmequelle, andererseits die auftriebsgetriebene Ausströmung aus einer Raumöffnung.

In Abhängigkeit des experimentellen Aufbaus werden unterschiedliche Charakteristika der Strömung ausgewertet. Im freien Auftriebsstrahl werden maximale Strömungsgeschwindigkeiten, Plumebreiten und Strömungsintegrale ermittelt. Außerdem werden die Zentrallinien analysiert, um den Umschlag von laminarer zu turbulenter Strömung in Abhängigkeit der Grashof Zahl zu bestimmen. Die Ergebnisse liegen im Bereich von $4 \times 10^8 < Gr < 2 \times 10^9$ und damit in guter Übereinstimmung mit früheren Studien. Im zweiten Aufbau werden die Position und maximale Geschwindigkeiten der Ausströmung sowie die Volumenströme vor der Raumöffnung verglichen. Da die konvektiven Wärmeströme aus der Öffnung nicht direkt gemessen werden können, werden sie auf Grundlage der vorhandenen Daten abgeschätzt.

Der Vergleich mit FDS Simulationen zeigt nur teilweise gute Übereinstimmung. Während Simulationen mit ausreichend feiner Auflösung die wesentlichen Charakteristika des freien Auftriebsstrahls gut wiedergeben, zeigen sich im zweiten Aufbau deutliche Unterschiede. Um diese eingehender zu untersuchen, sind Veränderungen an den Experimenten erforderlich. Zum Abschluss der Arbeit werden daher mögliche Verbesserungen diskutiert sowie ein Fazit zur Eignung von PIV für Experimente dieser Art gezogen.

Acknowledgements

This thesis summarizes my work from 2011 to 2016 at the Bergische Universität Wuppertal, the Forschungszentrum Jülich and the University of Canterbury, NZ, where I worked as a visiting researcher.

I am thankful to my supervisors, Armin Seyfried and Lukas Arnold, who encouraged me to take up research in Fire Safety Engineering and supported me in many ways throughout the work on this thesis. Their attitude towards science is inspiring. Together with the entire working group at Bergische Universität Wuppertal and Forschungszentrum Jülich they made my time at both institutions very special.

I would also like to thank Bjarne Husted from Lund University for writing the second report on this thesis and Andreas Schlenkhoff and Roland Goertz from Bergische Universität Wuppertal for being part of the examination committee.

The experimental work within this thesis would not have been possible without the support of my colleagues at IEK-6, in particular Alexander Belt and Alexander Hundhausen. Despite the numerous technical problems that were to overcome, the lab-time was great. The same goes for Leonie Rommeswinkel and Anna Tscherniewski, who became DaVis experts while processing the experimental data. I would also like to thank my colleagues from ZEA-1 Knut Dahlhoff, Harald Glückler, Thomas Louis, Thomas Töpfer, and Steffen Wolf for providing expertise, equipment and practical help in support of the experiments.

I'm grateful to Michael Spearpoint, Charles Fleischmann, Dennis Pau, Greg Baker, and Xiaoyun Wang for giving me a warm welcome at the University of Canterbury and for willingly sharing their experimental expertise with me. I gratefully acknowledge the scholarship for doctoral candidates granted by the German Academic Exchange Service (DAAD) for my stay in New Zealand, and the computing time granted on the supercomputers JUROPA and JURECA at Jülich Supercomputing Centre (JSC).

Last, but not least, I would like to thank my family and friends for their support and understanding.

Contents

List of Figures **xi**

List of Tables **xv**

Nomenclature **xvii**

1 Introduction **1**
- 1.1 Motivation 2
- 1.2 Outline of this thesis 3

2 State of the art and preparatory work **5**
- 2.1 Fire simulation 5
  - 2.1.1 Applications and approaches 5
  - 2.1.2 Fundamentals of FDS 8
  - 2.1.3 Validation experiments 12
  - 2.1.4 Introduction of FDSgeogen 14
- 2.2 Particle image velocimetry 17
  - 2.2.1 Particles 19
  - 2.2.2 Illumination 20
  - 2.2.3 Recording unit 21
  - 2.2.4 Processing and evaluation 22
  - 2.2.5 Measurement accuracy 25

3 An undisturbed buoyant plume above a heat source **29**
- 3.1 Experiments 30
  - 3.1.1 Experimental setup 30
  - 3.1.2 Experimental procedure 39
  - 3.1.3 Image processing 42
  - 3.1.4 Evaluation of experiments 46
- 3.2 Simulations with FDS 64
  - 3.2.1 Simulation setup 65

3.2.2 Execution and output processing 73
3.2.3 General observations 74
3.3 Comparison of experiments and simulations 77
3.3.1 Boundary conditions 77
3.3.2 Flow pattern 80
3.3.3 Plume centerlines 85

4 A spill plume emerging from a compartment opening 89
4.1 Experiments 90
4.1.1 Experimental setup and procedure 90
4.1.2 Image processing 94
4.1.3 Experimental results 95
4.2 Simulations with FDS 109
4.2.1 Simulation setup 109
4.2.2 Execution and evaluation 113
4.3 Comparison of experiments and simulations 116
4.3.1 Temperature stratification 116
4.3.2 Centerlines 116
4.3.3 Volume flow in front of the opening 119
4.3.4 Heat flow out of the compartment 121

5 Conclusions 129

Bibliography 133

A Complete overview over open plume experiments 145

B Complete overview over spill plume experiments 147

List of Figures

2.1 FDSgeogen workflow in principle. 16
2.2 Reading in parameter files in FDSgeogen. 17
2.3 Schematic representation of a 2D PIV system. 18
2.4 Schematic representation of a Nd:YAG double pulsed laser. . . 20
2.5 Staggered pulse trains from double pulsed lasers for PIV. . . . 21
2.6 Light sheet optics using three cylindrical lenses. 22
2.7 Cross correlation for determination of velocity vectors. 23
2.8 Composition of peaks in the cross-correlation function. 24
2.9 Vector computation via iterative multigrid approach. 25

3.1 Laser safety box and computers used for the PIV measurements. 31
3.2 Sketch of the open plume experiment. 32
3.3 Technical drawing of the heat source. 34
3.4 Heat source temperature depending on the surface quality. . . 35
3.5 Picture of the applied Dual-Nd:YAG laser. 36
3.6 Picture of the open plume experiments. 37
3.7 Particle size distribution of the used aerosol generator. 38
3.8 Target for camera calibration. 40
3.9 Background subtraction for enhanced image quality. 43
3.10 Close-up of a single interrogation window. 44
3.11 Flow velocity field and velocity profiles of run 1.1. 45
3.12 Thermal images of the heat source. 47
3.13 Deviation between inner heat source temperature and surface temperature. 48
3.14 Scattering of heat source temperatures during the experiments. 49
3.15 Scattering of the ambient temperatures during the experiments. 50
3.16 Temperature stratification inside the enclosure for different power settings. 51
3.17 Schematic representation of the involved heat transfer mechanisms. 52
3.18 Comparison of instantaneous velocity fields. 55

3.19 Comparison of time-averaged velocity fields. 56
3.20 Relative measurement uncertainty of typical velocity fields. . . 56
3.21 Scattering of v_z velocity profiles of all experiments. 58
3.22 Characteristic flow values in different heights. 59
3.23 Centerline positions for all experimental runs. 61
3.24 Vertical velocities in the centerline of the plumes. 63
3.25 Standard deviation of v_x in the centerline of the plumes. . . . 64
3.26 Mesh distribution for open plume simulations. 68
3.27 Grid sensitivity study for open plume simulations. 69
3.28 Prescribed initial temperatures for open plume simulations. . . 71
3.29 Chronological sequence of temperature profiles inside the enclosure wall. 72
3.30 Heat balances of incoming and outgoing heat fluxes. 73
3.31 Flow velocities and gas temperatures close to the heat source. 75
3.32 Time-averaged temperature fields for open plume simulations with 96 W. 76
3.33 Convective, radiative and conductive fractions of the total heat input. 76
3.34 Comparison of surface temperatures on top of the heat source. 78
3.35 Comparison of temperature stratification inside the enclosure. 79
3.36 Temperature stratification in simulations with different grid resolutions at $P_{HS} = 96\,\mathrm{W}$. 80
3.37 Time-averaged velocity fields at $P_{HS} = 96\,\mathrm{W}$ in experiment and simulation. 81
3.38 Comparison of v_z velocity profiles. 82
3.39 Comparison of characteristic flow values. 84
3.40 Vertical velocities in the centerline of the plume. 85
3.41 Standard deviation of v_x in the centerline of the plumes. . . . 86

4.1 Sketch of the spill plume experiment. 91
4.2 Pictures of the spill plume experiment. 92
4.3 Laser light sheet in front of the compartment opening. 93
4.4 Background subtraction from raw particle images. 95
4.5 Scattering of heat source temperatures. 96
4.6 Scattering of ambient temperatures. 97
4.7 Temperature stratification inside the enclosure. 98
4.8 Temperature stratification inside the compartment. 98
4.9 Instantaneous velocity fields at $dw = 80\,\mathrm{mm}$. 100
4.10 Instantaneous velocity fields at $dw = 40\,\mathrm{mm}$. 100
4.11 Comparison of velocity fields at $dw = 80\,\mathrm{mm}$. 101
4.12 Comparison of velocity fields at $dw = 40\,\mathrm{mm}$. 101

4.13 Relative measurement uncertainties at $dw = 80\,\mathrm{mm}$. 102
4.14 Relative measurement uncertainties at $dw = 40\,\mathrm{mm}$. 102
4.15 Centerlines for both door widths. 104
4.16 Flow velocities along the centerlines. 105
4.17 Volume flows at $x = 10\,\mathrm{mm}$ at the highest heat input. 106
4.18 Velocity fields at $x = 10\,\mathrm{mm}$ for $dw = 80\,\mathrm{mm}$. 108
4.19 Velocity fields at $x = 10\,\mathrm{mm}$ for $dw = 40\,\mathrm{mm}$. 108
4.20 Overview of volume flows in front of the opening for all experiments. 109
4.21 Mesh distribution for spill plume simulations. 111
4.22 Grid sensitivity study for spill plume simulations. 112
4.23 Velocity fields at $dw = 80\,\mathrm{mm}$. 115
4.24 Velocity fields at $dw = 40\,\mathrm{mm}$. 115
4.25 Temperature stratification in experiment and simulation. . . . 117
4.26 Comparison of centerlines for different heat inputs. 118
4.27 Analysis of centerlines at $P_{HS} = 97\,\mathrm{W}$ and $dw = 80\,\mathrm{mm}$. . . . 120
4.28 Overview of volume flows in front of the opening in experiment and simulation. 121
4.29 Outflow in front of the compartment as function of x. 122
4.30 Ratio of estimated to true volume flows as derived from the simulations. 123

List of Tables

3.1 Abridged overview over open plume experiments. 42
3.2 Estimates of the radiative and convective fractions. 54
3.3 D^* and $D^*/\delta x$ for various grid resolutions and heat inputs. . . 70
3.4 Compute times for open plume simulations. 74

4.1 Abridged overview over spill plume experiments. 94
4.2 Compute times for spill plume simulations. 113
4.3 Calculation of heat flows for $dw = 80\,\text{mm}$. 126
4.4 Calculation of heat flows for $dw = 40\,\text{mm}$. 126

A.1 Overview over open plume experiments. 146

B.1 Overview over spill plume experiments with $dw = 80\,\text{mm}$. . . . 148
B.2 Overview over spill plume experiments with $dw = 40\,\text{mm}$. . . . 149

Nomenclature

General

δx	Cell size
$\dot{m}$	Mass flow
$\dot{Q}$	Heat flow
$\dot{V}$	Volume flow
$\overline{x}$	Arithmetic mean / normalized value
A	Area
c_p	Specific heat capacity at constant pressure
d	Diameter
D^*	Characteristic fire diameter
dw	Door width
f	Frequency, frame rate
Fr	Froude number
g	Gravitational acceleration
Gr	Grashof number
h	Height
k	Thermal conductivity
l	Length

m	Mass
Ma	Mach number
N	Number of measurements
P	Electric power
p	Pressure
R_s	Specific gas constant
Re	Reynolds number
T	Temperature
t	Time
V	Volume
v	Velocity
w	Width
x, y, z	Coordinates

Greek letters

β	Coefficient of thermal expansion
ϵ	Emissivity
λ	Wavelength
μ	Dynamic viscosity, as a prefix: micro
ν	Kinematic viscosity
ρ	Density
σ	Standard deviation or Stefan-Boltzmann constant

Subscripts and superscripts

$+$	Measured in positive x, y or z direction

0	Initial value
$1-11$	Location of temperature devices
∞	At infinity
b	At the bottom
cl	Referring to the centerline
$cond$	Conductive fraction
$conv$	Convective fraction
$encl$	Referring to the enclosure
end	Final value or simulation time
est	Estimated value
f	Referring to the fluid
HS	Referring to the heat source
in	Inflow into the compartment
m	Measurement
max	Maximum
out	Outflow out of the compartment
P	Referring to a power setting
p	Referring to the particle(s)
Pro	Referring to the insulating base (Promat)
rad	Radiative fraction
s	Referring to the solid
sim	Referring to the simulation
$surf$	Referring to the surface
tot	Total value
$true$	True value

x, y, z	In x, y or z-direction

Acronyms

CCD	Charge coupled device
CF	Correction factor
CFAST	Consolidated Model of Fire and Smoke Transport
CFD	Computational fluid dynamics
CFL	Courant, Friedrichs, Lewy
CID	Charge injection device
CMOS	Complementary metal-oxide semiconductor
CPU	Central processing unit
CSV	Comma-separated values
DAAD	Deutscher Akademischer Austauschdienst, German Academic Exchange Service
DEHS	Di(2-ethylhexyl)sebacate
DNS	Direct numerical simulation
FDM	Finite difference method
FDS	Fire Dynamics Simulator
FEM	Finite element method
FVM	Finite volume method
FZJ	Forschungszentrum Jülich GmbH
HVAC	Heating, ventilating and air conditioning
IEK	Institut für Energie- und Klimaforschung
JSC	Jülich Supercomputing Center
JURECA	Jülich Research on Exascale Cluster Architectures, JSC's general purpose supercomputer since 2015

JUROPA	Jülich Research on Petaflop Architectures, JSC's general purpose supercomputer 2009 - 2015
LES	Large eddy simulation
LIF	Laser-induced fluorescence
MBO	Musterbauordnung, the German model building code
MPI	Message passing interface
Nd:YAG	Neodymium-doped yttrium aluminium garnet
NIST	National Institute of Standards and Technology
OpenMP	Open Multi-Processing
PDA	Phase Doppler anemometryy
PIV	Particle image velocimetry
PMMA	Polymethyl methacrylate
Pt100	Platinum resistance thermometer with 100 Ω at 0 °C
RANS	Reynolds-averaged Navier-Stokes
SFPE	Society of Fire Protection Engineers
SLR	Single-lens reflex
SMV	Smokeview
SNR	Signal-to-noise ratio
TPIV	Thermal particle image velocimetry
XML	Extensible Markup Language
ZEA	Zentralinstitut für Engineering, Elektronik und Analytik

Chapter 1

Introduction

Over the last few decades, computer fire models have undergone a remarkable evolution. While they were still barely used in the early 1990s, today they have become an everyday tool for many engineers and scientists in fire safety engineering. From the author's point of view, several factors have driven this development.

With the advent of performance-based codes in fire safety engineering, an important area of application for fire models has developed. A performance-based approach allows for a more flexible building design compared to a prescriptive approach. Instead of prescribing specific safety measures, safety objectives are defined. It is the obligation of the planner to prove that these safety objectives are achieved and that the building therefore complies with the building code. Computer fire models often play an essential role in producing this evidence. During the last 25 years, the performance-based approach has found increasing application worldwide [1–8]. And although open questions remain (for example with regard to tenability criteria, scenario selection or the incorporation of risk) and sometimes a reintroduction of prescriptive elements is required [9], performance-based design has become an integral part of fire safety engineering.

A performance-based approach requires more sophisticated tools, such as computational fire models, to determine the effects of a fire. But it also requires a deeper understanding of fire in the broadest sense (including not only the actual fire physics, but also the organizational, legislative and societal framework of fire safety, physiological and psychological response of humans to fire and smoke, etc.) and therefore a higher qualification of the engineers involved. This leads to another major driver for the development of computational fire models. During the last few decades, fire safety engineering has developed as an independent profession among other engineering disciplines [10]. As a result, understanding of the numerous complex phenomena, which are involved in even the smallest fire, has improved.

At the same time, the available computer performance has increased immensely. Due to increased processor speeds and the introduction of multi-core processors, it was possible to double the computer performance every 18 to 24 months [11]. This relation is known as Moore's law [12] and allows computations today which would have been unthinkable only a few years ago. Advancements in computer science have made the evolution of computer fire models possible in the first place [10]. However, sophisticated fire models still incorporate many simplifying assumptions, either in order to be computable in a reasonable amount of time or due to a lack of knowledge of the underlying processes. Therefore, much research still needs to be done; this work is meant to be a contribution to it.

1.1 Motivation

The extreme difficulty of modeling fire as a physical phenomenon on a real scale has been summarized by Hostikka [13]: "The complexity of fire modelling results from the multitude of physical problems and chemical reactions to be solved simultaneously and the wide range of associated time and length scales." Computer fire modeling builds upon several different scientific disciplines and it has many overlaps with areas of active research. Therefore, it goes without saying that an integral part of the development and application process of a fire model is to evaluate its reliability and quantify its predictive capability. This process is generally referred to as validation; a more detailed definition is given in Section 2.1.3.

The responsibility for the validation of a model lies not only with its developers. Eventually, it is the user of a model who has the best knowledge of the application and needs to make sure that it complies with the limits of applicability. In case of the Fire Dynamics Simulator (FDS), which is the fire model used in this thesis, the developers deny a sweeping statement of the validity of the model by declaring it "may or may not have predictive capability" and "all results should be evaluated by an informed user" [14]. Nevertheless, an extensive validation suite is provided and professionally maintained by the developers in order to support the user in making an informed decision [15].

For fire models in general, a great variety of validation studies have already been performed. Many of them have led to new insights by revealing flaws in the models, marking the limits of applicability or underpinning the confidence in the models. However, many open questions remain, for example with regard to "overall uncertainties and error estimates of fire models" [10, 16]. From the author's point of view, these questions can be best addressed by simplified laboratory experiments with reduced complexity. Although real-scale fire tests, which include the burning of real furniture or wood cribs in a real building, for example, are closer to the later application, they are often too complex for validation. Simplified laboratory experiments are less realistic, but allow the researcher to concentrate only on specific physical phenomena. Also, the reproducibility is increased and measurement techniques with higher precision can be applied. Both are vital factors for the uncertainty quantification. With the increasing quality of numerical calculations, the quality of the experimental data for validation also needs to increase. As Raffel states, "the experimental data of the flow field must possess high resolution in time and space in order to be able to compare them with high density numerical data fields" [17]. One measurement technique that can provide very accurate velocity measurements with a high spatial and temporal resolution is particle image velocimetry (PIV). Therefore, this technique has been applied in this thesis.

1.2 Outline of this thesis

This thesis aims at designing and carrying out bench-scale laboratory experiments that are well suited for the validation of fire models. The focus lies on buoyancy-driven flows because they are the main driver for the spread of smoke in a fire. The experiments are simplified by neglecting combustion and pyrolysis and they aim to achieve a high reproducibility. Due to its high precision and resolution, particle image velocimetry is used to measure the flow velocities. After the experiments are carried out, simulations with FDS are set up and the results are compared to the experimental data. Besides the collection of validation data, this study also aims to gain experience with the application of PIV for the validation of fire models. Therefore, practical problems encountered throughout the experiments are discussed, and areas of potential improvement for future experiments are identified.

In Chapter 2, the current state of the art with regard to fire simulation and particle image velocimetry is discussed. This includes an overview of possible applications of fire models, their role within a performance-based design process, and a categorization by different model classes. The fundamentals of FDS relevant to the simulations in this work are explained, and an overview of validation studies that have applied PIV for the velocity measurements is provided. Finally, the basic components of a PIV system are explained as a basis for understanding the experiments described later.

In this work two different scenarios are investigated: an undisturbed buoyant plume above a heat source and a buoyant spill plume emerging from a compartment opening. The undisturbed buoyant plume, also referred to as open plume, is analyzed in Chapter 3. First, the experimental setup and procedure as well as the evaluation of the experiments are described. Subsequently, the implementation of the experimental setup into FDS simulations is explained. Finally, the results of the experiments and simulations are compared with each other.

Chapter 4 covers the scenario of a buoyant spill plume emerging from a compartment opening. This experimental setup builds upon the open plume setup but increases the complexity by positioning the heat source inside a compartment. This chapter is structured similarly to the previous chapter. However, since a different scenario is analyzed, different evaluation methods are required and different flow characteristics are compared between experiments and simulations.

In Chapter 5 conclusions from the investigations in this thesis are drawn and suggestions for future research are provided.

Chapter 2

State of the art and preparatory work

This chapter provides an overview of the current state of the art of fire simulation. The focus lies on the Fire Dynamics Simulator (FDS), which will be used for the simulations conducted in this thesis. In addition, FDSgeogen, a tool that simplifies the automated setup of a multitude of FDS simulations, is introduced. In order to provide a basis for the experiments described later, the fundamentals of particle image velocimetry (PIV) are explained.

2.1 Fire simulation

Within this section the areas of application for fire simulation are explained, and different approaches and validation experiments are introduced.

2.1.1 Applications and approaches

At least three areas can be distinguished in which fire simulations are frequently applied. The first area is in the course of the design and building permit process, when a new building is planned or an existing building is converted for a new use. The second area of application is for scientific use, whether for basic research or in connection with the development of new products. The final area to be discussed here is in post-fire investigations for forensic analyses, which try to reveal the course of events in retrospect. The first area, which is the primary area of application, will be explained in more detail based on German legislation.

In Germany, four universal protection goals are defined in the "Musterbauordnung" (MBO) [18], which functions as the model building code for the building regulations in Germany's different states.

1. Prevent the emergence of a fire.
2. Prevent the propagation of fire and smoke.
3. Enable escape and rescue measures.
4. Enable effective fire-fighting.

Buildings need to comply with these protection goals during their entire lifespan, including construction, occupancy and maintenance. The compliance with these protection goals can be proved in different ways; for this, one usually distinguishes between prescriptive and performance-based design. Further information on these two methods can be found in the literature [8, 19, 20], but a summary is given below.

In the prescriptive approach, the requirements of the regulations are met, and only certified or tested construction measures are used, possibly accompanied by technical fire protection measures. On the other hand, the performance-based approach can be applied when the regulative requirements cannot be entirely fulfilled. This approach aims at proving the same level of safety as the prescriptive approach. Therefore, a number of steps are required, e.g. assess the circumstances relevant to fire safety, specify the building use and number of occupants, underpin the qualitative protection goals with quantitative performance criteria, and determine fire scenarios and design fires. When these preparatory steps are carried out, performance-based design methods such as fire simulations can be used. Subsequently, the simulation results are compared with the previously-defined performance criteria. Only via these quantitative values can the simulation results be used to assess the fulfillment of the qualitative protection goals. For example, performance criteria for the safe egress of occupants could be a threshold for optical density and temperatures at a certain height, which must not be exceeded during the evacuation period.

Depending on the question that needs to be addressed, a variety of calculation and simulation methods are available for performance-based fire safety design. According to [8], four modeling classes can be distinguished.

1. Empirical models
2. Post-flashover models
3. Zone models

4. Computational fluid dynamics (CFD) or field models

Empirical models are derived from experimental studies and condense the results of those studies into simple relations. The equations usually do not incorporate a time dependency and can often be solved by hand. Their validity is limited to the range of the experimental study on which they are based. Plume formulas, for example, allow plume temperatures and velocity or flame height to be calculated based on the heat release rate or the diameter of a fire. Frequently used plume formulas have been developed by Zukoski, Heskestad and McCaffrey [21–24], among others.

Post-flashover models, as the name suggests, can only be applied for a fully developed post-flashover fire, in which a uniform temperature distribution inside the compartment can be assumed. Although they are based on theoretical considerations, they can also include empirical relations, e.g. for the heat release rate of the fire. The resulting compartment temperature inside the room is derived based on the conservation of energy. This means that, from the heat released by the fire, all other heat fluxes out of the compartment are subtracted in order to obtain the amount of energy that heats the compartment itself.

Zone models extend the functionality of post-flashover models by introducing at least two distinct layers: a hot upper layer that is smoke-filled, and a cold lower layer that is smoke-free. Both layers are assumed to be internally uniform. There is no mass transfer between the two layers apart from the fire plume, which feeds hot gases into the upper layer. The amount of mass moving between the layers can be calculated based on empirical correlations (plume formulas) as described above. Some zone models are able to handle multi-zone and multi-room geometries; however, complex geometrical details cannot be considered. Also, it is conceptually impossible to obtain local variables, for example, gas temperatures for the design of load-bearing structures or soot densities for the activation of smoke detectors. Exemplary zone models are CFAST and B-RISK [25, 26].

The fourth class of models are computational fluid dynamics (CFD) models, also referred to as field models. Of the models described they are the most sophisticated and offer the widest scope of application. CFD models are not only applied in fire safety engineering, in fact, this is one of the minor areas of application. Major fields of application are for example the aerospace and automotive industry, turbine design or meteorology. They are based on fundamental physical principles of the conservation of mass, energy and momentum. It is from these principles that the conservation equations are derived, which are used to determine the evolution of state variables such as pressure or temperature. To allow for a numerical solution of the partial differential equations (usually the Navier Stokes equations), the entire computational domain is divided into cells. The total number of cells can easily exceed several millions, and each cell is assumed to be internally uniform. There are mainly three different methods available for the numerical solution; the finite volume method (FVM), the finite element method (FEM), or the finite difference method (FDM). More information on these methods can be found in the extensive literature [27–29].

Because CFD models are based on fundamental physical principles, they can be applied to a large variety of different scenarios, without the need to derive empirical relations from experimental studies beforehand. Nevertheless, validation experiments are necessary to ensure that the simulation results are sufficiently accurate. Due to the high spatial resolution, complex geometries can be simulated, and detailed information about local variables such as temperature, pressure or species concentration is available. The disadvantages are the high demands in terms of model development, simulation setup, computing effort, and interpretation of results. Exemplary CFD models for fire simulation are FDS, OpenFOAM/FireFOAM, and ANSYS Fluent [14, 30]. Because FDS is applied for the simulations in this thesis, it is explained in more detail in the following section.

2.1.2 Fundamentals of FDS

The Fire Dynamics Simulator (FDS) and its companion visualization tool smokeview (SMV) are "the products of an international collaborative effort led by the National Institute of Standards and Technology (NIST) and the VTT Technical Research Centre of Finland" [14,31]. To date, it is one of the most widespread CFD models used in fire safety engineering worldwide and it is accepted by many authorities having jurisdiction. A number of reasons have contributed to its acceptance.

- It is specifically designed for modeling the impact of fires and therefore includes sub-models that are required for fire engineering. For example, it is possible to model pyrolysis, combustion, soot production and deposition, species transport, smoke toxicity, sprinkler and heating, ventilating and air conditioning (HVAC) systems. Although some of these sub-models are still subject to ongoing research and it is always the responsibility of the user to make sure the limits of FDS applicability are complied with, the availability of these features proves useful for various applications.
- Despite its numerous features, FDS is comparably fast, which is enabled by a rectangular mesh without sophisticated refinement strategies.

- The extensive and regularly updated documentation facilitates the correct application of FDS. In addition, various user communities work on the improvement and acceptance of FDS [32–34].
- Numerous validation studies have been carried out with FDS, which means that for many applications an approximate simulation error is known [15].

The following introduction to the fundamental principles of FDS 6 [14] is given with regard to the simulations conducted later in this study. Therefore, several irrelevant sub-models are neglected, for example, those modeling pyrolysis or combustion. More detailed information on the use of FDS, the mathematical models, or validation and verification are provided in the respective documentation, which is also the basis for the following sections [14,15,35–37]. For background information, see the extensive literature on CFD in general [27–29] or with a special focus on fire simulation [38]. Theoretical introductions to the fire dynamics that are to be modeled are, for example, provided in the SFPE Handbook of Fire Protection Engineering or by Drysdale, Quintiere and Karlsson [39–42].

As the user's guide states, "FDS solves numerically a form of the Navier-Stokes equations appropriate for low-speed ($Ma < 0.3$), thermally-driven flow with an emphasis on smoke and heat transport from fires" [14]. The hydrodynamic model employs finite differences scheme accurate to the second order. Therefore, the computational domain is discretized by a uniform, rectangular mesh. In every mesh cell, macroscopic properties such as flow velocity, density, enthalpy, and soot or species concentration are calculated and stored. Local mesh refinements within a mesh are not possible, and obstructions in the simulations are made to conform to the underlying mesh. Hence, curved objects cannot be accurately represented and need to be approximated by the rectangular mesh. The computational domain can be split into several meshes in order to better represent a geometry or to divide the computational load among several computing units.

For the time integration, an explicit second order predictor-corrector scheme is used; the time step is adjusted so that the Courant, Friedrichs, Lewy (CFL) condition is fulfilled. This condition provides an upper limit for the time step in explicit time-integration schemes and does not allow an observed value to propagate more than one cell during a time step. An appropriate initial time step is estimated based on the dimensions of the smallest mesh cell, the height of the computational domain, and the acceleration of gravity.

Since a second-order accurate finite differences scheme is applied, halving the cell size reduces the discretization error by a factor of four. On the other hand, the computational effort will be increased by a factor of approximately 16, because in every dimension the number of cells doubles and, due to the CFL condition, the time step can only be half as long. Therefore, it is common practice to carry out a grid sensitivity study, which aims at finding a resolution that is sufficiently fine for grid-independent results but not finer than necessary to save computation time. This is usually done by starting a simulation on a coarse mesh and gradually refining the grid until the observed values converge. In addition, there are characteristic values that can hint at an appropriate mesh resolution. For simulations involving buoyant plumes, the dimensionless expression $D^*/\delta x$ can be used as a measure of how well the flow is resolved [14]. δx is the nominal size of a mesh cell and D^* is the characteristic fire diameter, which calculates as:

$$D^* = \left(\frac{\dot{Q}}{\rho_\infty \cdot c_p \cdot T_\infty \cdot \sqrt{g}} \right)^{\frac{2}{5}} \tag{2.1}$$

The expression $D^*/\delta x$ therefore states the number of cells by which the characteristic diameter of the fire is resolved. Because this value takes the actual scenario into account, it is a better reference for an appropriate grid resolution than an absolute number. However, one should keep in mind that, depending on the scenario, other geometrical details such as narrow openings can become decisive.

Turbulence is treated in FDS by using a large eddy simulation (LES) as a default. Direct numerical simulation (DNS) is also possible but in general is not practical. The main idea in LES is to calculate those eddies that are resolved by the mesh and to model the small-scale eddies with artificial eddy viscosity. In FDS, the Deardorff eddy viscosity model is used for modeling the effects of turbulence on sub-grid scale [43]. The LES filter width is taken as the geometric mean of the local cell size in each direction. For cubic cells, the filter width is equal to the edge length of a cell, which is referred to as implicit filtering. When LES is applied, it is important to use sufficiently high mesh resolution to capture the important eddies in a flow, which are, for example, responsible for the entrainment of air into a plume.

The radiation transport in FDS is calculated by a technique similar to finite volume methods used for convective transport. As a default, 100 discrete angles are used to calculate the radiation exchange among obstructions and gas; more angles can be used for higher precision. The radiation solver is called upon every third time step to update one fifth of the radiation angles. Thus, the radiation transport equation is completely updated every 15 time steps. As a rule of thumb, this takes up about 20 % of the overall computation time for a simulation. It is assumed that the gas in the simulation behaves as a gray gas, which means that its emissivity is not particularly sensitive to wavelength. This assumption is justified by the presence of soot in most fire simulations.

In FDS, only one dimensional heat conduction in the direction normal to the surface can be calculated. To compute the temperature inside the solid, FDS solves the one-dimensional heat transfer equation numerically.

$$\rho_s c_s \frac{\delta T_s}{\delta t} = \frac{\delta}{\delta x}\left(k_s \frac{\delta T_s}{\delta x}\right) + \dot{q}_s''' \tag{2.2}$$

The temperature evolution inside the solid therefore depends on its average density ρ_s, specific heat c_s, and thermal conductivity k_s. The source term $\dot{q}_s'''$ additionally considers the heat input or loss inside the solid via chemical reactions and radiative emission or absorption. Because the material temperatures usually do not fluctuate strongly, the heat transfer equation is only updated every second time step, in order to save computation time. For the spatial discretization a different grid than in the gas phase is used. The mesh resolution on the surface of the solid is automatically chosen depending on the thermal diffusivity of the respective material. By default, the mesh resolution decreases from the layer boundaries towards the middle of the solid. The boundary condition at the front surface takes both convective and radiative heat fluxes into account. If DNS is applied, the convective heat transfer is calculated directly; for LES, it is based on a combination of natural and forced convection correlations [14].

As CFD simulations are very computationally intensive and modern computers draw their power from a large number of processors, code parallelization is an important issue [11]. In FDS, a hybrid parallelization using OpenMP and MPI is applied. Message passing interface (MPI) is a distributed memory approach, meaning the work is decomposed and spread to multiple processes. Data or results from other processes are exchanged by explicit messages, for example via a network between computation nodes. In Open Multi-Processing (OpenMP), however, all processes have access to the same memory; it is therefore referred to as shared memory approach. Although the OpenMP scalability in FDS is not ideal, a speedup to a factor of two can be achieved without additional configuration work by the user [44].

For the MPI parallelization, the user needs to split the computational domain into as many meshes as there are MPI processes, so that each mesh can be assigned to one process. For stability reasons it is recommended to compute all meshes with a synchronized time step; therefore, it is also advisable to make the meshes similar in size, in order to obtain a balanced computational load and prevent individual cores from idling. The simulations in this thesis are carried out on up to 96 cores on the general purpose supercomputer JURECA using both OpenMP and MPI. For more information on the parallelization and scalability of FDS, see [44, 45].

2.1.3 Validation experiments

When a fire simulation tool is developed, its correctness and reliability must be evaluated continuously. This process is referred to as verification and validation. In a position paper on verification and validation of numerical fire models published by the international FORUM of fire research directors, these two elements of the evaluation process are distinguished as follows [4]. Verification is defined as "solving the equations right", which means it deals only with computational science and mathematics. It does not imply that the governing equations are appropriate; only that they are being solved correctly. On the other hand, validation means "solving the right equations". It deals with the physical phenomena and evaluates the appropriateness of the mathematical models. Its objective is to quantify the predictive capability of the model by assessing the agreement between model output and experimental data. Validation experiments are therefore considered the standard against which the model outputs are to be compared.

Depending on the intended purpose, there are a wide variety of possible validation experiments, which can differ in terms of the physical phenomena involved, complexity, scale, metric, standardization, reproducibility and additional aspects. An overview of different activities relating to the validation of models for fire safety engineering purposes is given by van Hees [16]. He concludes that "excellent activities have been conducted over the past decades but that more work can be done in order to obtain overall uncertainties and error estimates of fire models." Although many fire experiments have been published, most of them lack a sufficient description and are thus impossible to use for validation. Also, data on reproducibility and repeatability are only rarely provided.

An experimental study, which needs to be mentioned separately, was carried out in 1982 by Steckler et al. [46]. The experiments are generally referred to as "Steckler compartment experiments", and they investigated the flow induced by a simulated pool fire in a compartment. Therefore, 55 full-scale steady state experiments have been conducted with heat release rates from 31.6 kW to 158.0 kW. Due to their large extent and good documentation, the experimental results are still used to this day. The spill plume experiments in this thesis have also been inspired by the setup of these experiments.

Considering that FDS is one of the most widespread fire models, the published validation studies are too numerous to list here. The most systematic survey of validation work is provided in the respective validation guide of FDS [15]. Over several hundred pages, the results of numerous experiments are compared with simulation results from the latest version of FDS. Thus, the data is organized by output quantity in order to enable the user to assess the predictive capability of the model for a given quantity over a range of different experiments and scenarios. From all described experiments, only two apply particle image velocimetry (PIV) to measure the flow velocities. These two are the "Sandia Plume Experiments" [47] and the "Bryant Doorway Experiments" [48–50]. This is somewhat surprising, since with the increasing quality of numerical calculations the quality of the experimental data for validation must also increase. As Raffel states, "the experimental data of the flow field must possess high resolution in time and space in order to be able to compare them with high density numerical data fields" [17]. He recommends PIV as an appropriate measurement technique for this task, especially if instantaneous velocity data is required.

The basic theory of particle image velocimetry (PIV) was developed approximately 25 years ago, and important contributions have been made by Keane and Adrian, among others [51, 52]. In PIV, a flow is seeded with tracer particles, illuminated by a pulsed laser light and photographed with a high-speed camera. This yields a series of image pairs. After subdividing the images into interrogation windows, spatial cross-correlation is used to obtain the average particle displacement and fluid velocity within each interrogation window [53]. A more detailed description of the technical aspects of PIV is given in Section 2.2. First, however, an overview of validation experiments for fire simulation with the application of PIV is provided. This list is not meant to be exhaustive but should cover the most important experimental studies carried out to date.

To the author's knowledge, one of the first fire experiments that used PIV to measure flow velocities was conducted in 1996 by Zhou and Gore, who studied the entrainment of air and the flow patterns in pool fires [54]. Others followed and used PIV to, for example, characterize the flow of flickering methane/air diffusion flames [55], or to investigate the dynamics of a large turbulent buoyant helium plume within ambient air [47]. In some studies, the PIV measurements were accompanied by sophisticated temperature measurements, e.g. Funatani et al. carried out simultaneous measurement of temperature and velocity using two-color laser-induced fluorescence (LIF) combined with PIV, with a color CCD camera [56].

A modification of PIV was proposed by Zhou et al. and Sun et al. to measure gas velocities inside of buoyant diffusion flames [57, 58]. In order to achieve this, they used virtual thermal particles determined via thermal infrared imagery, instead of real physical particles. This measurement technique is therefore referred to as thermal particle image velocimetry (TPIV). Husted et al. used the water droplets of a high-pressure water mist system as particles and compared the PIV measurements to phase Doppler anemometry (PDA) measurements [59, 60]. In this study, the velocity of the water droplets themselves was of interest, therefore the surrounding air was not seeded.

The scale of the measurement region differs significantly depending on the objective of the investigation. An experimental study of limit lean methane/air flame in a standard flammability tube recorded an area of only a few square centimeters [61], while an investigation of the flame front spreading across vegetative fuel recorded a measurement region of several square meters [62, 63].

An extensive study on fire-induced doorway flows was carried out by Bryant [48–50, 64]. He applied stereoscopic PIV measurements to the doorway of an ISO 9705 room to measure the flow into an enclosure containing a small fire. Such conditions would be characteristic of a room prior to flashover. Simultaneously, velocity measurements with bi-directional pressure probes were taken for comparison, and the gas temperatures were recorded with thermocouples. The experiments were conducted in real-scale, and a gas burner with a heat release rate of 32 kW to 160 kW was used as a heat source in the center of the room. As tracer particles gas filled, hollow plastic spheres were constantly injected into the inflow. Unfortunately, the tracer particles were unable to resist the high gas temperatures in the outflow, so only the flow into the compartment could be measured with PIV. Nevertheless, the experiments made an important contribution to the application of PIV in real-scale fire tests and provided insight into the accuracy of the commonly used bi-directional pressure probes.

A recent study investigates the fire-induced doorway flows in a similar setup but in reduced scale [65]. It also applies a gas burner as a heat source but uses reduced heat release rates of 10.6 kW to 21.7 kW. The study aims to provide validation data for RANS simulations with the CFD fire model ISIS [66].

2.1.4 Introduction of FDSgeogen

In the following section FDSgeogen is introduced. It is a tool that facilitates the simultaneous setup and evaluation of multiple FDS simulations, and it has been used for the validation studies in this thesis.

As already stated in the introduction, fire modeling based on computational fluid dynamics has become state of the art in fire safety engineering over the last fifteen years. The available computational power has increased dramatically during this period. Nowadays, it is not only possible to use more sophisticated sub-models and increase the spatial and temporal resolution, but it is also viable to run a great number of simulations in order to better understand the system under investigation. However, despite being one of the most popular tools for fire simulation, FDS lacks functionality for automated batch processing.

This is the case, although a number of possible applications for such functionality exists. For instance, the design of a metro station might require the consideration of different stopping positions for a subway train on fire. Therefore, it would be helpful if the train's position could be changed by one single parameter in the simulation instead of having to move each component of the train manually. Or, thinking one step further, one might want to vary not only the train's position but also other factors (e.g. natural airflows, ambient temperature, smoke exhaust systems, etc.) in order to carry out a thorough sensitivity study as presented by Schröder et al. [67]. Therefore it might be necessary to import external parameter sets, to apply various design of experiment methods, or to structure and facilitate the post-processing in advance. While there is a proprietary program (PyroSim [68]), which can assist with the first task, it is not applicable for automatization and batch processing, as it would be required for the second task. That is why the new tool FDSgeogen [69] was developed at Forschungszentrum Jülich [70]. Among other things, it enables the user to automatically generate FDS input files implementing freely selectable variables, e.g. for material properties or geometrical measures.

Another application, for which the author of this thesis could derive benefit from FDSgeogen, was the automated generation and evaluation of FDS simulations for optimizing parameters [71–73]. In that work, FDSgeogen was embedded in an automated workflow for optimizing thermophysical and kinetic parameters on various scales, in order to find a parameter set that best fits the ignition and burning behavior of polyurethane foam. Although the desired goal proved too ambitious, it worked flawlessly on a technical level.

In this thesis, FDSgeogen is utilized for automatically creating the FDS input files with variable heat inputs, ambient temperatures, door widths, or grid resolutions. Instead of setting up one FDS input file for each of the simulations, it is sufficient to set up and maintain one FDSgeogen input file for all simulations. This is particularly helpful, since setting up a simulation requires several iterations and improvements before a final version is reached. Therefore, unnecessary work and sources of error can be avoided by maintaining only a single file. The setup of every simulation is described in the respective chapter; however, the basic principle of FDSgeogen is explained in the following section to provide a general understanding.

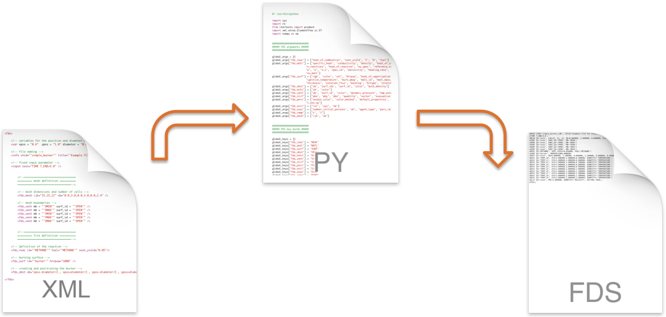

Figure 2.1: FDSgeogen workflow in principle.

Basic principle

FDSgeogen consists of two basic components: An input file that is written in Extensible Markup Language (XML) format and a Python interpreter that evaluates the XML syntax and generates an FDS input file (see Figure 2.1). The basic idea is to replace the conventional FDS syntax with XML syntax which has all the powerful advantages that result from the interpretation via Python. Beneficial features of this approach are, for instance, the utilization of algebraic operations, loops, if statements, or data sequences. That is why the presented method provides a great deal of flexibility and adaptability for the automatic input file generation for different applications. In this respect, both the complete generation from scratch as well as the modification of existing FDS input files are possible.

The XML input file for FDSgeogen contains most of the relevant information about the setup of the simulation, the boundary conditions, and the output values. Therefore it may seem similar to an FDS input file. However, in combination with the Python interpreter, it provides much more flexibility. For example, it is possible to include freely selectable variables and make them dependent on each other. Furthermore, a parameter file can be read in, in order to automatically set up a number of simulations. This file contains the parameter sets for the various simulations and is usually formatted as comma-separated values (CSV). This feature is illustrated in Figure 2.2 and will be used for the validation studies presented later.

FDSgeogen is freely available; interested readers are invited to make use of the presented method and participate in further development. More information on obtaining access to the code, annotated examples, and documentation are provided on the project's website:

`https://cst.version.fz-juelich.de/l.arnold/fdsgeogen`

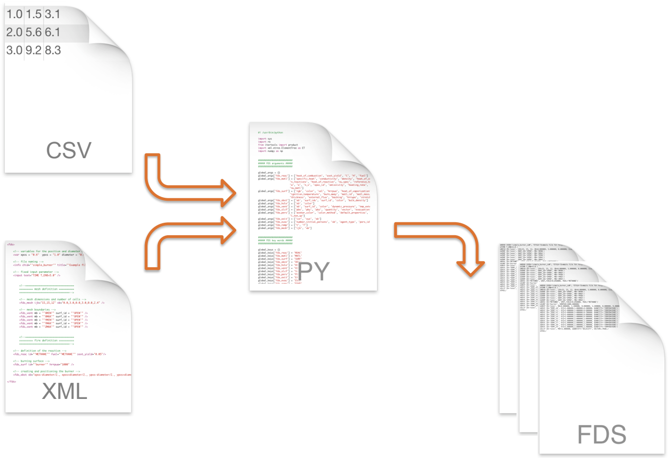

Figure 2.2: Reading in parameter files in FDSgeogen.

2.2 Particle image velocimetry

Particle image velocimetry (PIV) is a technique for measuring flow velocities of a gas or a liquid by seeding it with particles. These particles are illuminated by either natural or by artificial light, and within a very short period of time two subsequent images are taken. From these images, the displacement of the particles can be determined, which allows the calculation of the particle velocities in combination with the time shift between the two images. A schematic representation of a classical PIV system is shown in Figure 2.3. PIV is an indirect measurement method where the underlying assumption is that the particle movement coincides with the movement of the surrounding fluid. For this to be the case, the particles have to fulfill certain criteria, which are explained in Section 2.2.1.

Using PIV for experimental flow measurements offers a number of benefits. It is a non-intrusive technique, i.e. the flow is completely undisturbed apart from the added particles, whose influence can be considered negligible in most cases. It is a whole field technique [17], meaning not only a single location but a whole region of interest can be analyzed at once. Thus it is possible to capture interesting flow structures, e.g. entire eddies in a turbulent flow. PIV measurements provide almost instantaneous information about the flow with a precision that is not achievable when using classical measurement techniques such as bidirectional probes or hot wire anemometers. While classical PIV makes it possible to capture the two velocity components

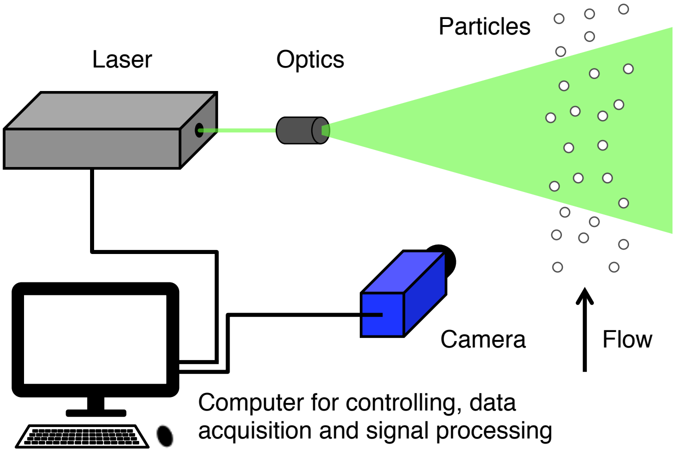
Particles
Laser
Optics
Camera
Flow
Computer for controlling, data acquisition and signal processing

Figure 2.3: Schematic representation of a 2D PIV system. Illustration based on [64].

parallel to the two-dimensional light-sheet, stereoscopic or tomographic PIV facilitate the measurement of all three velocity components in the region or even a volume of interest.

However, the high cost and complexity of such measurements are the main drawbacks. The required equipment usually has to be specifically designed for PIV and can therefore be very expensive. Familiarizing oneself with methods for measuring and post-processing, as well as setting up and calibrating the equipment, demands a great deal of time and effort. Accessibility of the experimental region can become an issue, because both the laser and the camera need optical access. On the other hand, either an enclosure around the experiment is needed to confine the particles or a constant, well-distributed supply of fresh particles needs to be guaranteed. Also, the lasers usually applied in PIV pose a potential hazard to experimenters, bystanders and equipment and therefore safety measures need to be taken.

The most important components of PIV systems are explained in the following paragraphs. It is a very complex measuring technique, so only those aspects which are essential for the understanding of the experiments conducted in this thesis are covered. For further reading on the topic, there are numerous publications available that cover the different subsystems of PIV, such as particle seeding, illumination, imaging optics, or post-processing. A good starting point for an interested reader might be [74,75]; a more extensive guide to PIV is [17].

2.2.1 Particles

The two main requirements of particles used for PIV are good visibility and good flow-following characteristics. For the experiments in this thesis, small liquid droplets of di(2-ethylhexyl)sebacate (DEHS) are used with particle sizes of approximately 0.2 µm to 0.3 µm [76]. The visibility of these particles is based on the light scattering at the interface of ambient air and DEHS. As a general rule, the greater the difference of the refractive indices of the involved materials and the larger the particles, the better is the visibility of the particles.

On the other hand, it has to be guaranteed that the particles "faithfully follow the motion of the fluid" [17]. Because, after all, the fluid velocity is only indirectly measured by measuring the particle velocity. In order to ensure slow sedimentation of the suspended particles, their density ought to be similar to the fluid density, or the particle size has to be small enough to result in a settling velocity that is negligible compared to the fluid velocity.

According to [74] and assuming the process is governed by Stokes drag, the settling velocity $v_{p,\infty}$ can be calculated by

$$v_{p,\infty} = \frac{g d_p^2 (\rho_p - \rho_f)}{18 \mu_f}, \tag{2.3}$$

with d_p and ρ_p as diameter and density, respectively, of the suspended particles, and μ_f and ρ_f as dynamic viscosity and density, respectively, of the surrounding fluid. This relation is valid for spherical objects that move through a viscous fluid at a small Reynolds number ($\mathrm{Re} \ll 1$) and can be used to estimate particle characteristics. The Equation 2.3 results in $v_{p,\infty} \propto d_p^2$, which means that a small particle diameter is beneficial for slow deposition of particles. In summary, "the choice of optimal diameter for seeding particles is a compromise between an adequate tracer response of the particles in the fluid, requiring small diameters, and a high signal-to-noise ratio (SNR) of the scattered light signal, necessitating large diameters" [77].

A uniform seeding size is desirable to obtain a uniform light intensity from all particles. A number of devices have therefore been developed, see [77] for further details. Also, a homogeneous particle distribution within the region of interest is required. An insufficient particle concentration would not provide enough information for vector calculations; concentrations that are too high make the particles difficult to distinguish. Depending on the experimental conditions, the stability of the particles under the influence of heat or chemicals has to be considered, too. Both liquids and gases as well as solid particles are used for experimental applications with PIV. Also,

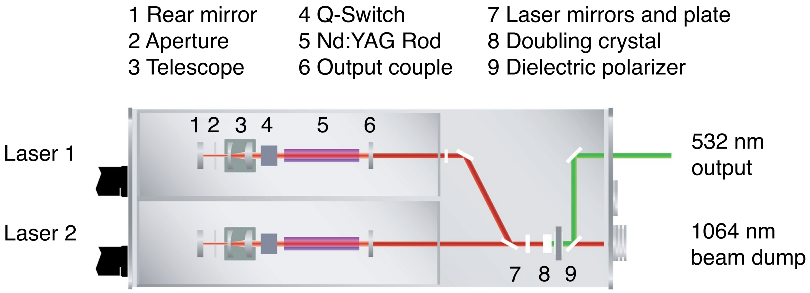

Figure 2.4: Schematic representation of a Nd:YAG double pulsed laser with bandpass filter for PIV. Illustration based on [78].

the particle size can vary substantially; an overview of the different kinds of particles used for PIV is given in [74].

2.2.2 Illumination

When taking images of a fluid at a high velocity, a short exposure time is needed to "freeze" the particles and obtain sharp images. In order to guarantee adequate illumination despite the short exposure time, a high-energy light source is required. Also, the time delay (also called pulse separation time) between the two light pulses needs to be very short so that the particles only move a few pixels between the two shots.

Nowadays, lasers are often used for PIV because they meet the requirements listed above. Additionally, they provide monochromatic light, which allows the use of optical filters for the cameras to further improve the image quality. The most common laser type used is a neodymium-doped yttrium aluminum garnet (Nd:YAG) laser in pulsed mode [17]. A schematic representation is shown in Figure 2.4. Because these lasers typically emit infrared light at a wavelength of 1064 nm, a doubling crystal is used to create a laser beam at 532 nm wavelength, which is visible to the naked eye as green light. This measure simplifies the laser calibration and reduces the danger of unnoticed exposure to laser light. The latter is important because most of the lasers used for PIV are classified as Class 4. This means both indirect and direct laser light can burn the skin and cause permanent eye damage.

In order to obtain pulse separation times shorter than the pulse frequency of a single laser, two lasers are coupled. The principle is illustrated in Figure 2.5. In this way, pulse separation times in the order of microseconds

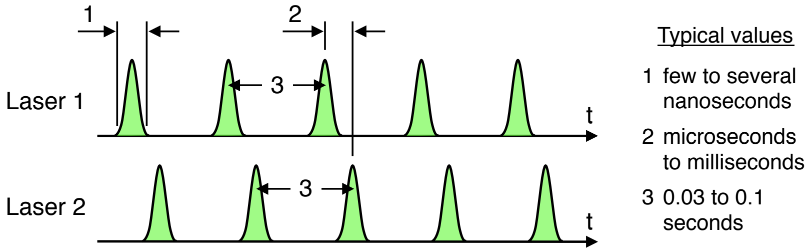

Figure 2.5: Staggered pulse trains from double pulsed lasers for PIV. Illustration based on [74].

can be realized. When working with two lasers, special care has to be taken to ensure that the two light sheets exactly overlap inside the measurement region. A lack of accurate calibration can lead to poor correlation between the two images and thus unsatisfactory results [74].

The laser beam is guided to the measurement area by mirrors or fiber optics and subsequently fanned out into a light sheet by an arrangement of lenses. An exemplary configuration for light sheet optics is shown in Figure 2.6. The light sheet at the measurement domain has to be very thin, so only particles are illuminated, which are focused by the camera. Furthermore, a homogenous light intensity over the entire region is desired for an even illumination of all particles.

2.2.3 Recording unit

During the early days of PIV, analog cameras were used for imaging. For certain aspects, this technique is still able to compete with more recently developed digital imaging, e.g. in terms of image resolution. However, the convenience and speed-up that comes along with digital imaging has resulted in the almost exclusive use of digital cameras. Digital images are immediately available and thus allow for fine-tuning during the recording process. Also, photochemical processes can be avoided and no digitalization for post-processing is required [17]. The most common sensor architectures available today are charge-coupled devices (CCD), charge injection devices (CID) or complementary metal-oxide-semiconductor devices (CMOS). CCD sensors, which are also used in most consumer-grade cameras, are more sensitive to light than CMOS sensors, which are very fast and thus used for high-speed PIV. A comparison of different sensor types for digital cameras and their performance can be found in [79].

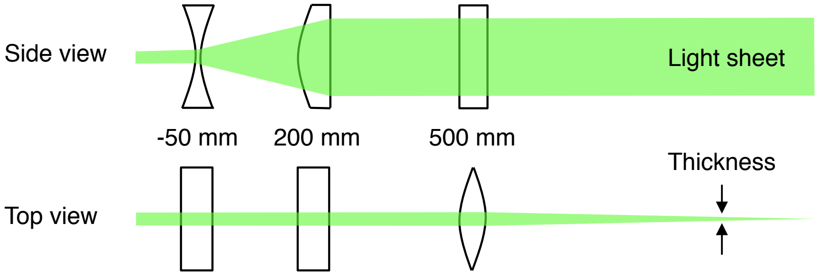

Figure 2.6: Light sheet optics using three cylindrical lenses. Illustration based on [17].

The two main factors for selecting the camera are resolution and speed. An increase in resolution makes it possible to either increase accuracy within the measurement region or to enlarge the measurement region while maintaining the same accuracy. For the most precise particle localization, the camera setup, resolution and particle size should be chosen in such a way that one particle is recorded on four pixels of the cameras sensor. The intensity distribution of a particle image may then be used to estimate its position with sub-pixel accuracy by means of the Gaussian function. In this manner, an accuracy of more than one-tenth of a pixel can be achieved. If a particle is recorded on a single pixel only, a "peak-locking" effect may occur. This means that sub-pixel accuracy is lost and the particle displacement tends to be biased towards integral values [17, 75].

The minimum time between two subsequent frames, the interframe time, is an important parameter when it comes to measuring flows at high velocity. For an accurate and reliable calculation of the velocity vectors, the particle displacement should only be a few pixels between two subsequent frames. Therefore, the interframe time for measuring super or hypersonic flows needs to be extremely short. Current high-speed cameras can capture more than 25,000 frames per second at full resolution with an interframe time of only a few hundred nanoseconds [80]. Of course, for experiments with lower velocities, the interframe times are much longer and other aspects can become more important. Further technical requirements regarding the recording unit are discussed in [17].

2.2.4 Processing and evaluation

The key component of a PIV system is the control and processing unit. It synchronizes the triggering of the laser and camera and facilitates the derivation of displacement vectors from the particle images. The images are therefore subdivided into interrogation windows (sometimes called interrogation areas) with typical sizes of 32 pixels × 32 pixels or 64 pixels × 64 pixels. For every interrogation window, a single vector is derived by calculating the displacement of the particles within the interrogation window; see Figure 2.7.

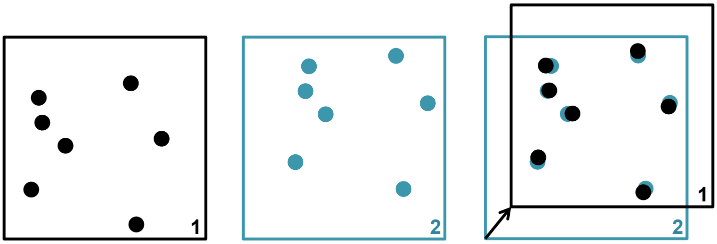

Figure 2.7: Cross correlation for determination of velocity vectors. The highest correlation between frame 1 and frame 2 yields the average particle displacement. Illustration based on [81].

Thus, in contrast to particle tracking methods, where individual particles are followed, in PIV the displacement of entire groups of particles is evaluated [75]. The applied method is cross correlation technique. For every possible shift dx and dy, the correlation between the two frames is calculated as shown in Figure 2.8. The location of the maximum of this correlation yields the average in-plane displacement of the particles. In combination with the known interframe time, the v_x and v_y components of the flow velocity can be derived from this average in-plane displacement [52].

Regarding the particle concentration, a number of approximately 15 particles per interrogation window is indicated in the literature to be an optimal value [51, 77, 83]. The optimal interframe time is directly dependent on the flow velocity. A particle displacement of less than a quarter of the interrogation window size is desirable ("one quarter rule"), because it ensures, on the one hand, a sufficiently large particle shift for a precise calculation without, on the other hand, losing too many particles to adjacent interrogation windows ("loss-of-pairs") [17, 51]. Further criteria to yield optimal performance of the PIV analysis include an out-of-plane displacement of less than a quarter of the in-plane displacement, and a velocity gradient over the interrogation area of less than five percent of the mean velocity [51, page 1214].

A careful adjustment of experimental parameters, as described above, is the basis for an accurate PIV analysis. However, there are also numerous methods available on the software side which may improve the quality of results. First of all, the images can be processed prior to vector calculation

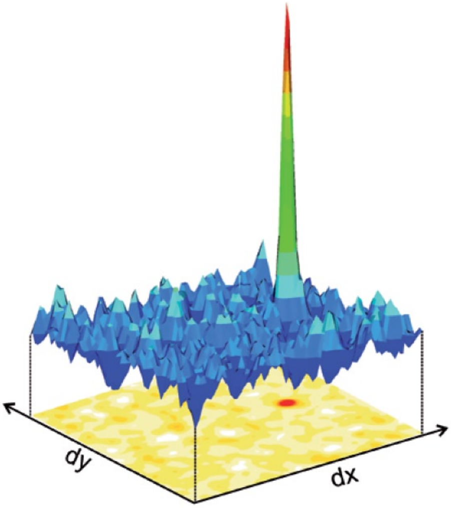

Figure 2.8: Composition of peaks in the cross-correlation function [82].

to enhance contrast, reduce noise, or to bring particle image intensities to a similar level [17, page 139]. For the experiments described in this thesis, background subtraction was conducted in order to reduce the effect of stationary disturbances on the images, such as reflected laser light. First, the background image was created by computing the minimum intensity image from all the recorded images. As a second step, this background image was then subtracted from each raw image. An illustration of this method is given in Section 3.1.3. Further methods for image pre-processing include high-pass or low-pass filters, image binarization, intensity capping, or dynamic histogram stretching. All of these methods can enhance image contrast; however, they also modify and potentially bias the image statistics. For further information see [17,83,84].

For the vector computation, a range of enhancement methods are available as well. A popular method, which has also been applied in this thesis, is an "iterative multigrid approach" as described by Scarano and Riethmuller [85]. It aims at reducing the loss-of-pairs due to in-plane motion by gradually reducing the size of the interrogation window. The vectors of coarse interrogation windows are thereby used as predictors for smaller interrogation windows, as illustrated in Figure 2.9. The smaller interrogation windows are no longer stationary between the two images, but they are instead shifted according to the predicted particle displacement. This is ad-

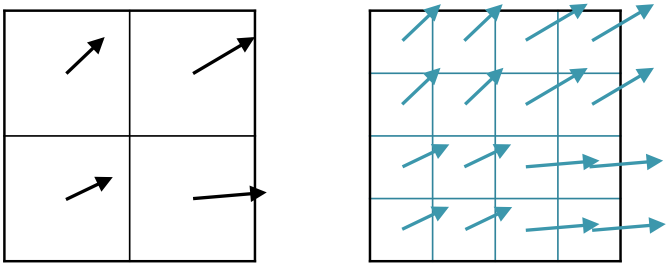

Figure 2.9: Vector computation via iterative multigrid approach. The coarse vectors (left) are used as predictors for vectors of smaller interrogation windows (right) at the same position. Illustration based on [85].

vantageous, because the one-quarter rule, related to the maximum in-plane displacement, no longer limits the window size and thus a better resolution can be achieved.

Defining an overlap of adjacent interrogation windows is another common measure. Typically 25 % to 50 % of the windows are made to overlap [74, page 60]. Such an oversampling increases the spatial resolution of the vector grid while retaining a sufficiently large number of particles per window for a reliable vector computation. There are methods available to avoid the redundant computation of the correlation function for overlapping areas [86].

2.2.5 Measurement accuracy

PIV measurements are generally considered to be very precise. However, as with every measurement technique, they contain several sources of error. Some of the most dominant causes are discussed in this section.

First of all, it is an indirect measurement method using the Lagrangian motion of the particles to approximate the instantaneous Eulerian flow velocity of the surrounding fluid [74]. The underlying assumption is that the particles move in accordance with the fluid. For this to be true, the particles have to meet certain criteria, as described in Section 2.2.1.

When it comes to image recording, inaccuracies can occur due to imperfections of the applied lenses as well as electronic noise when capturing and reading out data from the camera sensor. As described in the previous section, peak locking can occur if a particle is only resolved with a single pixel on the camera sensor. The particle displacement is then biased towards integral pixel values, and sub-pixel accuracy can no longer be achieved. Histogram plots of all the computed particle displacements for an experimental run can help to identify this type of error [17, page 168].

An inherent error of the vector computation based on two subsequent images is that it recovers linear shifts only. By definition, the cross-correlation method yields the displacement vector to the first order, i.e. the average linear shift of the particles during the interframe time. Deviations from the direct path cannot be captured [74, page 59]. This type of error is negligible, if the particle displacement is small or if the streamlines are relatively straight.

If the velocity gradient over the interrogation area is large, the cross-correlation method can also produce biased data. This is due to the in-plane loss-of-pairs, even if the mean particle displacement is accounted for by shifting the interrogation windows. In the latter case, the error will be random. If the interrogation windows are not shifted by the mean particle displacement, the result will be biased towards lower values, because especially fast moving particles will be lost for the cross-correlation [17, page 175].

In some of the interrogation windows a false correlation peak will be detected. This happens when the two correlated windows do not contain enough particle pairs, for example, due to a low particle concentration or an out-of-plane motion of the particles. The results are spurious vectors which may differ considerably from their neighbors, both in direction and magnitude. In order to obtain unbiased results it is necessary to eliminate and replace those vectors. A number of methods exists for this procedure, which is referred to as data validation [87, page 2]. Again, great care needs to be taken not to manipulate the data by deleting correct vectors.

In recent years, automatic uncertainty estimation for PIV has gained a great deal of attention, and several studies have been conducted on different sources of uncertainty and their effect on the achievable accuracy [87–93]. Some of these studies used synthetic particle images for the investigations. This is beneficial for studying selected parameters only. However, it cannot account for the manifold complexity of real experiments. The reported precision errors of numerical investigations are as small as 0.05 pixel [88, page 386] [83] or even 0.01 pixel under certain conditions [17, page 169]. In real experiments an empirical universal constant of 0.1 pixel is often used as a typical figure for measurement error [87, page 2].

Other methods try to quantify the measurement uncertainty using an a-posteriori approach. Sciacchitano et al. propose to estimate the error based on the obtained velocity fields in combination with the original particle images [87]. For every particle pair, a disparity vector is calculated, which is the difference between the real displacement of this very particle and the displacement vector calculated for the entire interrogation window. The scatter of all disparity vectors gives an estimate of the random error, and the mean value of the disparity vectors gives an estimate of the systematic error.

Concluding the above discussion, it becomes clear that PIV is a complex measurement technique that requires careful application. However, many of the potential sources of uncertainty are only relevant for sophisticated experimental setups with three-dimensional flows. In the experiments conducted in this thesis, the flows are predominantly two-dimensional, parallel to the light sheet, and the gas velocities are moderate. Nevertheless, the measurement uncertainty will be evaluated in the experiments.

Chapter 3

An undisturbed buoyant plume above a heat source

Many experiments in fire safety engineering involve pyrolysis and combustion, or even interaction with fire-extinguishing systems. Modeling those experiments is a difficult and complex task, which can exceed the limits of FDS applicability. Often, consistency of model and experiment can only be attained after extensive optimization or adjustment of either material or model parameters. Moreover, if no consistency is attained, the number of involved physical phenomena makes it difficult to localize possible reasons for the deviations or assign inaccuracies to specific sub-models.

Therefore the experiments described in the following two chapters are intended to be as simple as possible in order to obtain a valid and reliable data basis for model validation. They focus on one of the key components for fire simulation: modeling buoyancy-driven flows. Buoyancy is the main driver for the spread of smoke and toxic gases from fires, but it can also be exploited for natural ventilation and for establishing a low-smoke layer for the safe egress of occupants. Pyrolysis and combustion are neglected in the experiments; instead, an electrically heated block of copper is used as a heat source. The experiments are carried out on a bench-scale in two different geometries. In this chapter an undisturbed plume above an electrical heat source is analyzed. In the following chapter the same heat source is placed inside a simplified compartment with a single opening, and the flow through the opening is analyzed. In both experiments PIV is applied for measuring the flow velocities. The basic principles of PIV have already been explained in the previous chapter; the different experimental setups and respective simulations are described in the following sections.

3.1 Experiments

In these experiments the focus lies on the undisturbed buoyant plume that develops above the heat source. Surrounding air is heated by the heat source and rises due to its positive buoyancy compared to the ambient air. There is neither forced convection nor an enclosure, apart from a 650 mm tall box, which is required to confine the tracer particles. In the course of the experiments temperature stratification develops due to the buoyancy of the warm air. The PIV measurements are carried out as soon as a steady state is reached and the temperature stratification does not change. In this case the same amount of heat which is brought in by the heat source is lost through the outer enclosure walls and ceiling. They function as a heat sink for the gas volume inside the enclosure. The flow velocities within the plume are measured at four different power settings. Additionally, gas temperatures are recorded at various positions in order to quantify the boundary conditions of the experiments. A detailed description of the experimental setup is given in the following section.

The technical equipment for PIV as well as guidance on its use has been provided by IEK-6, a sub-institute of the Institute for Energy and Climate Research of Forschungszentrum Jülich. In preparation of the experiments, two bachelor theses have been written, which cover preparatory experiments and simulations in a very similar setup [94, 95]. The experimental work described here has been summarized in a paper submitted to the International Journal of Heat and Mass Transfer [96]. Several paragraphs and figures from this section have therefore been literally or textually incorporated into the paper.

3.1.1 Experimental setup

The lasers applied for illumination are classified as class 4 lasers. This means the laser light can ignite combustible materials and burn the skin, and even scattered or indirect light can cause serious and permanent eye damage. This is why the whole experimental setup needs to be located inside a laser safety box in order to protect the experimenters, bystanders, and the equipment. The laser safety box is 3.0 m long, 2.0 m wide and 2.1 m high, a picture is shown in Figure 3.1.

Experimental geometry and temperature measurements

In order to confine the particles and to guarantee defined boundary conditions, an enclosure made of polymethyl methacrylate (PMMA) slabs is used,

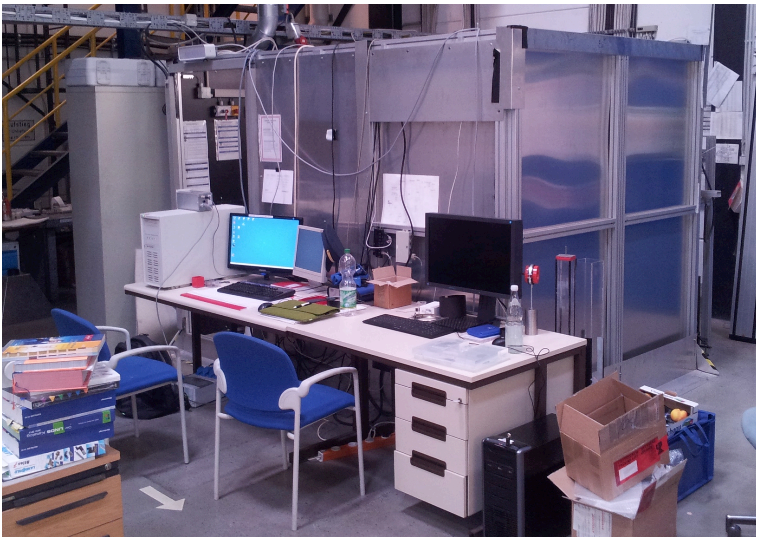

Figure 3.1: Laser safety box and computers used for the PIV measurements.

also known as acrylic glass. It is 735 mm wide, 575 mm deep, and 650 mm high (inner dimensions) and constitutes the experimental space for both the open and spill plume setup. Figure 3.2 gives a schematic representation of the whole experimental setup. Outside this enclosure only the temperature is measured in order to obtain realistic back wall conditions for the later simulations. The PMMA slabs for the walls and ceiling of the enclosure are 5 mm thick, and for the base plate a 12 mm thick board of plywood is used. Two holes in the base plate are used as particle inlet and exhaust port respectively. A closable opening on the left side of the enclosure allows access, even after the instrumentation has been set up. The enclosure as well as all the optical equipment are set up on an optical table, or where this is not possible, rigidly connected to it. The latter is necessary for the laser and cameras, because there is not enough space on the table. Such an optical table provides a stable, rigid and vibration-free platform for optical experiments. A rectangular grid of tapped holes on the tabletop makes it easy to fix and align the required equipment in almost any position.

For measuring the gas temperature platinum resistance thermometers (Pt100) are used. Compared to thermocouples they provide more precise and stable results, which improve the accuracy of the experiments. Advantages of thermocouples, such as a higher temperature resistance and a shorter

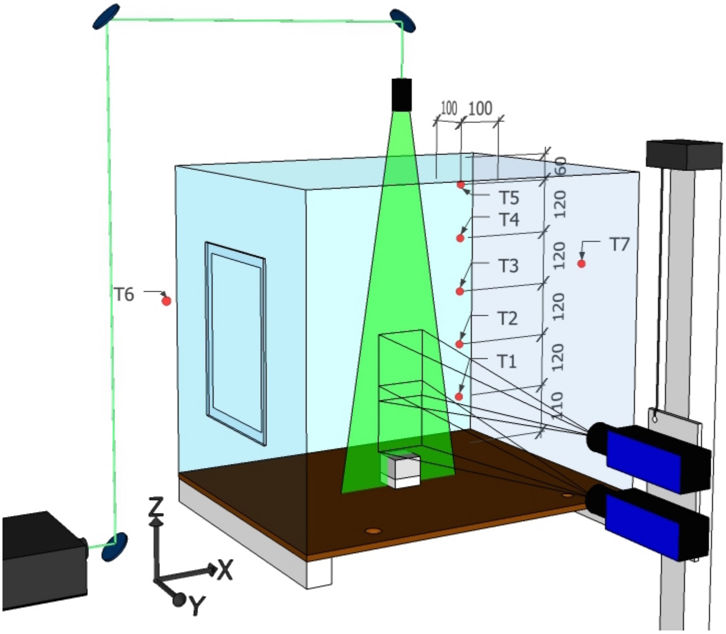

Figure 3.2: Experimental geometry: The heat source is placed in the middle of an enclosure, which is required to confine the particles. Temperatures are measured at positions inside and outside the enclosure (T_1 to T_7). The laser light sheet (green) illuminates a vertical plane along the plume axis. Both cameras can be driven upwards in order to capture the entire plume. Dimensions are given in mm, the coordinate origin is defined at the center of the top surface of the heat source.

response time are not relevant here, because only moderate gas temperatures at a steady state are investigated. Ambient temperatures are measured on either side of the enclosure with a few centimeters distance from the enclosure walls. Inside the compartment the temperature stratification is measured. For this purpose five Pt100 devices are placed above each other in one corner of the enclosure; the distance to both adjacent walls is 100 mm. The uppermost device is placed with 60 mm vertical distance to the ceiling; the other devices line up underneath with a vertical distance of 120 mm to each other. Hence the bottom device is positioned 110 mm above the base plate. The devices are brought into the enclosure parallel to the expected thermal stratification, i.e. along the isotherms. In combination with the minor difference in temperature between the inside and the outside of the enclosure, the measurement error due to heat flux to the exterior is expected to be very low.

Heat input

The heat source as well as the room geometry for the second setup have been constructed with a Cartesian grid with 10 mm resolution in mind. This is advantageous for recreating the setup in CFD models with Cartesian grids, such as FDS. In this way the geometry can be represented without having to neglect any geometrical details. The dimensions of the heat source are 60 mm × 60 mm × 40 mm ($l \times w \times h$), see the technical drawing in Figure 3.3. A heating coil and a thermocouple are embedded inside the block of copper.

When planning the experiments the heat source was meant to be kept at a constant temperature by automatically switching the electrical heating on and off. For automatic temperature control the embedded thermocouple reading was to be used. However, this approach led to fluctuating surface temperatures and made it difficult to measure the electrical power. Instead, a constant voltage was applied in the final experiments, which resulted in very steady surface temperatures after some time of heating up.

Another lesson learned during the preparations of the experiments was how quickly the copper surface oxidizes during experimental runs with higher surface temperatures. Since the emissivity of copper varies strongly with the surface quality, this would have an immediate influence on the radiative and convective fraction. With an increased emissivity at an identical heat input, more energy would be transferred via radiation and less energy would be transferred via convection. In order to prevent shifting emissivity during the experiments the copper block was coated with chalk spray from the outset. Because the emissivity of the chalk spray is known and constant throughout the experiments, it is possible to determine the radiative fraction of the

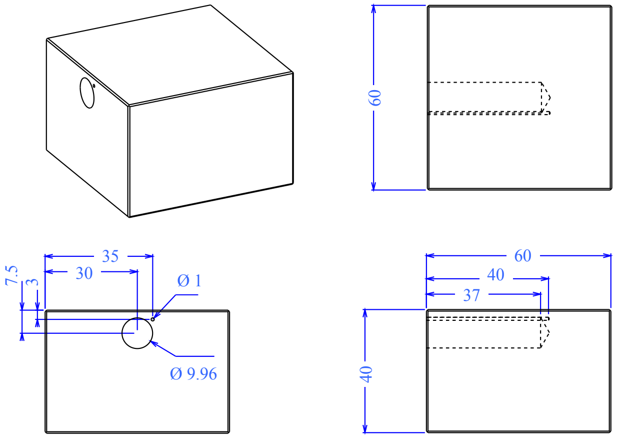

Figure 3.3: The heat source consists of an electrical heating coil and a thermocouple embedded in a rectangular block of copper. Dimensions are given in mm.

overall energy input. To measure the total energy input, P_{HS}, an ampere meter and a voltmeter are connected in series and parallel to the heat source respectively. It is assumed that 100 % of the electrical power are converted to thermal power. Figure 3.4 illustrates the relation of electrical power and surface temperature dependent on the surface condition of the heat source. With increased emissivity, the heat loss via radiation also increases. Thus the surface temperature at steady state conditions is lower. This is particularly true for higher surface temperatures when radiation becomes the dominant mode of heat transfer. Copper has a very high conductivity, and thus quick equalization of temperature differences and thus a homogeneous surface temperature can be expected. Nevertheless thermal imaging is applied in order to evaluate the homogeneity of the surface temperature. The results are presented in Section 3.1.4.

In addition to radiative and convective heat transfer, there is also conductive heat transfer to be considered. In order to reduce the heat loss to the wooden floor board a 20 mm thick base plate out of calcium silicate is used for insulation purposes. This material resists temperatures of up to 1000 °C and has a low thermal conductivity of around 0.09 W/m K [97]. It is sold under the trade name *Promatect L*. A small hole is drilled in the center of the insulating base so that the heat source can be screwed to the wooden ground plate to guarantee a fixed position.

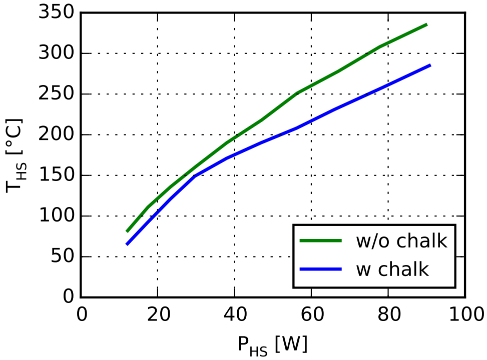

Figure 3.4: Heat source temperature depending on the surface quality. The uncoated block of copper has a low emissivity that varies with the level of oxidation. With a coating of chalk spray a constant emissivity of 0.82 is obtained.

Equipment for PIV

For illumination purposes a Dual-Nd:YAG Laser is used. It is marketed by *InnoLas* under the tradename *SpitLight PIV Compact 400*. Figure 3.5 shows a photograph of the laser head, although the power supply is not displayed. The following features are a selection taken from the *InnoLas* data sheet [98]:

- Repetition rate: 2 × 10 Hz
- Pulse energy at 532 nm: > 2 × 180 mJ
- Pulse width at 532 nm: 4 ns to 6 ns
- Beam diameter: 6 mm

As can be seen in Figure 3.2, the laser is positioned on the left side of the enclosure, although a vertical light sheet is required, which is aimed at the heat source from above. That is why the laser beam has to be deflected via a number of mirrors. In order to ease the alignment of the mirrors and to guarantee a highly focused beam the number of mirrors ought to be as small as possible. Here, three mirrors are used. The angle of each mirror can be set precisely via adjustment screws. Before entering the enclosure the laser beam is converted to a laser light sheet via light sheet optics. Not only the laser head but also the power supply is positioned on the left side of the laser

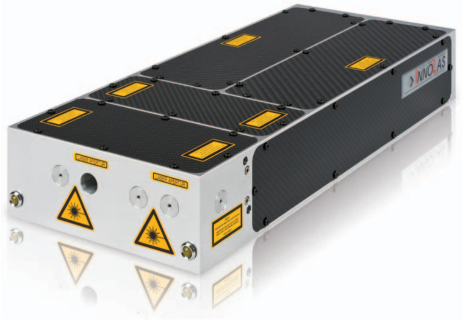

Figure 3.5: Picture of the applied Dual-Nd:YAG laser *InnoLas SpitLight PIV Compact 400* [98]. The two units for power supply are not displayed.

table. It is assumed that the exhaust heat of this power supply heated up the adjacent side of the enclosure during preliminary experiments, resulting in a skewed plume axis. For this reason an air exhaust is placed next to the power supply and a felt mat is placed between the power supply and the enclosure: see Figure 3.6. These measures prove useful to some extent. However, the plume axis is still skewed as will be shown in the experimental evaluations.

For the particle generation the *TSI Aerosol Generator Model 3079* is used [99] in conjunction with di(2-ethylhexyl)sebacate (DEHS) as raw material. It is a non-soluble, colorless and odorless liquid that boils at approximately 232 °C to 249 °C at 1 bar atmospheric pressure [76]. The lifetime of a particle with 0.3 µm diameter is given as four hours, but this will depend upon ambient conditions such as temperature and pressure. The typical distribution of particle sizes for the applied aerosol generator is shown in Figure 3.7.

Assuming an average particle size of 0.2 µm and air temperatures of 30 °C, the settling velocity can be estimated using Equation 2.3:

$$v_{p,\infty} = \frac{9.81\,\mathrm{m/s^2} \cdot (2 \times 10^{-7}\,\mathrm{m})^2 \cdot (912 - 1.15)\mathrm{kg/m^3}}{18 \cdot 18.718 \times 10^{-6}\,\mathrm{kg/(m\,s)}} \approx 10^{-6}\,\mathrm{m/s}, \tag{3.1}$$

This settling velocity is substantially smaller than the expected flow velocities of up to 1 m/s and thus negligible for the determination of the gas velocities when evaluating the experiments.

As recording devices two *LaVison Imager pro X 2M* cameras are used. The following list of features is taken from the *LaVision* data sheet [100]:

- 1600 pixels × 1200 pixels

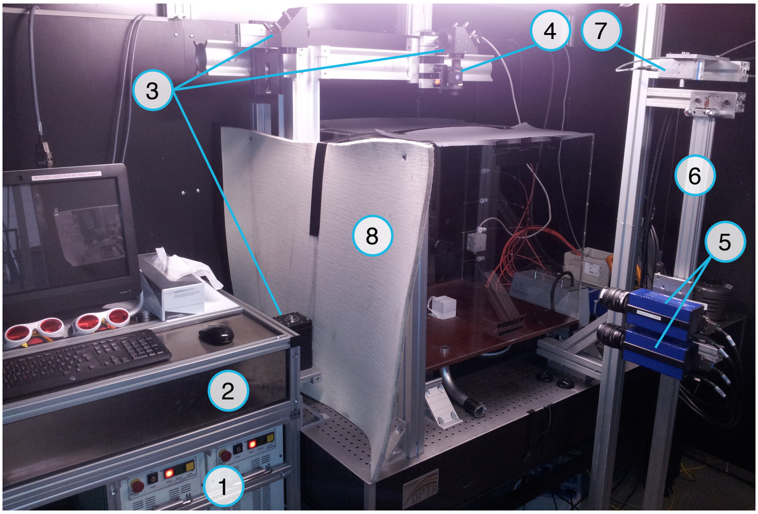

(a) Seen from the left.

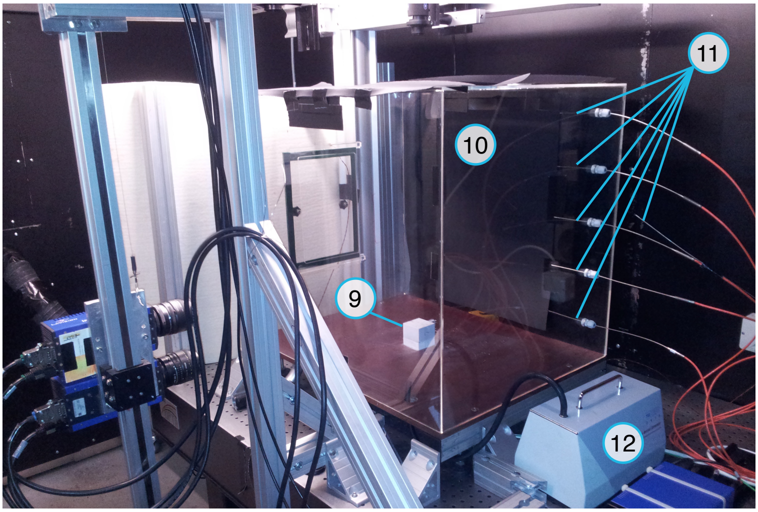

(b) Seen from the right.

Figure 3.6: Experimental setup of the open plume experiments. Shown are the laser power supply (1), laser head (2), mirrors (3), light sheet optics (4), CCD Cameras (5), linear drive (6), string potentiometer (7), felt mat (8), heat source (9), enclosure (10), Pt100 temperature devices (11), and the particle generator (12).

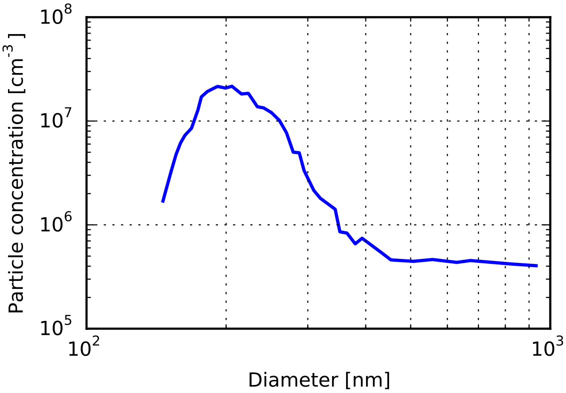

Figure 3.7: Particle size distribution of the used *TSI Aerosol Generator Model 3079* [99].

- 29 frames/s maximum frame rate
- 110 ns minimum interframing time

The two cameras are mounted on an aluminum base plate with a viewing angle perpendicular to the laser sheet. The viewing areas slightly overlap (29 mm) in order to allow for a common calibration of both cameras. The combined viewing area of both cameras together is 104 mm wide and 246 mm high. Thus the acquired images have a resolution of approximately 11.6 pixels per millimeter. Due to a rigid fixing to the base plate a misalignment of the cameras after calibration is prevented. The base plate itself is mounted on a linear drive, which allows the movement both cameras vertically, parallel to the laser light sheet. The linear drive can be seen in Figure 3.6. Special care has to be taken to ensure that the laser light sheet and the linear drive are parallel to each other, otherwise the cameras would lose the focus on the particles when being driven up or down.

The exact position of the cameras is measured via a string potentiometer. Preliminary experiments have shown that entering the laser safety box in order to manually adjust and measure the camera position takes too long and interferes with the constant experimental conditions. Therefore both the remote control of the linear drive and the display of the string potentiometer are accessible from outside the laser safety box. A detailed description of the experimental procedure is given in the following section.

3.1.2 Experimental procedure

After the experimental geometry and equipment described in the previous section have been built, set up, wired, adjusted and tested, only a few more preparations are necessary in the run-up for the experiments:

- Pictures for the camera calibration have to be taken. Therefore a calibration target needs to be placed at the exact position of the laser light sheet: see Figure 3.8. This target exhibits a regular grid of markers with a known distance from each other. In combination with the reading of the string potentiometer for the camera position the particle images can be calibrated precisely; see Section 3.1.3 for details.
- The background of the particle images - in this instance the rear wall of the enclosure - needs to be as dark and evenly colored as possible in order to make the particles easy to distinguish. For this purpose black cardboard is attached to the rear wall.
- Each camera position needs to be carefully checked for laser light reflections or refractions into the camera. These can occur when the laser penetrates the PMMA slabs of the enclosure, or when the light sheet strikes the heat source or other obstructions. In order to avoid damaging the cameras, such an incidence of light onto the sensor needs to be avoided. It is for this reason that the close-up range of the heat source cannot be investigated.
- Since different computers are used for recording the PIV images and temperature measurements, their internal clocks need to be synchronized.

In the short-term before the experiments, i.e. every morning during the experiments, the following measures are taken:

- The air exhaust of the laser safety box is activated. The extraction is placed directly adjacent to the laser's power supply to remove the heat generated and to prevent the laser safety box from heating up. The air supply is guaranteed by the aid of numerous openings at different positions in the outer wall of the laser safety box.
- The heat source is switched on and set to the first power setting. After approximately 20 to 30 minutes it reaches a constant temperature. However, in order to obtain constant gas and enclosure temperatures, another 60 to 90 minutes are allowed for the heat-up.

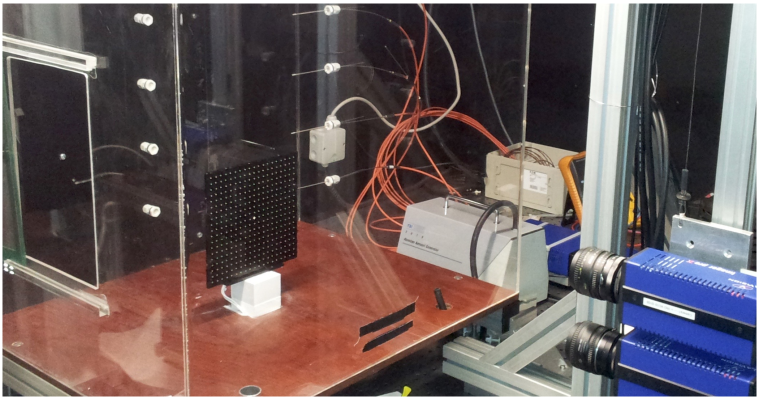

Figure 3.8: The target for the camera calibration is placed at the very same position as the laser light sheet.

- Particles are injected and spread quickly inside the enclosure due to the buoyancy-driven flow. The cameras are focused on the particles illuminated by the laser light sheet; some test PIV measurements are done in order to check the particle density and to ensure the functioning of the entire system.

After a sufficient time to attain the quasi-steady state the experimental procedure for recording one heat source power setting is as follows:

1. The readings of the heat source temperature, voltmeter and ampere meter are noted and the laser is started.

2. An appropriate interframe time for the measurements is determined via DaVis' integrated *dt optimizer* [101]. This tool iteratively changes the interframe time until an optimal particle shift of five pixels is obtained. The optimization is performed for the medium camera position, where the highest velocities are usually observed.

3. Starting at the bottom position, the measurement is triggered. After the images are recorded and stored, the cameras are driven to the middle position, 200 mm above the lowest position. This results in an overlap of 46 mm between the viewing areas of both positions. This requires approximately 60 s to move the cameras.

4. As soon as the middle position has been reached the next recording is

triggered. Afterwards the cameras are driven to the highest position, 155 mm above the middle position.

5. When the top position is reached, the measurements are triggered again.

6. Steps 3 to 5 are repeated in reverse order, i.e. the cameras are driven from top to bottom. This is done in order to obtain a second measurement of the full plume for comparison.

7. After finishing the PIV measurements and switching off the laser, the readings of the heat source temperature, voltmeter and ampere meter are re-checked to detect a possible shift throughout the measurement.

In the course of the experiments the quality of the data obtained and the particle density is checked periodically. Depending on the heat source temperature, particles need to be refilled after a few hours. The power supply of the laser is water-cooled. However, because the experiments were mostly carried out during warm summer days, the water temperature became critically high twice, which caused the power supply to shut off. This happened despite the exhaust air, which is placed close to the power supply to prevent excessive heating. The affected measurements were repeated after a short cooling off period. Another piece of equipment which heats up over time is the wooden base underneath the heat source. Despite the insulating plate of calcium silicate in-between, conductive heat loss has to be considered in the later simulations.

Table 3.1 gives an abridged overview of all open plume experiments, a complete overview is given in the appendix. Four different power settings, P_{HS}, from 30 W to 96 W are investigated, which lead to heat source temperatures, T_{HS}, from 149 °C to 307 °C. Due to radiative and convective heat losses, the surface temperatures of the heat source, $T_{HS,surf}$, are smaller than the internal temperatures T_{HS} measured by the embedded thermocouple. This is explained in more detail in Section 3.1.4. Measurements for identical heat source settings are repeated on different days to obtain an estimate of the uncertainty related to the measuring procedure. Most of the images are recorded over 10 s with 10 Hz, which is the highest frequency the laser can provide. Some measurements are recorded with 1 Hz over up to 180 s, in order to capture possible long term fluctuations. In total, 24 runs for the open plume setup are performed. By 'one run' a scanning procedure of the entire plume is meant, i.e. each run comprises camera recordings at the three different camera positions.

Table 3.1: Abridged overview over open plume experiments with different heat inputs, P_{HS}, and the associated standard deviation. N is the number of experimental runs, t_m is the duration of each measurement and f is the camera frame rate.

P_{HS}	T_{HS}	$T_{HS,surf}$	N	t_m	f
W	°C	°C		s	Hz
29.9 ± 0.2	149.2 ± 0.7	147.5	4	10	10
			2	117	1
55.6 ± 0.1	216.3 ± 1.9	212.1	4	10	10
			2	180	1
78.0 ± 0.3	270.7 ± 0.5	264.8	4	10	10
			2	180	1
96.0 ± 0.3	305.2 ± 1.1	298.0	4	10	10
			2	180	1

3.1.3 Image processing

The first step of the image processing and the basis for the later evaluation is to assign the correct calibration to the raw images. For the experiments described here this serves two main purposes. First, the results are required in true dimensions, e.g. mm, instead of pixels. Therefore the image scale needs to be determined. Secondly, the images may show some distortion due to the view through the PMMA enclosure or due to a slightly oblique view of the light sheet. Both of these can be corrected by correct calibration [102].

As described in the previous section and illustrated in Figure 3.8, a calibration target is used for this purpose. In order to create the calibration one needs to select three of the target's markers that are visible on both cameras. The other markers on the target are selected automatically by DaVis' semi-automatic calibration tool [102]. After the experimenter has checked the correct recognition of all the markers, the calibration is automatically calculated. In the course of the calibration process it is also possible to define the coordinate origin. Here it is defined at the center of the top surface of the heat source.

In order to generate vector fields from the images the following steps are carried out. Parts of this process can be automated by so called *hyperloops* in DaVis, which saves time and avoids the errors of manual execution.

1. The double-frames from both cameras need to be reorganized, because as defaults they are stored together in DaVis.

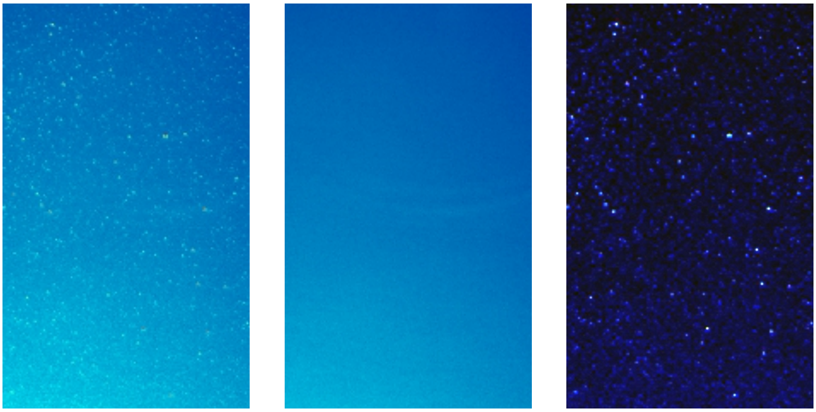

(a) Original (b) Background (c) Difference

Figure 3.9: Background subtraction for enhanced image quality. Illustrated by an image section taken from experimental run 1.1. The background calculates as the minimum intensity image of the entire image set at that position.

2. As described in Section 2.2.4, the image background can be subtracted from the images in order to enhance the image quality and particle visibility. Thus the minimum intensity image of all 100 (or 180) images is calculated and afterwards subtracted from every image, see Figure 3.9. By doing this, unwanted information can be largely removed, leaving only the particles. This method works well for disturbances on fixed positions, e.g. parts of the geometry or reflections on the enclosure.

3. For the vector calculation an iterative multigrid approach is used. The vectors of larger interrogation windows are thereby used as predictors for smaller interrogation windows, as described in Section 2.2.4. The interrogation window size is reduced from 128 pixels × 128 pixels to 64 pixels × 64 pixels. Additionally, an overlap of 50 % is prescribed between the interrogation windows. Such an oversampling increases the spatial resolution of the vector grid while retaining a sufficiently large number of particles per window for a reliable vector computation. Here a final resolution of approximately 2.75 mm is obtained.

As mentioned in Section 2.2.4, a particle density of around 15 particles per interrogation window is given as an optimal value in the literature. In Figure 3.10 a close-up of a single interrogation window is presented that seems to exhibit more than 15 particles. However, it should be noted that

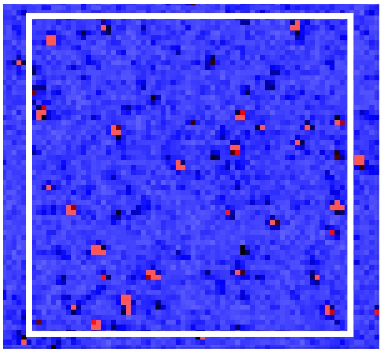

Figure 3.10: Close-up of a single interrogation window marked as a white rectangle with 64 pixels × 64 pixels, i.e. 5.5 mm × 5.5 mm. It is taken from run 1.1 and is plotted in false colors for illustration purposes.

the true number of particles is difficult to determine due to the wide range of different particle sizes (see Figure 3.7). Also, a different color scaling will make it appear as if the particle concentration changes. Even if absolute numbers cannot be determined from the image, it becomes apparent that both particle concentration and particle size lie within reasonable bounds. Most of the particles are large enough to be recorded on several pixels so that a peak locking effect is avoided.

After an evaluation of the generated vector fields it transpired that additional filtering methods for correcting erroneous vectors were not necessary. There are a few obvious errors on some of the frames. However, the overall rate of spurious vectors is very low. This is particularly the case when evaluating averaged vector fields, where single spurious vectors are of almost no consequence. This is why the average and standard deviation for every run is calculated without prior filtering.

Due to the limited viewing area of the cameras it is not possible to capture the entire plume at once; see Section 3.1.2 for a detailed description of the experimental procedure. Instead the plume has been recorded in three steps. That is why the recordings taken in different heights need to be merged in order to obtain an overall view of the plume. Additionally, the vector fields obtained from PIV only contain data at discrete positions, i.e. at the centers of the interrogation windows. For the later evaluation of the data it is advantageous to have interpolated values in between. Both requirements are implemented into an evaluation program written in *Python* [103, 104].

An exemplary time-averaged flow velocity field is shown in Figure 3.11.

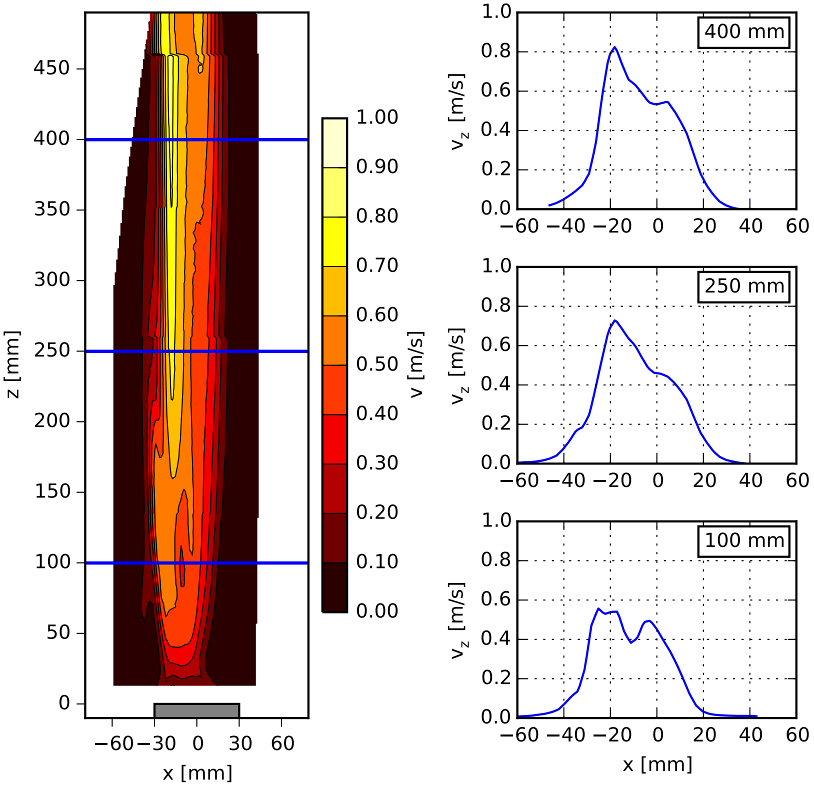

Figure 3.11: Flow velocity field and velocity profiles of run 1.1 with $P_{HS} = 30\,\mathrm{W}$ and $T_{HS} = 149\,°\mathrm{C}$. On the left hand side absolute velocities are displayed, time-averaged over 10 s and 100 doubleframes respectively. The horizontal blue lines indicate the positions of the velocity profiles shown on the right. For these profiles only the vertical velocity, v_z, is considered.

At the top left corner of the measurement area there is triangle of data missing, because the light sheet has not illuminated that area. For the areas within the velocity field, where the viewing areas of both cameras overlap, thus allowing duplicate data to exist, the recordings of the lower camera are used. The transition between camera positions is visible at $z = 260\,\mathrm{mm}$ and $z = 460\,\mathrm{mm}$. However, the flow is sufficiently stable for the velocity fields to be merged. For the velocity profiles on the right of Figure 3.11, only the vertical velocity component, v_z, is used. Those profiles are evaluated at three different heights: in the close range of the heat source (100 mm), at the top of the plume with some distance to the ceiling (400 mm) and between the two (250 mm).

3.1.4 Evaluation of experiments

Before the experimental results are presented, general observations will be described and the consistency of the ambient conditions analyzed.

General observations

It has been observed in the course of the experiments that both the insulating plate and the wooden floor underneath the heat source heat up over time. Although this effect is not quantitatively recorded, it should be considered when using the experimental data for validation purposes. On the one hand it reduces the energy brought into the enclosure by the amount lost via conduction through the floor. On the other hand, it might have an influence on the flow, if not only the heat source surface is hot, but also the insulating plate underneath. However, thanks to the low thermal conductivity of calcium silicate, the total amount of energy lost via conduction is expected to be low.

In some of the experiments, which have been conducted at higher power settings, areas with a low particle concentration are visible. These areas extend from the top surface of the heat source upwards into the plume and are most likely to be caused by an evaporation of the particles. As mentioned above, DEHS evaporates at temperatures of 232 °C to 249 °C, which is less than the maximum heat source surface temperature of around 300 °C. Although the surrounding air is far cooler than the heat source surface, the gas temperatures in the slipstream at the top of the heat source might exceed the boiling temperature of DEHS. Despite the low particle concentration it is still possible to determine valid vectors in most cases. However, this could influence the measurement uncertainty, which will be determined at a later stage.

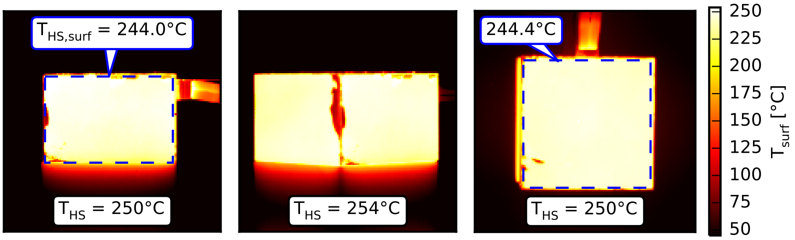

Figure 3.12: Thermal images of the heat source at an inner temperatures of $T_{HS} = 250\,°\mathrm{C}$ and $T_{HS} = 254\,°\mathrm{C}$ respectively (measured by the embedded thermocouple). From left to right, the view at one side, one corner and the top of the heat source is shown. The dashed blue line indicates the area, which is used for the determination of the surface temperature.

During many of the experimental runs the plume had a tendency to bend to the left (from the camera's viewpoint). A possible explanation for this could be uneven heating of the heat source. Although copper has a very high thermal conductivity, and thus a quick equalization of temperature differences can be expected, thermal imaging was applied to confirm this assumption. The thermal images have been recorded in collaboration with ZEA-1, a sub-institute of the Central Institute of Engineering, Electronics and Analytics of Forschungszentrum Jülich. For technical reasons the thermal images could not be recorded simultaneous with the PIV recordings, however, the identical experimental setup has been used. The images for heat source temperatures of $T_{HS} = 250\,°\mathrm{C}$ and $T_{HS} = 254\,°\mathrm{C}$ respectively are displayed in Figure 3.12. T_{HS} denotes the temperature measured by the thermocouple embedded inside the heat source and as displayed in Figure 3.3. It is clear that the surface temperatures are mostly homogeneous, with only a few colder patches visible probably resulting from an uneven coating with chalk spray, which tends to agglomerate close to the edges. Therefore the bending of the plume cannot be explained by non-homogeneous surface temperatures and requires further investigation. Possible explanations include an asymmetric cable routing outside of the heat source or asymmetric ambient conditions outside of the enclosure that lead to non-homogeneous enclosure temperatures.

What is evident from the thermal images, however, is a general deviation of the surface temperature, $T_{HS,surf}$, from the heat source temperature, T_{HS}, measured by the embedded thermocouple. When averaging across the indicated area in Figure 3.12 a deviation of around 6 K results for a heat

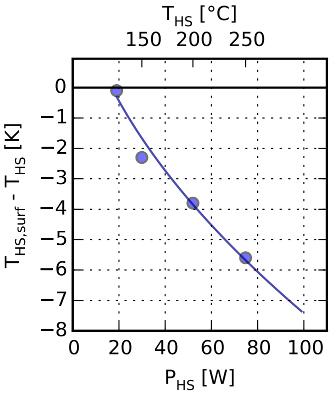

Figure 3.13: There is a deviation between the inner heat source temperature, T_{HS}, and the surface temperature, $T_{HS,surf}$, measured on top of the heat source. The blue line is a fitted function used for inter- and extrapolation.

source temperature of 250 °C. In Figure 3.13 the temperature deviations for different power settings are displayed. These deviations increase with higher heat source temperatures and can be explained by the cooling effect of convection and radiation on the outside. The thermocouple, on the other hand, is embedded close to the heating coil inside the heat source and thus displays higher temperatures.

Reproducability of experiments

The experiments were conducted over the course of several days. Furthermore, since for every power setting a number of experimental runs have been carried out for comparison – some of them on different days – constant ambient conditions are an important issue.

It has been found that keeping the heat source power constant is relatively easy. As can be derived from Table 3.1, the standard deviation is between 0.1 W and 0.3 W, which is 0.7 % at most. As a result, the heat source temperatures vary only slightly. On average the standard deviation is around 1 K. Figure 3.14 gives a detailed overview of the scattering of the heat source temperatures. For every power setting the deviation to the mean heat source temperature at that power setting is displayed.

It has been more difficult, however, to keep the ambient temperature within the laser safety box constant. In Figure 3.15 the ambient gas tem-

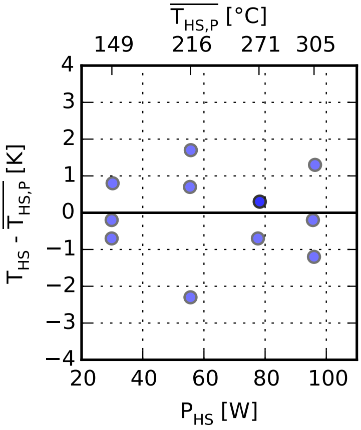

Figure 3.14: Scattering of heat source temperatures during the experiments. The figure displays the deviation of each heat source temperature, T_{HS}, from the mean heat source temperature at every power setting, $\overline{T_{HS,P}}$. Per power setting there are only three data points visible, because two runs have been measured in a row at identical heat source temperatures.

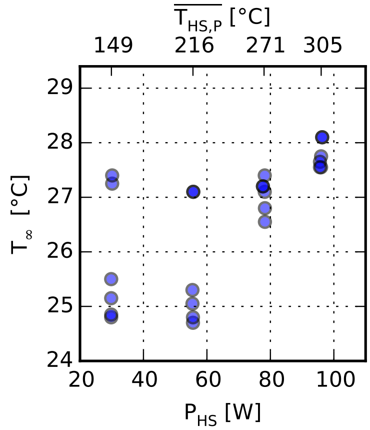

Figure 3.15: Ambient temperatures, T_∞, during the experiments. The measurement error is less than 0.4 K (not plotted for reasons of clarity).

perature, T_∞, during all experimental runs is shown. It is calculated as the averaged value of T_6 and T_7, measured within a few centimeters distance to the enclosure. There is a positive correlation with the power setting, because experiments at higher powers have been performed in the afternoons of the experimental days when the temperature within the laser safety box was increased. This increase was caused by the laser's power supply and a general heating up of the laboratory due to summer temperatures outside.

When comparing these temperature measurements one needs to keep the measuring tolerances in mind. The Pt100 temperature devices used are of tolerance class B and the measurement error is declared as $\pm(0.3 + 0.005 \times T)$, with the measured temperature T given in °C [105]. However, the error is expected to be lower, because the measurements are not taken at a single point in time but averaged out over a period of several minutes.

The gas temperatures inside the enclosure are mainly a result of the heat source temperature and the ambient temperature outside the enclosure. In Figure 3.16 the temperature profiles in one corner of the enclosure are given for the four different power settings. The coordinate origin is set to the center of the heat source top surface so that the enclosure's interior extends from $y = -60\,\mathrm{mm}$ to $y = 590\,\mathrm{mm}$. The formation of a hot gas layer in the upper part of the enclosure is clearly visible. However, the increase in temperature seems to be continuous, without a distinct interface between the

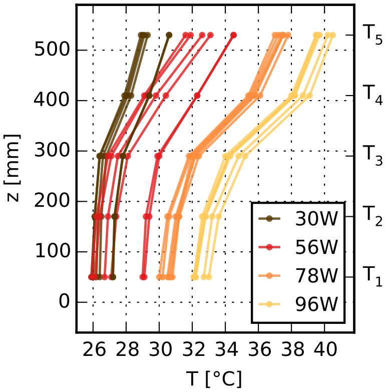

Figure 3.16: Temperature stratification inside the enclosure for different power settings, measured by the devices T_1 to T_5. The measurement error for this temperature range is less than 0.5 K.

hot upper layer and the cold lower layer. Similar variability in Figure 3.15 and Figure 3.16 can be found when comparing the scattering per power setting. For the power setting of 78 W and 96 W both the ambient temperatures outside the enclosure and the temperature profiles inside the enclosure exhibit very little scattering, which lies within the measurement tolerance.

Analysis of heat fluxes

During the experiments the total electrical power brought into the heat source is measured. When the heat source temperature no longer rises, i.e. steady state is attained, the same amount of power received by the heat source is emitted by it. This can happen via three fundamental methods of heat transfer, which are illustrated in Figure 3.17.

1. Convective heat transfer to the surrounding colder air.
2. Radiative heat transfer to the colder enclosure.
3. Conductive heat transfer to the insulating base of calcium silicate (Promat), which again transfers energy via convection, radiation or conduction to the surrounding air, the enclosure or the wooden floor respectively.

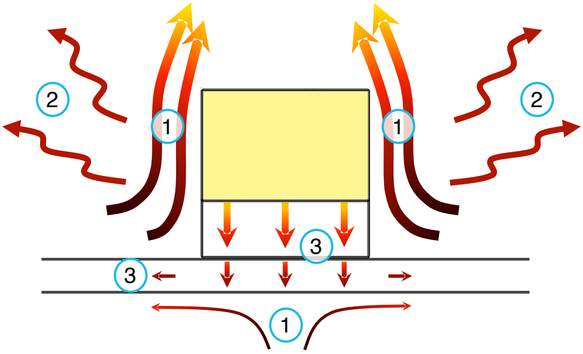

Figure 3.17: Schematic representation of the involved heat transfer mechanisms convection (1), radiation (2) and conduction (3).

The only direct driver of the buoyant plume is the convective heat transfer to the surrounding air both from the heat source itself or the heated calcium silicate base underneath. Unfortunately this convective fraction of the total energy input cannot be measured directly in the experiments. It is therefore estimated by calculating the radiative fraction based on the available temperature data and subtracting it from the total energy input. The conductive loss to the wooden floor is assumed negligible for this estimation, because of the low thermal conductivity of the insulating material. It is, however, considered in the heat flux analysis of the simulations, which will be discussed in Section 3.2.3.

The heat source emits thermal radiation at different wavelengths. The wavelength at the radiation peak can be estimated by Wien's displacement law, as shown here for the highest heat input:

$$\lambda_{max} = \frac{2.898 \times 10^6\,\mathrm{nm}\cdot\mathrm{K}}{578\,\mathrm{K}} = 5014\,\mathrm{nm} \tag{3.2}$$

PMMA does not transmit radiation at a wavelength of 5000 nm [106, page 5]. Therefore, the thermal radiation of the heat source is absorbed or reflected at the inner enclosure walls. For calculating the radiative heat transfer to the enclosure walls the Stefan-Boltzmann law is used, as given in Equation 3.3. The surface temperatures of the heat source can be considered homogenous, as has been shown in Figure 3.12. This is why the radiative fraction emitted from the heat source can be calculated by

$$\dot{Q}_{rad,HS} = \sigma \varepsilon_{HS} A_{HS} (T_{HS,surf}^4 - T_{encl}^4) \tag{3.3}$$

with

σ : Stefan-Boltzmann constant
ε_{HS} : emissivity of the coating of chalk spray, 0.82
A_{HS} : surface area of heat source, $0.0132\,\mathrm{m}^2$
$T_{HS,surf}$: surface temperatures of the heat source
T_{encl} : temperature of the enclosure walls

The surface temperature of the enclosure walls, T_{encl}, has not been measured in the experiments, which is why the gas temperature T_3 at $z = 290\,\mathrm{mm}$ is used as an approximation. The error introduced by this assumption is considered negligible, because the radiative heat flux is dominated by $T_{HS,surf}^4$.

As previously described, the insulating plate underneath the heat source also heats up over time. Here the radiative heat flux is more difficult to calculate, because the surface temperature is not homogenous but instead exhibits a temperature gradient from top to bottom. For the following calculation the surface temperature at the top of the insulating plate ($z = -40\,\mathrm{mm}$) is assumed to be equal to $T_{HS,surf}$. For the temperature, T_b, at the bottom ($z = -60\,\mathrm{mm}$), where the insulating plate touches the wooden floor, surface temperatures of 47 °C to 70 °C are assumed. These values are estimates based on experimental measurements of the surface temperature underneath the wooden floor. For $-60\,\mathrm{mm} < z < -40\,\mathrm{mm}$ a linear temperature profile is assumed.

$$\dot{Q}_{rad,Pro} = \int_{-60\,\mathrm{mm}}^{-40\,\mathrm{mm}} \sigma \varepsilon (T(z)^4 - T_{encl}^4) l dz \tag{3.4}$$

with

$$T(z) = T_b + \frac{z + 60\,\mathrm{mm}}{20\,\mathrm{mm}} (T_{HS,surf} - T_b) \tag{3.5}$$

and

l : length of the insulating plate
T_b : temperature at bottom of insulating plate

The results of the calculations are given in Table 3.2. It becomes apparent that radiation is the dominant mode of heat transfer, even for the lowest energy input. As described above, the convective fraction is calculated by subtracting the radiative fraction from the total energy input. For a total energy input of 29.9 W the overall convective fraction is only about 13.1 W or 44 %. As one would expect due to the Stefan-Boltzmann law, the radiative fraction increases with higher surface temperatures, see Equation 3.3. Of a total energy input of 96.0 W, only about 29 % or 27.5 W is convectively

Table 3.2: Estimates of the radiative and convective fractions of the total energy, P_{HS}, brought into the enclosure.

P_{HS} W	$\dot{Q}_{rad,HS}$ W	$\dot{Q}_{rad,Pro}$ W	$\dot{Q}_{conv}$ W
29.9	14.2 (48 %)	2.5 (8 %)	13.1 (44 %)
55.6	28.9 (52 %)	4.7 (9 %)	21.9 (39 %)
78.0	46.0 (59 %)	7.1 (9 %)	24.9 (32 %)
96.0	59.7 (62 %)	8.8 (9 %)	27.5 (29 %)

transferred to the surrounding air. It should be noted, however, that these values are estimates only.

Analysis of velocity measurements

Typical instantaneous velocity fields for each heat input are shown in Figure 3.18. As was described before, the entire plume is recorded in three steps. That is why the plume regions $z < 260\,\mathrm{mm}$, $260\,\mathrm{mm} < z < 460\,\mathrm{mm}$ and $460\,\mathrm{mm} < z$ are recorded at three different points in time. While the plume on the left at the lowest heat output of 30 W is clearly laminar, the plume on the right at the highest heat output of 96 W is largely turbulent. With increasing energy input the transition from laminar to turbulent flow occurs at lower heights.

For the following analysis mostly time-averaged velocity fields are used, which are presented in Figure 3.19. It should be noted, that the scaling of the color bar was changed compared the instantaneous velocity fields, in order to improve the clarity of the figure. Due to the turbulent nature of the higher-energy plumes, the plume width at the top increases. Interestingly, the maximum velocity seems to occur at the plume with the second lowest energy input. However, one should keep in mind that these images are time-averaged and therefore transient velocity maxima, which are characteristic for turbulent flows, are not visible here.

In DaVis [107] an uncertainty quantification method is implemented based on a statistical analysis of the correlation between the images to be matched. This is called the correlation statistics method and is an extension of the particle disparity method by Sciacchitano et al. [87]. Unlike the particle disparity method, it works on the pixel level by evaluating the contribution of individual pixels to the correlation peak. For a detailed description of the method see [108]. The relative measurement uncertainty belonging

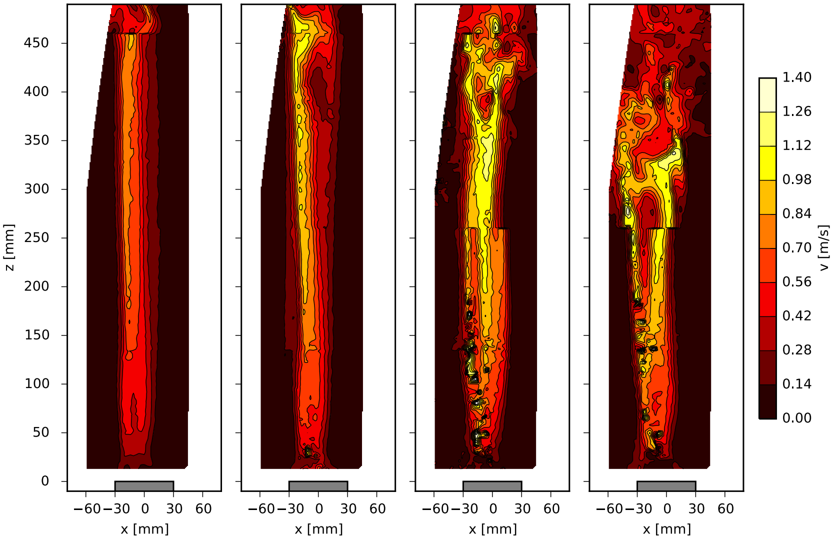

Figure 3.18: Instantaneous velocity fields for 30 W, 56 W, 78 W and 96 W. Each figure comprises measurements taken at three different points in time.

to Figure 3.19 is presented in Figure 3.20. It is calculated by dividing the absolute measurement uncertainty by the absolute flow velocity for every interrogation window. That is why in regions with low flow velocities (outside the plume) the relative measurement uncertainty is high, although the absolute error is small. For the greater part of the measurement region, where the plume is located, the measurement uncertainty is below 4 %. However, there are small regions close to the heat source with higher uncertainties, which may be caused by reflections and/or low particle densities. Inside the plume at heights where the velocity profiles are derived, the uncertainty does not exceed values of 4 % and is usually below 2 %. For some of the other experimental runs that are not displayed here the uncertainties are higher, up to 8 % at the heights of the velocity profiles.

In order to allow for a better comparison of different experimental runs the velocity profiles of all experiments are presented in Figure 3.21. Velocity profiles for different heat inputs are evaluated in three positions. The heights of 100 mm and 250 mm are recorded at the same time, while recordings in 400 mm height have a time shift of around 120 s to 180 s, due to the shifting of the cameras.

The least scattering can be observed for power settings of 78 W and 96 W.

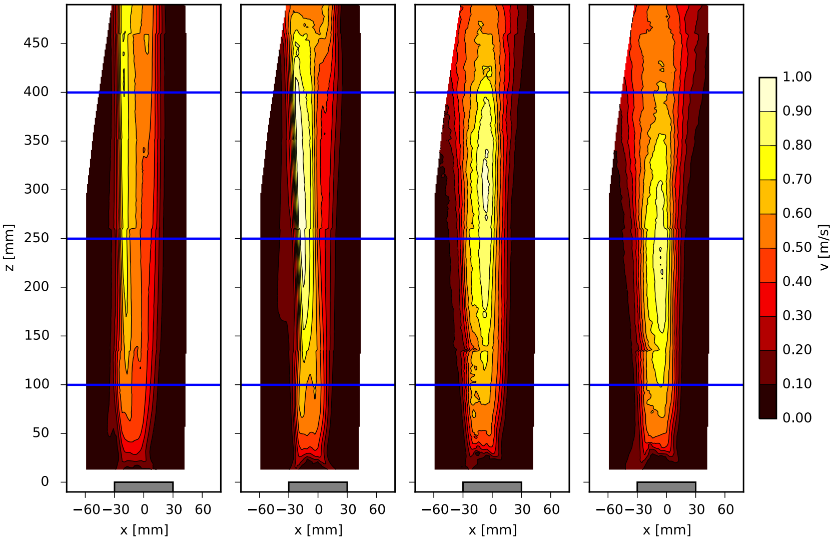

Figure 3.19: From left to right velocity fields at 30 W, 56 W, 78 W and 96 W are shown. They are recorded with 1 Hz and time-averaged over 117 s (30 W) and 180 s (others). The blue lines indicate the positions where the velocity profiles are derived. The color bar was changed compared to Figure 3.18.

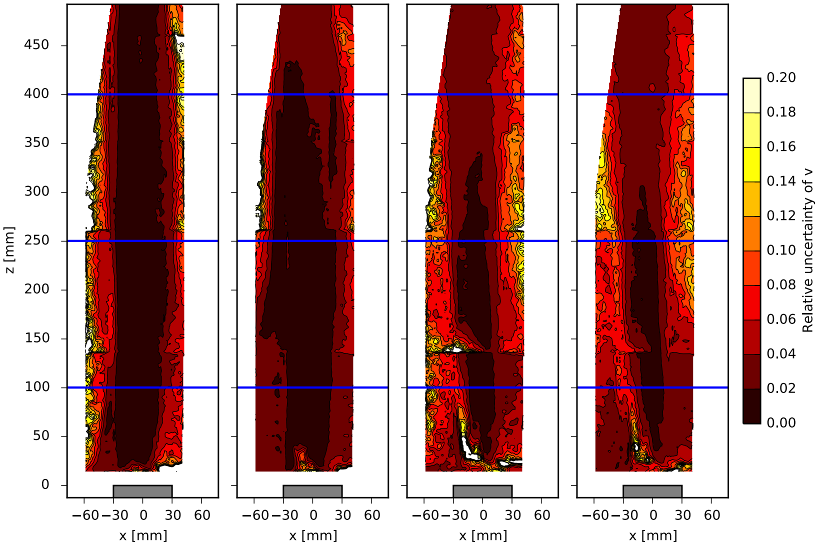

Figure 3.20: Relative measurement uncertainty belonging to Figure 3.19.

This is in accordance with the least scattering of the ambient conditions, compare Figures 3.15 and 3.16. The flattening and widening of the velocity profiles at the top of turbulent plumes – already observed in Figure 3.19 – is visible throughout all experimental runs at 78 W and 96 W. In virtually all experiments the plume deviates to the left, bearing in mind that the coordinate origin is placed at the center of the heat source top surface. As already discussed in Section 3.1.4, this behavior is not likely to be caused by non-homogeneous heating of the copper block but might be caused by an asymmetric cable routing to the heating coil or other external factors. Further investigations are therefore necessary.

In some of the runs at 30 W and 56 W, the velocity profiles exhibit two peaks. They are not an artifact of the time-averaging of the images, because they also appear on the instantaneous velocity fields. Whether this observation indicates a double or a hollow plume cannot be distinguished from the available data, because it is recorded on a vertical plane parallel to the flow. A possible explanation could be, that the surrounding air undergoes a stronger acceleration on the vertical sides of the heat source than on the top of the heat source and in this way a hollow plume is created. The fact, that such a double or hollow structure is only occasionally observed, might be caused by the size of the heat source. For a very small heat source a stable hollow structure might not be able to propagate into the plume, for a large heat source this could be more likely to happen. Therefore, if the size of the heat source applied in the experiments is in-between, a hollow structure might only occasionally occur. This, however, is only a speculation, further investigations, based on experiments or simulations, are required in order to investigate the underlying cause for this behavior.

In order to be able to compare the velocity measurements of different power settings quantitatively, characteristic values are derived from the velocity profiles, such as maximum velocity, plume width and area integral of the velocity profile. These characteristic values are displayed in Figures 3.22a, 3.22b and 3.22c. Each figure consists of three subplots that illustrate the relation of the characteristic value and the heat input at a specific height.

Figure 3.22a displays the maximum flow velocities at three heights. The maximum velocities close to the heat source (100 mm height) are positively correlated with the heat input. However, the velocity increase with raised heat input is not as strong as one might expect. At the intermediate (250 mm) and top (400 mm) position an increased heat input of more than 60 W leads to constant or even decreasing maximum velocities. This is caused by the transition from laminar to turbulent flow. As mentioned above, the averaging of the velocity fields makes the transient velocity maxima of turbulent flows disappear.

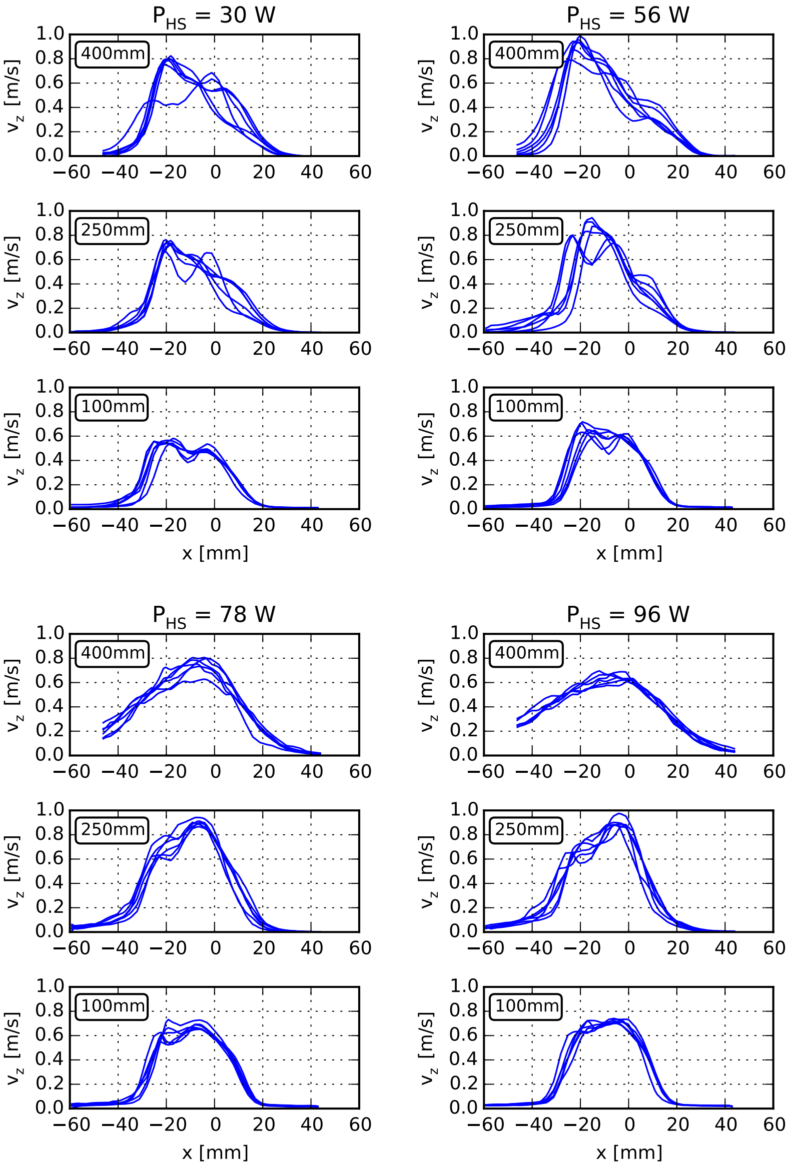

Figure 3.21: Scattering of v_z velocity profiles of all experiments. The subfigures show different power settings, for each of which three different heights are investigated. Every run is time-averaged over the entire recording time.

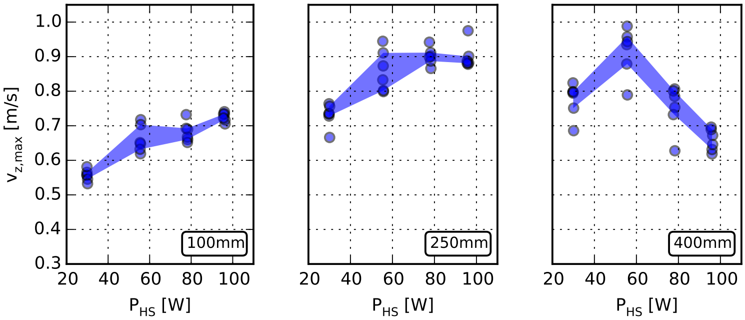

(a) Maximum velocities

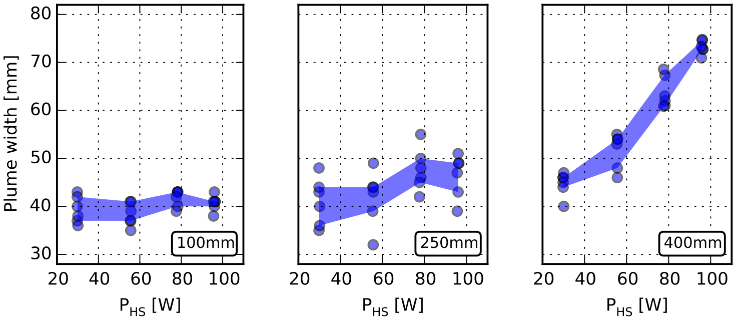

(b) Plume widths (determined via a velocity threshold of 0.2 m/s)

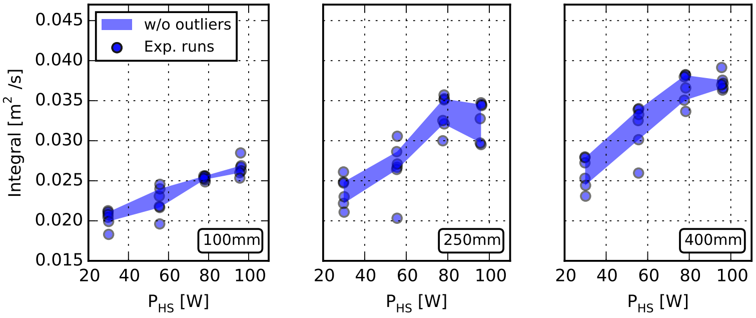

(c) Flow integrals

Figure 3.22: Characteristic flow values in different heights. The blue area shows the range of results without the extreme values at each power setting.

In order to determine the plume width, a velocity of 0.2 m/s is defined as the plume boundary. For some of the velocity profiles in 400 mm height at 78 W and 96 W the measurement area and thus also the velocity profiles do not cover the entire width of the plume, see Figure 3.21. Here the left plume boundary needs to be estimated. This is done by assuming a zero velocity at $x = -60\,\mathrm{mm}$ and approximating the values to the left edge of the velocity profile by a straight line. In Figure 3.22b the resulting plume widths are displayed. While they are independent of the heat input at the close range of the heat source, they show a strong positive correlation at the top position. This is again caused by the transition to a turbulent flow, as already seen in Figure 3.19.

Another meaningful characteristic of the plume – the induced volume flow – cannot be calculated, because only two-dimensional data is available and the plume is apparently not rotationally symmetric. Therefore, as an indication of the volume flow, the integrals of the velocity profiles are calculated. Again, a few velocity profiles at the top position at high heat output require a completion of the velocity profile. This is performed according to the description above. The resulting integrals are displayed in Figure 3.22c and generally show a positive correlation with the heat output. However, increasing the heat output further than 80 W does not increase the volume flow. Generally the flow integrals and the volume flow respectively grow with increasing distance to the heat source. This occurs because of the entrainment of ambient air into the plume.

As can be seen from the previous results, the transition from laminar to turbulent flow is of fundamental importance for the plume characteristics. With increased heat input this transition occurs at lower heights closer to the heat source. Where precisely this transition occurs is not yet known, because the plume has been evaluated in discrete heights only. Therefore in order to further localize the point of transition, the plume is now evaluated along its centerline in the flow direction. However, as can be seen from Figure 3.21, the centerlines are not straightforward to determine, because most of the plumes have shifted to the left and have asymmetrical flow profiles.

The identification of the centerline used for the experiments in this work is based on symmetry consideration of the vertical velocity. Basically, it is assumed that the centerline's x position represents the most symmetrical point – with respect to v_z – at a given height z. Therefore the x position of the centerline, x_{cl}, is given by

$$x_{cl} = \left\{ x \mid \min \left(\int_{\Omega(x)} v_z(x+\chi, z) - v_z(x-\chi, z)\; d\chi \right) \right\} \,.$$

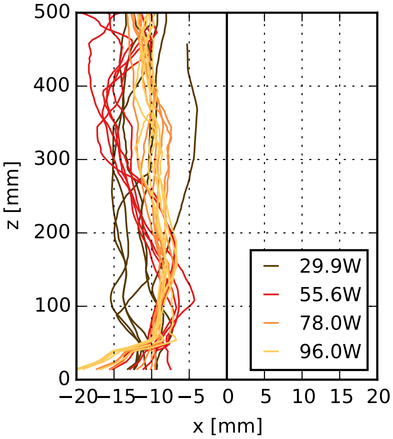

Figure 3.23: Centerline positions for all experimental runs. For illustration purposes the axes are not in the same scale.

Here, the domain $\Omega(x)$ indicates a region around the evaluated x position. This definition has proved to produce more reasonable centerlines for the experimental data presented than other methods, such as the maximal value of v_z or the zero-crossing of v_x. All these methods would indicate the same centerline in an ideal plume. The resulting centerline positions for all experimental runs are presented in Figure 3.23.

In Figure 3.24a the vertical velocity, v_z, along the centerline for all experimental runs is presented. In the nearfield of the heat source the flow is accelerated due to the buoyancy of the warm air. This acceleration is stronger the higher the heat input is. At a height of 250 mm above the heat source top surface, the experiments with 29.9 W total energy input reach a velocity of 0.6 m/s to 0.7 m/s while the experiments with $P_{HS} = 96.0\,\mathrm{W}$ reach a velocity of 0.8 m/s to 0.9 m/s.

An indication of the transition from laminar to turbulent flow is a decline in vertical velocity. A turbulent flow leads to the formation of eddies, which divert parts of the upwards-directed motion into the horizontal directions. As a result, v_z decreases and the horizontal velocity components v_x and v_y increase. For the experiments with 55.6 W to 96.0 W the transition is clearly visible. The height at which this transition occurs is lower when the heat input is higher. For the experiments with $P_{HS} = 96.0\,\mathrm{W}$ the turbulent flow begins at around 200 mm to 300 mm, while for the experiments with

$P_{HS} = 55.6\,\mathrm{W}$ this occurs at around 300 mm to 400 mm. For the experiments with the lowest heat input the decline in v_z is only visible for some of the experimental runs; for the other runs it would have occurred at a greater height and could not be observed due to the limitations of the experimental setup.

In order to make the results more generally comparable to other experimental findings, they need to be rendered dimensionless. This is achieved by normalizing the velocity, v_z, of a run from 0 to 1, so that 0 is the minimum velocity and 1 is the maximum velocity measured in that run for $z > 200\,\mathrm{mm}$. A threshold of 200 mm is introduced in order to avoid disturbances in the near field of the heat source, which can occur for other velocity components. The resulting normalized vertical velocity is referred to as $\overline{v_z}$.

Additionally, $\overline{v_z}$ is not plotted as a function of z but as a function of the Grashof number. The Grashof number is a dimensionless number that represents the ratio of buoyancy forces to viscous forces. It can therefore give an indication of whether a flow is laminar or turbulent. For the experiments described here the local Grashof number is determined as follows:

$$Gr = \frac{g\beta(T_{surf} - T_1)z^3}{\nu^2} \tag{3.6}$$

with

g : acceleration due to gravity
β : coefficient of thermal expansion
T_{surf} : surface temperature of heat source
T_1 : air temperature at z = 50 mm
ν : kinematic viscosity

In Figure 3.24b the dimensionless velocity, $\overline{v_z}$, as a function of Gr is shown. Due to the normalization the centerline velocities are no longer clustered according to the heat input. Instead of this the dimensionless centerline velocities of all heat inputs lie on top of each other. All curves reach their maximum in the range $2 \times 10^8 < Gr < 2 \times 10^9$. This result is in accordance with the previous findings of Noto et al. [109], who investigated the turbulent transition of a thermal plume above a line heat source and reported the same limits for the transition from laminar to turbulent flow.

The standard deviation of the horizontal velocity is another appropriate measure of turbulence for the present setup, because a laminar buoyancy-driven flow will produce very little horizontal movement, whereas the passing eddies of a turbulent flow produce strong fluctuations in the horizontal velocity. For the experiments described here the standard deviation of the v_x velocity along the centerline is shown in Figure 3.25a. There are two effects

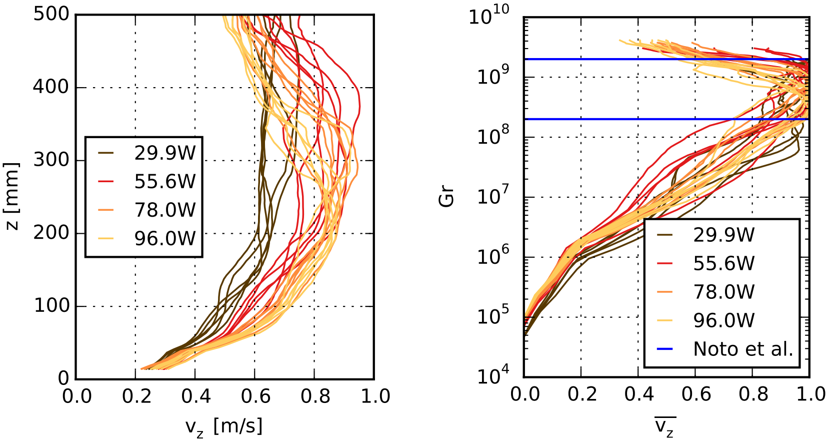

(a) $v_z(z)$ (b) $\overline{v_z}(Gr)$

Figure 3.24: Vertical velocity and normalized vertical velocity in the centerline of the plumes.

for $z < 180\,\mathrm{mm}$, which might obscure the message of this figure. Firstly, close to the heat source for $z < 100\,\mathrm{mm}$ the flow has a non-negligible horizontal component, because it is flowing around the heat source itself. Secondly, at a height of $110\,\mathrm{mm} < z < 180\,\mathrm{mm}$, laser light reflections caused inaccurate measurements for some runs with 78 W and 96 W. This is why the two peaks for $z < 180\,\mathrm{mm}$ are not considered to be an indication of a turbulent flow. What is however an indication of a turbulent flow is the increased standard deviation of v_x in a height of $z > 270\,\mathrm{mm}$. In line with the previous observation, increasing the heat input leads to a lower point of transition. For $P_{HS} = 29.9\,\mathrm{W}$ the increased fluctuations of v_x are only just visible.

In Figure 3.25b the normalized standard deviation of v_x velocity is shown as a function of the Grashof number. Only the transitional region is shown in order to make individual runs visible. In an analogy to the previous normalization, $\sigma(v_x)$ is normalized by assigning 0 to the minimum standard deviation and 1 to the maximum standard deviation of every run for $z > 200\,\mathrm{mm}$. The resulting normalized standard deviation is referred to as $\overline{\sigma(v_x)}$.

The Grashof number is calculated in accordance with Equation 3.6. Again, it becomes apparent that the transitional region determined in the present study lies within the limits determined by Noto et al. [109]. Furthermore, the present study allows localization of the transitional region

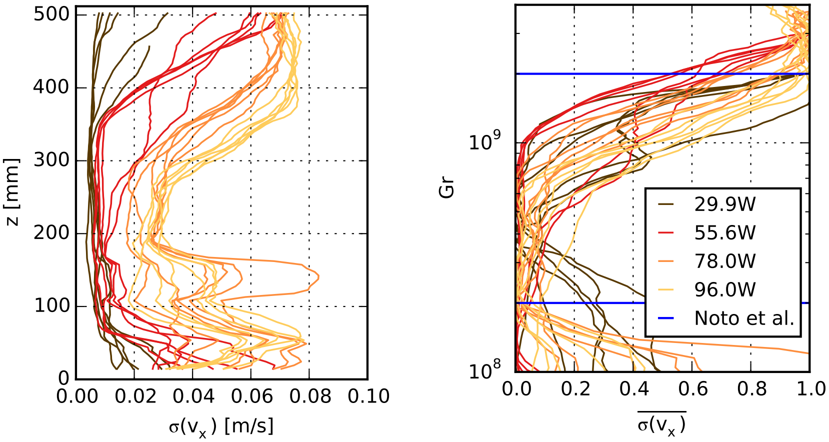

(a) $\sigma(v_x)$ as a function of z for the entire plume height.

(b) $\overline{\sigma(v_x)}$, as a function of Gr. Enlargement of the transitional region.

Figure 3.25: Standard deviation and normalized standard deviation of v_x in the centerline of the plumes.

more precisely. The increase in fluctuations of the normalized v_x velocity and thus the transition from laminar to turbulent flow occurs in the range $4 \times 10^8 < Gr < 2 \times 10^9$.

In this section a number of characteristic values could be derived, which have been used for a comparison among the experiments and will also be used for comparisons with the simulations. Although possible improvements for further experiments have been identified, the experiments discussed provide a sound basis for the validation study, which will be presented at the end of this chapter. First, however, the setup of the simulations will be explained in the following section.

3.2 Simulations with FDS

The experiments described in the previous section are intended to be used for the validation of CFD models. Here, FDS 6.2.0 is applied for the simulations. In the following section the simulation setup and the processing of the results for the open plume experiments will be presented.

3.2.1 Simulation setup

In general the implementation of the experiments in this thesis into FDS simulations is rather straightforward. This is not least due to the fact that the experiments have been specifically designed for this purpose. The geometry is built on a Cartesian grid, the boundary conditions are well defined, and neither pyrolysis nor combustion need to be considered. However, a few aspects do require closer examination, such as the heat source boundary condition, an adequate grid resolution, or the required time to reach quasi-steady state.

Building the model

The simulation domain includes the entire enclosure plus a few centimeters of ambient air in every dimension. Limiting the domain to the plume region only would have allowed a better plume resolution. However, it would not have been possible to consider the temperature stratification of the surrounding air, nor the radiative feedback from the inner enclosure walls. Extending the simulation domain further than a few centimeters outside the enclosure is not expected to have a significant effect on the simulation results but would result in a huge increase in computational cost.

The gas temperature of the ambient air outside the enclosure is prescribed according to the experimental measurements. In combination with a definition of the external mesh boundaries as 'open', the convective cooling effect on the outer enclosure walls is taken into account. The enclosure itself, i.e. the wooden floor and the PMMA sides and top, is modeled with realistic material parameters to allow heat transition. This is important because in order to attain steady state the heat flux balance of incoming and outgoing energy in the enclosure needs to be leveled. Two holes in the wooden floor, which serve as particle inlet and outlet respectively in the experiments, act as a pressure relief in the simulations.

Since the heat released by the heat source is the driver for the observed flow, the heat source boundary condition is of great importance. During preliminary simulations the surface temperature has been prescribed according to experimental measurements. However, this is not optimal, because as was shown in Figure 3.12, the surface temperature of the heat source is not necessarily identical with the embedded thermocouple reading. In addition, one cannot ensure that the overall energy transferred into the enclosure is the same as during the experiments. This is why a different approach has been chosen for the actual simulations. Instead of the surface temperature, the net heat flux on the heat source surface is prescribed. By doing this it is guaranteed that the intended amount of energy is transferred into the enclosure. The radiative and convective fraction is calculated by FDS, based on the actual flow conditions and the radiation exchange with the surroundings. For the latter, the heat source's emissivity needs to be fed into FDS, which has been determined as 0.82 in the experiments.

Considering heat conduction losses

Despite its low thermal conductivity, the calcium silicate base and subsequently the wooden floor underneath have heated up in the course of each experimental day. Due to the limited capabilities of FDS with regard to heat conduction, an iterative approach needs to be used in order to obtain a reasonable estimate for this effect. The aim is that the sum of the heat conducted through the wooden floor, the heat emitted from the insulating base and the heat emitted from the heat source equals the total electric power measured in the experiments in order to obtain a heat input as close as possible to that of the experiments.

First, the heat transfer to the bottom of the wooden floor is calculated. Therefore a strongly simplified FDS simulation is set up that resembles the insulating base of calcium silicate and the wooden floor. A surface temperature according to the experiments is maintained on the upper side and the conductive heat flux to the bottom is recorded after steady state is attained. It should be noted here that FDS is only capable of simulating one-directional heat conduction. Thus a lateral heat conduction through the wooden floor cannot be considered. However, since the simulation is being performed for an estimate of the heat loss only, this simplification is acceptable. Two simulations for heat source temperatures of $T_{HS} = 150\,°\mathrm{C}$ and $T_{HS} = 310\,°\mathrm{C}$ are performed, and intermediate values are linearly interpolated. The heat loss via conduction through the wooden floor is:

- 1.3 W for $T_{HS} = 150\,°\mathrm{C}$ ($P_{HS} = 29.9\,\mathrm{W}$)
- 3.0 W for $T_{HS} = 310\,°\mathrm{C}$ ($P_{HS} = 96.0\,\mathrm{W}$)

As a second step, the temperature profile that developed inside the calcium silicate base is prescribed as a surface temperature on its outer sides and another simulation is run. During this simulation the net heat emitted from the calcium silicate base is measured. This heat flux together with the heat conducted to the wooden floor is subtracted from the total electric power in all subsequent simulations in order to obtain the net heat flux, which is prescribed as a boundary condition for the heat source.

Output values

For a reasonable comparison with the experiments, the same output quantities at a similar temporal and spatial resolution should be recorded in the simulations. Additionally, further quantities are investigated for diagnostic purposes.

- Vector slicefiles in various positions orthogonal to the y and z axis record velocity, temperature, pressure, and turbulence resolution.
- The upwards-directed volume and heat flows in 200 mm and 300 mm height above the heat source are measured.
- Gas temperatures and thermocouple readings in the same positions as in the experiments are recorded.
- The net, radiative and convective heat flux on the surface of the heat source and the insulating base of calcium silicate is captured.
- Boundary files for the wall temperatures as well as the net, radiative and convective heat flux to the enclosure are recorded.
- Temperature profiles within the enclosure are also captured.

Meshing and grid sensitivity

The applied mesh distribution is illustrated in Figure 3.26. It consists of seven vertical meshes covering the main part of the simulation domain and an eighth mesh spanning the entire top of the domain where the ceiling jet occurs. The distribution of meshes is based on the following criteria.

- As recommended in the FDS user's guide [14], the region of interest is not cut by mesh boundaries. The heat source as well as the main part of the plume are completely enclosed in the central mesh.
- The number of meshes takes JURECA's architecture into account, which has 24 cores per node. Therefore each mesh is computed on three cores.
- The meshes are roughly similar in size to allow for an even load-balancing when simulating with a synchronized time-step.
- The dimensions of the meshes are each in the form $2^l \times 3^m \times 5^n$, where l, m and n are integers. This is beneficial for a fast computation via FDS' Poisson solver based on Fast Fourier Transforms [14].

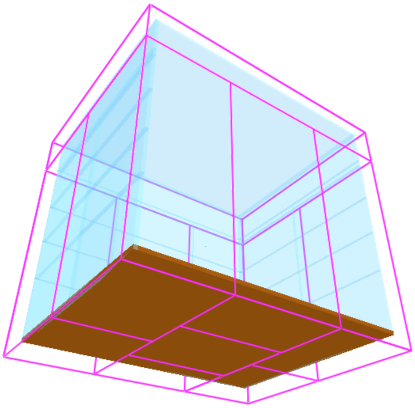

Figure 3.26: Mesh distribution for open plume simulations.

A question that needs answering prior to every FDS simulation is this: what mesh resolution is appropriate for the given setup? In FDS it is not possible to refine parts of a mesh locally or change the mesh resolution dynamically over time. Instead, the entire mesh usually has the same resolution. On the one hand, the resolution needs to be sufficiently fine, allowing the flow and important geometrical details to be resolved with an adequate number of cells. On the other hand, the computational effort increases dramatically when refining the grid. When halving the edge length of the cells in each dimension the total number of cells increases by a factor of eight. Additionally, the time-step halves in order to fulfill the CFL condition. As a consequence, a simulation with half the edge length of the cells will take approximately 16 times longer to compute.

The recommended approach for determining an adequate mesh resolution is to start simulations on a relatively coarse mesh and gradually refine the mesh until the results converge to a solution [14]. The simulation results should not be influenced by the cell size. This recommendation has been followed for the open plume simulation setup, and the results are shown in Figure 3.27. An overview of the investigated resolutions and the resulting cell sizes is given in Section 3.2.2.

Figure 3.27a shows the heat flux, which is convectively emitted from the sides and the top of the heat source. It is apparent that the grid resolution has an impact here. Compared to the heat flux at 10 mm resolution, the simulation with 1.25 mm cell size transfers approximately 25 % less heat convectively. This means that the radiative fraction increases with higher

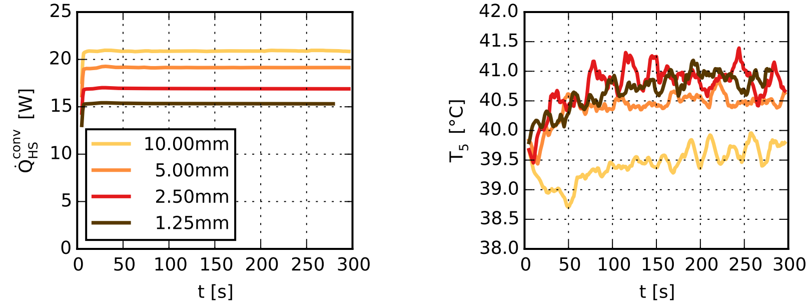

(a) Convective heat flux emitted from the heat source.

(b) Gas temperatures recorded at position T_5.

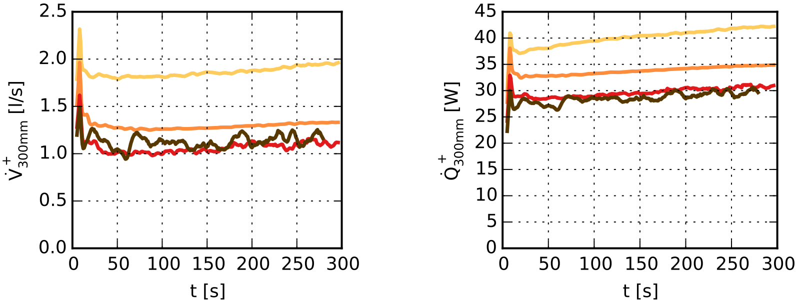

(c) Upwards directed volume flow in a height of 300 mm.

(d) Upwards directed heat flow in a height of 300 mm.

Figure 3.27: Grid sensitivity study for open plume simulations with $P_{HS} = 96\,\mathrm{W}$. Important simulation results are compared for grid resolutions of 10 mm, 5 mm, 2.5 mm and 1.25 mm. For the latter two, the outer meshes, which do not contain the plume, are set up with half the specified resolution. The simulation with 1.25 mm resolution took too long to reach t_{end}, but achieved steady state. All data is smoothed with a moving average over 10 s.

Table 3.3: D^* and $D^*/\delta x$ for various grid resolutions and heat inputs.

P_{HS}		29.9 W	55.6 W	78.0 W	96.0 W
D^*		15 mm	19 mm	22 mm	24 mm
$D^*/\delta x$	10.00 mm res.	1.5	1.9	2.2	2.4
	5.00 mm res.	3.0	3.8	4.4	4.8
	2.50 mm res.	6.0	7.6	8.8	9.5
	1.25 mm res.				19.0

resolution, because the net heat flux – being the sum of radiative and convective heat flux – is explicitly defined. It should be noted here again that the thermal plume, which is in the focus of this investigation, is only driven by the convective heat flux emitted from the heat source and the insulating base. When comparing properties such as flow velocities in the plume for different grid resolutions it should therefore be taken into account that in high-resolution simulations less energy is driving the plume.

For the gas temperatures in the enclosure the temperature at position T_5 is shown as an example, see Figure 3.27b. The temperature increases with increasing grid resolution until it converges at a resolution of 2.5 mm. A further refinement to 1.25 mm does not change the temperature significantly. Although not all of the figures at position T_1 to T_4 exhibit such a clear convergence, a grid resolution of 2.5 mm is considered appropriate for this setup.

Figures 3.27c and 3.27d show volume and heat flow 300 mm above the top of the heat source. Again, a grid resolution of 2.5 mm seems to be fine enough for resolution-independent results. Interestingly, this also applies for the heat flow, although the convective heat transfer at the heat source itself is not grid independent, as was shown in Figure 3.27a. There are apparently other effects that counteract the decreasing convective heat transfer of the heat source to some extend.

As was explained in Section 2.1.2 the dimensionless expression $D^*/\delta x$ can be used as a measure of how well a buoyant plume is resolved by the mesh. D^* is the characteristic fire diameter, which has been defined in Equation 2.1 and δx is the nominal size of a mesh cell. In Table 3.3 the values for all grid resolutions and heat inputs are provided. For comparison, a table of reference values from a multitude of simulations can be used, which is provided in the FDS validation guide [15]. Although these reference values for $D^*/\delta x$ cover a wide range, it can be said, that for the present setup a resolution of 2.5 mm seems to be a reasonable choice, while a resolution of 5.0 mm is rather coarse.

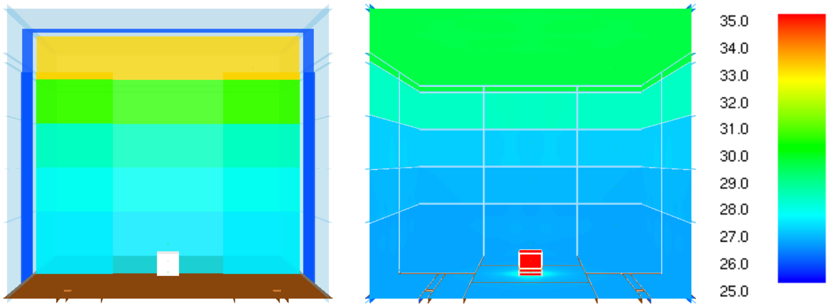

(a) Gas temperatures (b) Inner wall temperatures

Figure 3.28: Prescribed initial temperatures for open plume simulations at $t_{sim} = 0\,\mathrm{s}$. The setup with $P_{HS} = 55.6\,\mathrm{W}$ is shown, values are given in °C.

It has to be noted, however, that the values D^* and $D^*/\delta x$ are usually applied to plumes of real fires. For that reason they are based on the assumption, that with decreasing heat input the (characteristic) diameter of the fire decreases, too. In the setup described here, the dimensions of the heat source do not change with changing heat input. Also, the flow conditions in the nearfield and the radiative and convective fraction differ between a real fire and an electrical heated block of copper. Therefore, the values provided in Table 3.3 should be considered approximate values for orientation only.

Required simulation time

Considering the computational effort of FDS simulations with a fine resolution, it becomes obvious that one does not want to run the simulations longer than necessary. However, the experiments have been carried out in quasi-steady state and similar conditions need to be guaranteed in the simulations. The heat-up time of the experiments of approximately 1.5 hours cannot be computed in the simulations. This is why measures are taken to reduce the heat-up time of the simulations to a minimum.

The initial gas temperatures inside the enclosure are prescribed according to the temperature stratification measured in the experiments. A slicefile of the defined gas temperatures is shown in Figure 3.28a. The sharp transitions between temperature layers dissipate after a few seconds, but the overall layering remains, thus reducing the required time to steady state

Similar to the gas temperatures, the initial temperatures of the enclosure walls and ceiling have also been prescribed. The enclosure temperatures at $t_{sim} = 0\,\mathrm{s}$ are displayed in Figure 3.28b. In this case no experimental

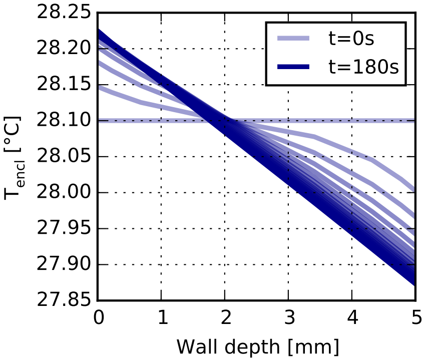

Figure 3.29: Chronological sequence of temperature profiles inside the enclosure wall at $z = 410\,\mathrm{mm}$ and $P_{HS} = 55.6\,\mathrm{W}$. Starting at t = 0 s a temperature profile is plotted every 10 s. A depth of 0 mm denotes the inner wall surface.

measurements are available. However, the average enclosure temperature can be approximated by the mean of the inner and outer gas temperature at every location. A temperature gradient inside the PMMA slab is not prescribed, but evolves automatically within the first few minutes, as can be seen in Figure 3.29. At $t_{sim} = 0\,\mathrm{s}$ the entire profile of the wall has a uniform temperature of 28.1 °C. After approximately 60 s the inner wall surface has heated up due to the higher gas temperatures on the inside and the outer wall surface has cooled down due to the lower ambient temperatures. Therefore a realistic temperature profile is obtained at steady state.

Figures 3.27 and 3.29 already indicate that a heat-up time of three minutes may be sufficient for the simulations. However, in order to underpin this observation the heat balances of incoming and outgoing heat fluxes into the gas phase are also calculated. In Figure 3.30 the energy difference brought into the gas phase by the heat source and heat loss at the inner enclosure surface is shown. After approximately 180 s the net heat flux approaches zero and – with regard to the heat fluxes – quasi-steady state can be assumed. This is why the following simulations are evaluated after a heat-up time of three minutes.

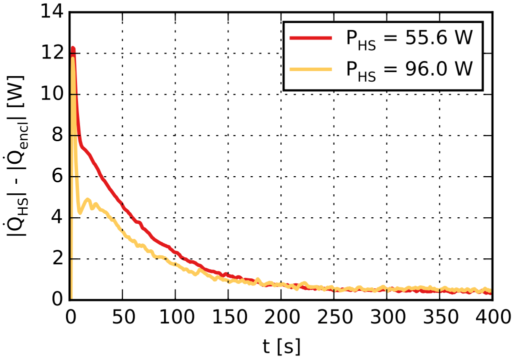

Figure 3.30: Heat balances of incoming and outgoing heat fluxes, measured at the heat source surface and the inner enclosure surface respectively.

3.2.2 Execution and output processing

As was shown in the previous sections, the ambient temperatures as well as the heat input are sufficiently similar between repeated experiments of the same power setting to allow for a common comparison with one simulation only. Thus in total four simulations with heat inputs of 29.9 W, 55.6 W, 78.0 W and 96.0 W are required.

Here again it is advisable to exploit the benefits of FDSgeogen. Instead of setting up one FDS input file for each of the four simulations, it is sufficient to set up and maintain one FDSgeogen input file for all simulations. This helps to avoid unnecessary work and sources of error, especially when several iterations are necessary before a final simulation setup is reached. Input values that vary between the simulations, such as electrical power or ambient temperatures, can be read in automatically from an external file.

The simulations have been run on JSC's general purpose supercomputer JURECA, which features a peak floating point performance of roughly 1.8 petaflops. However, due to the poor scalability of FDS for this setup and problem size, the simulations are run on individuals of the 1,800 compute nodes only. Each of these nodes consists of two Intel Haswell E5-2680 v3 12 core CPUs [110]. The compute times given in Table 3.4 originate from the simulations of Figure 3.27.

In order to extract the flow velocities from the simulations for further processing *fds2ascii.f90* is used. This Fortran 90 program is provided with FDS [14, page 275] and allows for the extraction of simulation data stored

Table 3.4: Compute times for the simulations with $P_{HS} = 96\,\mathrm{W}$ and $t_{end} = 300\,\mathrm{s}$.

Resolution plume region	Resolution surrounding	Number of cells	Number of cores	Compute time
10.00 mm	10.00 mm	0.37×10^6	24	2.4 hours
5.00 mm	5.00 mm	2.95×10^6	24	1.4 days
2.50 mm	5.00 mm	3.81×10^6	24	6.5 days
1.25 mm	2.50 mm	30.47×10^6	24	134.0 days

as slice files, and for the export of them as generic file types, for example as comma separated values. Thus, the simulation results can be processed similarly to the experimental data.

3.2.3 General observations

As was described in Section 3.1.4, in some of the experiments at higher power settings areas with a low particle concentration are visible. These areas extend from the top surface of the heat source upwards into the plume. It was assumed that particles in these regions are evaporated by high gas temperatures. However, close to the heat source there have been no temperature measurements available to verify this assumption. The simulation results can now be used for a closer examination. Even if they are not be in total agreement with the experiments, they can serve as a useful point of reference. In Figure 3.31 both the flow velocities and gas temperatures at a close range to the heat source are shown.

Figure 3.31a clearly shows an area on top of the heat source with reduced flow velocities. Here, in the slipstream of the heat source, the surrounding air has contact with the heat source for an extended period of time and thus heats up more. The effect can be seen in Figure 3.31b. While the gas temperatures at the side of the heat source do not exceed 120 °C, they are at around 210 °C at the top of the heat source. This is close to the boiling temperature of DEHS, which is around 232 °C to 249 °C at 1 bar [76], and thus can explain the reduced particle concentration. For experiments with higher heat source temperatures it would be advisable to use particles with a higher temperature resistance.

As mentioned above, there are no experimental temperature measurements available inside or close to the plume. It would be worthwhile therefore to evaluate the temperature distribution in these areas on the basis of

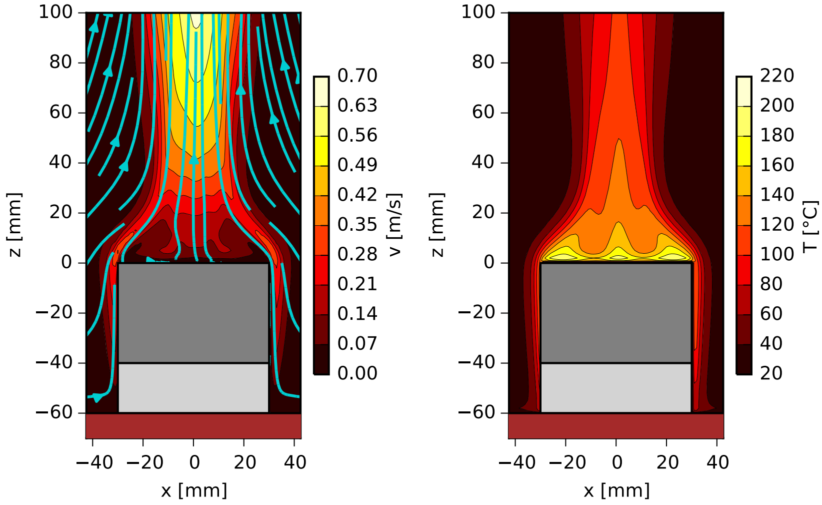

(a) Flow velocities

(b) Gas temperatures

Figure 3.31: Time-averaged flow velocities and gas temperatures close to the heat source for the simulation with 1.25 mm resolution and $P_{HS} = 96.0\,\mathrm{W}$.

the FDS simulations. Figure 3.32 shows the gas temperatures for simulations with different grid resolutions at $P_{HS} = 96\,\mathrm{W}$. Generally, the temperatures drop with increasing distance from the heat source. Close to the ceiling, the temperatures do not exceed 65 °C. With increasing grid resolution the hot region directly above of the heat source extends further into the plume. For example, the 95 °C isotherm extends to a height of 30 mm at the coarsest resolution versus a height of 150 mm at the finest resolution. Outside the plume the height of the colder lower layer increases with a finer grid resolution, with the exception of the two finest resolutions, which are very similar in this regard.

During the experiments the total energy brought into the system was measured. The individual fractions transferred via convection, radiation or conduction, however, could not be measured directly. That is why the convective heat transfer in the experiments was estimated in Section 3.1.4. In the simulations the proportionate heat fluxes can be recorded directly, the results are shown in Figure 3.33.

It becomes apparent that radiation is the dominant mode of heat transfer, even for the lowest energy input. For a total energy input of 29.9 W the total convective fraction – both transferred from the heat source and the calcium

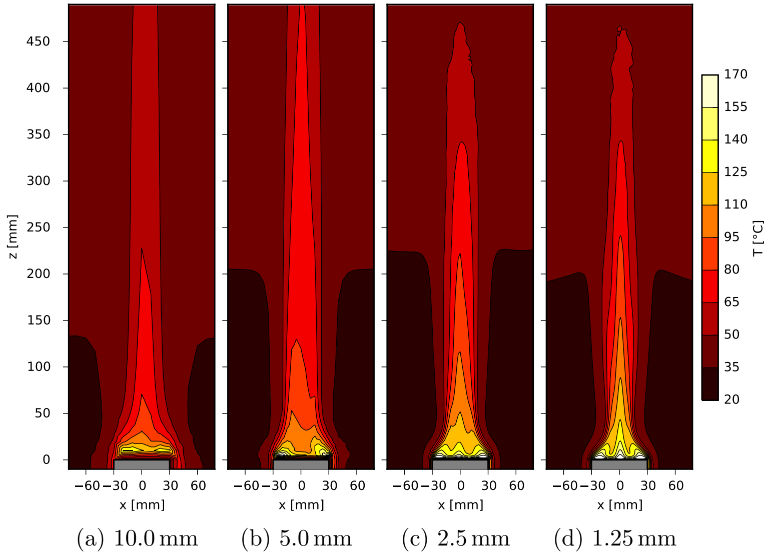

(a) 10.0 mm (b) 5.0 mm (c) 2.5 mm (d) 1.25 mm

Figure 3.32: Time-averaged temperature fields for open plume simulations with $P_{HS} = 96\,\mathrm{W}$.

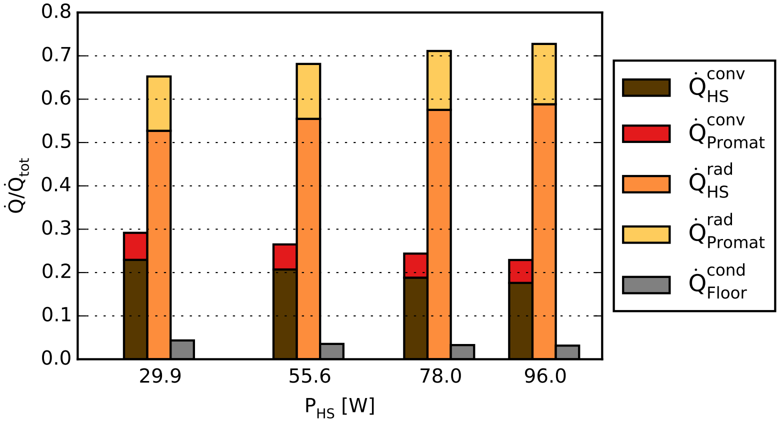

Figure 3.33: Convective, radiative and conductive fractions of the total heat input, P_{HS}, for simulations with 2.5 mm grid resolution at steady state.

silicate base – is only about 29 % or 8.7 W. As one would expect due to the Stefan-Boltzmann law, the radiative fraction increases with higher surface temperatures, see Equation 3.3. Of a total energy input of 96 W, only about 23 % or 22.0 W is convectively transferred to the surrounding air.

This effect is not advantageous for a two reasons. First, most of the energy brought into the system is not used to drive the thermal plume. Instead it is radiated from the heat source surface to the inner enclosure walls. As was shown in Section 3.1.4 PMMA does not transmit thermal radiation at the respective wavelength. Thus, the inner enclosure walls warm up, which subsequently leads to an overall increase of the gas temperature inside the enclosure. Second, uncertainties in the measurement of the heat source's emissivity during the experiments will have a direct impact on the radiative fraction resulting from the simulations, because the radiative heat flux is directly proportional to the emissivity. This results from the Stefan-Boltzmann law, which is shown in Equation 3.3.

For the reasons described above, it might be useful to modify the heat source for future experiments. In order to reduce the radiative heat transfer as far as possible a low emissivity would be advantageous. A coating of polished silver, for example, could result in an emissivity as low as 0.02 or even less [111]. In this case the radiative heat flux would be reduced by a factor of more than 40 compared to the current emissivity of 0.82. Additionally, this would have a positive effect on the accuracy of the temperature measurements, because they can also be affected by the radiation from the heat source.

3.3 Comparison of experiments and simulations

In this part the two previous sections are linked and experimental and simulation results are compared with each other. Although a number of possible improvements for further experiments have been identified, e.g. to either prevent or measure the conductive heat loss to the floor, to reduce the radiative fraction of the total heat input and to further investigate the bending of the plume to one side, the experiments presented provide a sound basis for validation.

3.3.1 Boundary conditions

As already discussed in Section 3.2.3, radiation is the dominant mode of heat transfer even for the lowest power setting. As a result, the emissivity of the

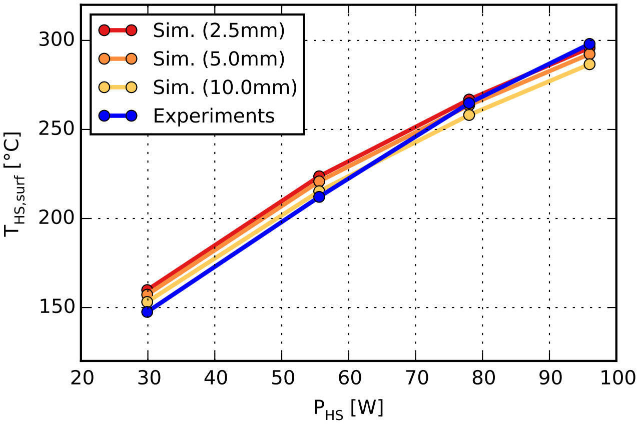

Figure 3.34: Comparison of surface temperatures on top of the heat source.

heat source is an important input parameter for the simulations, because it determines the radiative and convective fraction. In the simulations the specific net heat flux is prescribed as a boundary condition for the heat source, see Section 3.2.1. In order to realize the prescribed net heat flux, the surface temperature is increased in FDS until the sum of radiative and convective heat flux equals the prescribed net heat flux. It therefore follows that an emissivity that is too low leads to a radiative fraction that is too low. FDS will subsequently increase the surface temperature further in order to increase the net heat flux. The accordance of the heat source surface temperatures can therefore also be used as an indicator for the agreement of the emissivities in both experiment and simulation.

In Figure 3.34 the surface temperatures on top of the heat source are compared for different power settings in experiment and simulation. The surface temperatures in the experiments are derived from the measured values T_{HS} corrected by the fitted function shown in Figure 3.13. In the simulations the surface temperature can be recorded directly. With refined grid resolution the simulations result in higher surface temperatures. In simulations with 2.5 mm instead of 10 mm the surface temperature is on average 8 K warmer.

For lower power settings the simulations overestimate the surface temperature, while for higher power settings they agree well or slightly underestimate the surface temperature. In numbers, the simulation with 10 mm resolution deviates by 6 K at 30 W, and by −11 K at 96 W. The simulation with 2.5 mm cell size deviates by 12 K and by −2 K at the same power set-

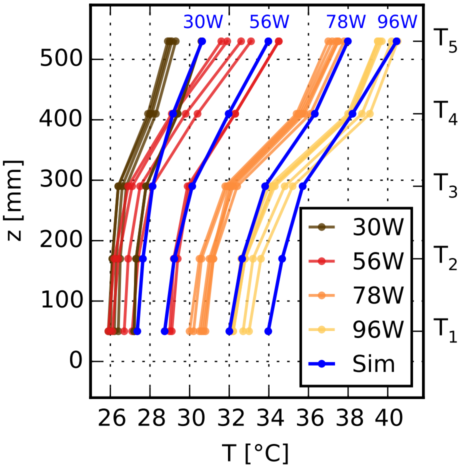

Figure 3.35: Comparison of temperature stratification inside the enclosure for different power settings, measured by the devices T_1 to T_5. The simulation with 2.5 mm resolution is shown, time-averaged from 180 s to 190 s.

tings. From these values it becomes evident that there is no general over- or under-estimation of the surface temperatures, which suggests that the measured emissivity is reasonable.

In Figure 3.16 the temperature stratification inside the enclosure is evaluated for the experiments. It is now possible to extend this evaluation to include the simulation results. From Figure 3.35 it becomes evident that simulation and experiment mainly correlate well. For the two lowest power settings the simulation results lie among the experimental results. For the two highest power settings the gas temperatures correlate well for the upper part of the enclosure but have been overestimated by the simulations within the lower layer. Consequently the interface between the two layers is less distinct. The temperature drop from 400 mm to 300 mm height is only a little more than 2 K in the simulations, compared to almost 4 K in the experiments.

In order to examine the influence of the grid resolution the temperature profiles for $P_{HS} = 96\,\mathrm{W}$ are shown enlarged in Figure 3.36. Additionally, temperature profiles from simulations with 10 mm, 5 mm and 1.25 mm have been plotted. As can be seen from the figure, with increasing resolution the simulation results become more similar to the experimental measurements.

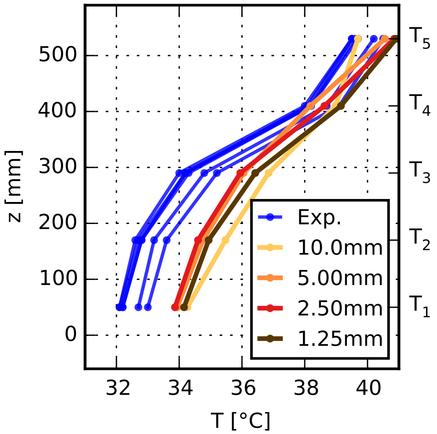

Figure 3.36: Temperature stratification in simulations with different grid resolutions at $P_{HS} = 96\,\mathrm{W}$, time-averaged from 180 s to 190 s.

The simulations with 1.25 mm and 2.5 mm both exhibit realistic temperature gradients over the height. However, both overestimate the temperatures for $z < 300\,\mathrm{mm}$. Nevertheless the overall agreement is regarded as good, especially when considering the existence of measurement uncertainties in the experiments.

3.3.2 Flow pattern

Now that the similarities of experiment and simulation regarding the boundary conditions have been evaluated, the flow velocities inside the plume – the central element of validation – can be compared. Figure 3.37 shows flow fields at $P_{HS} = 96\,\mathrm{W}$. Figure 3.37a is based on data from the experimental run 11.1, the other sub-figures are of simulations with different grid resolutions. The blue lines indicate the positions where the velocity profiles are derived. It becomes evident from the figure that not all the simulations can reproduce the flow pattern visible in the experiments. In the simulations with cell sizes of 10 mm or 5 mm there is no transition to a turbulent plume that is accompanied by a widening in the upper half. Neither is there a narrowing of the flow directly above the heat source, which is visible in the experiments and in the highly resolved simulations. Apparently the simulations with 2.5 mm or 1.25 mm resolution show good correlation with the

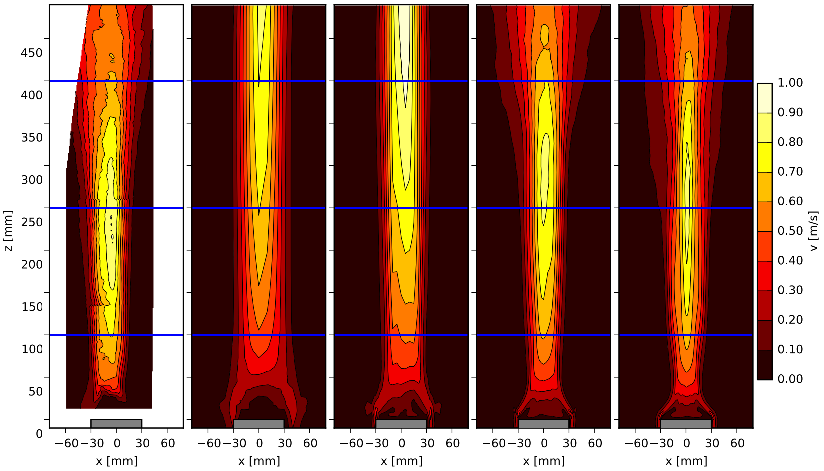

(a) Run 11.1 Experiment (b) 10.0 mm Simulation (c) 5.0 mm Simulation (d) 2.5 mm Simulation (e) 1.25 mm Simulation

Figure 3.37: Time-averaged velocity fields at $P_{HS} = 96\,\mathrm{W}$ in experiment and simulation. Run 11.1 is taken as exemplary data for the experiments.

experiments at at $P_{HS} = 96\,\mathrm{W}$.

In order to give an overview of all the heat inputs investigated the velocity profiles of all experiments and simulations are presented in Figure 3.38. The approach is identical to that described in Section 3.1.4 and considers only the vertical velocity component, v_z. Due to the long computing time the finest resolution of 1.25 mm was only applied for the highest power setting.

In general there seem to be notable deviations between experiments and simulations. However, this impression is partly caused by the bending of the plume which leads to a shifting of the flow profiles. In the simulations the plume rises vertically above the heat source, whereas in the experiments the flow profiles are shifted to the left. Possible reasons for this bending of the plume have already been discussed in Section 3.1.4.

Interestingly, the phenomenon of a double or hollow plume, which could be observed in some of the experimental runs at low heat inputs, also occurred in the simulations. At a power setting of 30 W the simulation with 5 mm grid resolution exhibits two velocity peaks each at 250 mm and 400 mm height. So far there is no explanation why this occurs only at this power setting and this specific resolution. However, the fact that it can be reproduced by FDS allows this phenomenon to be studied by simulations in the future.

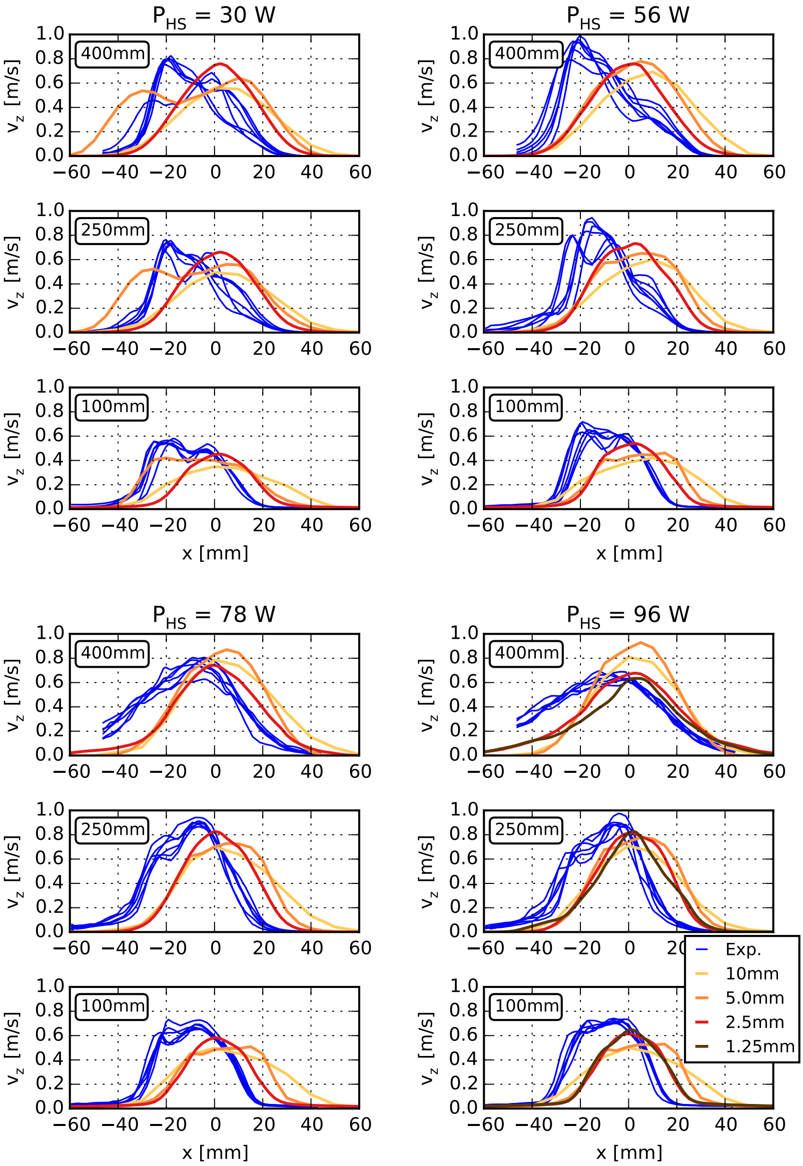

Figure 3.38: Comparison of v_z velocity profiles between experiments and simulations. The subfigures show the different heat outputs, for each of which three different heights are investigated.

In order to further compare and quantify the similarity of experiments and simulations, characteristic values are derived, i.e. the maximum velocities, plume widths and flow integrals. In Figure 3.39a, Figure 3.39b and Figure 3.39c those values are displayed for different heights. The blue shaded area represents the range of experimental values with the highest and lowest value removed at every power setting, which means that two thirds of the experimental measurements are included in this area.

With regard to the maximum velocities shown in Figure 3.39a the 2.5 mm simulations show the best agreement with the experiments, despite their tendency to underestimate the maximum velocities slightly. Not only is the relative deviation the smallest – no more than approximately 15 % – the inversely proportional relation of flow velocity and heat input at the top position can also only be reproduced by simulations with a sufficiently fine resolution.

A similar picture emerges when comparing the plume widths in Figure 3.39b. They have been calculated based on a velocity threshold of 0.2 m/s for both the experiments and the simulations. Again, the 2.5 mm simulations show the best overall correlation with the experimental measurements. For most heights and heat inputs they lie close to or within the experimental measurements. Only for the highly turbulent parts of the plume (in 400 mm height at high heat inputs) the 2.5 mm simulations also underestimate the plume width. Nevertheless only the finest resolved simulation correctly predicts the widening of the plume at increasing heat inputs, while the other simulations predict constant or declining plume widths at 400 mm height. The 5 mm simulations exhibit an outlier at 30 W, which is caused by the double plume described above. Although the same phenomenon has also been observed in the experiments, it apparently results in a much wider plume in the simulations.

The calculation of the flow integrals is used as a substitute value for the induced volume flow, which could not be measured with 2D PIV in the experiments. Figure 3.39c shows the comparison of simulated and experimental flow integrals. Here the simulations with the coarsest resolution of 10 mm show the best overall agreement, despite the huge deviations that have been visible in maximum velocity and plume widths. At this resolution the underestimation of the flow velocities and the overestimation of the plume widths seem to level out for the calculation of the flow integrals. The 2.5 mm simulation shows deviations of up to 20 % at the lowest height of 100 mm but agrees reasonably well at the middle and top position. The 5 mm simulation again exhibits an outlier at 30 W heat input caused by the double plume.

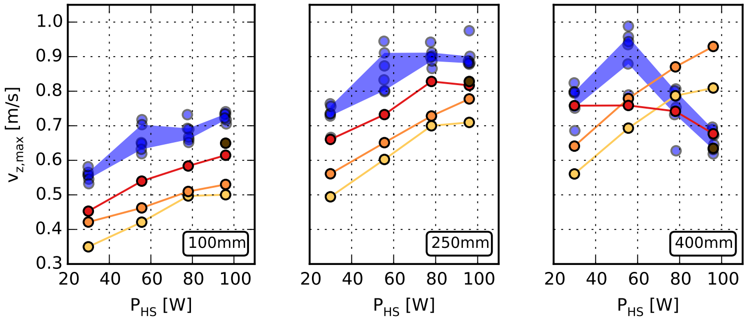

(a) Maximum velocities

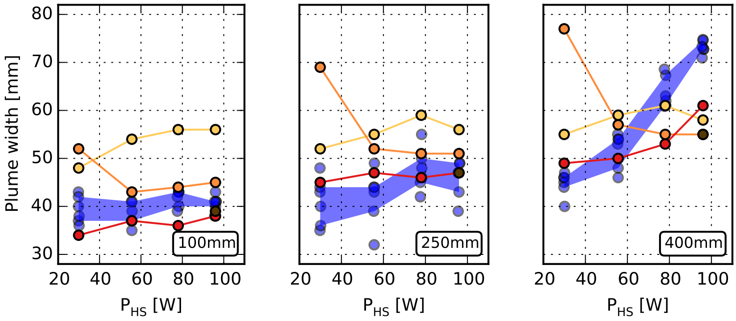

(b) Plume widths

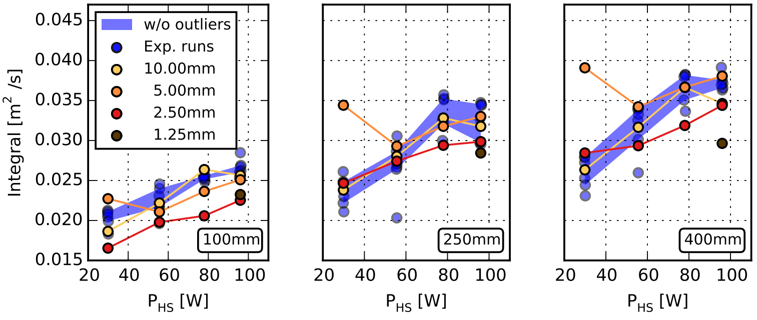

(c) Flow integrals

Figure 3.39: Comparison of characteristic flow values in experiments and simulations.

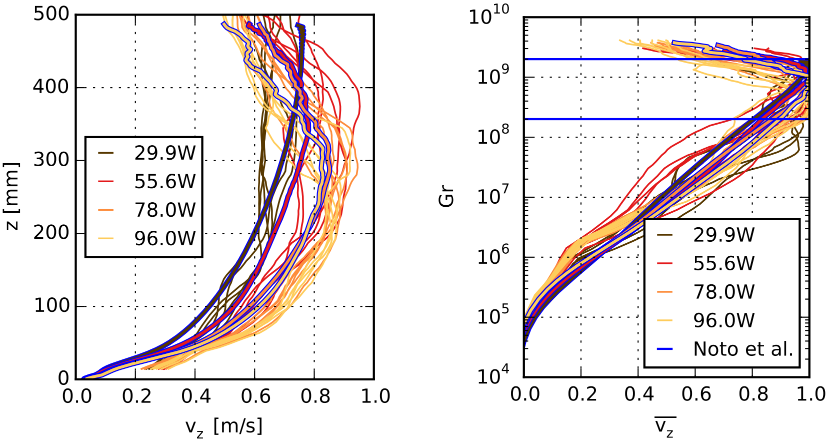

(a) $v_z(z)$

(b) $\overline{v_z}(Gr)$

Figure 3.40: Vertical velocity and normalized vertical velocity in the centerline of the plume. The simulation curves (framed in blue) are obtained with 2.5 mm resolution.

3.3.3 Plume centerlines

In Figure 3.40 the vertical velocity $v_z(z)$ and the normalized vertical velocity $\overline{v_z}(Gr)$ are shown. A sophisticated method for fitting the centerline, as it was applied for the experiments, is not required for the simulations. The plumes rise vertically and thus the centerline lies on the z axis.

The development of v_z as a function of z is very similar in both simulation and experiment. Both the gradient in low heights and the velocities close to the ceiling are similar. The maximum velocities are also attained at approximately the same heights. The maximum velocities themselves, however, are underestimated by the simulations, as already shown in Figure 3.39a. Due to the normalization the differences in the maximum velocities no longer exist in Figure 3.40b. The normalized simulations lie among the experimental results with regard to the transition from laminar to turbulent flow.

A reliable measurement for determining the transition from a laminar to a turbulent flow is the standard deviation of v_x along the centerline. While the velocity components perpendicular to the flow direction of a laminar flow are small, the passing eddies of a turbulent flow create many fluctuations in all directions. Figure 3.41 shows the standard deviation $\sigma(v_x)$ as a function

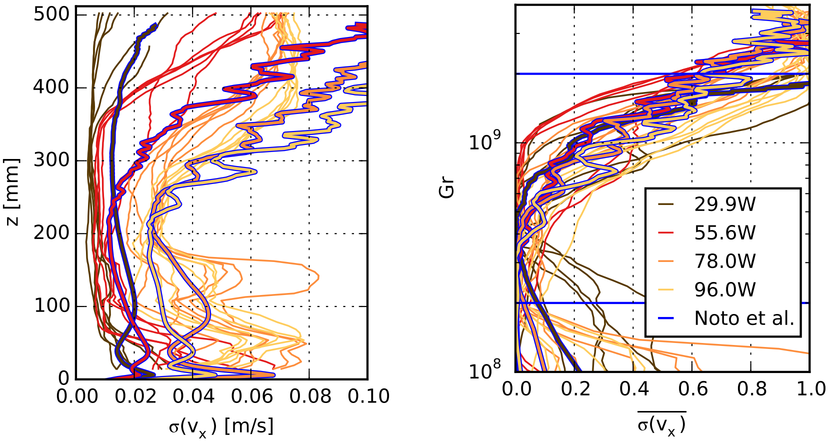

(a) $\sigma(v_x)$ as a function of z for the entire plume height.

(b) $\overline{\sigma(v_x)}$, as a function of Gr. Enlargement of the transitional region.

Figure 3.41: Standard deviation and normalized standard deviation of v_x in the centerline of the plumes. The simulation curves (framed in blue) are obtained with 2.5 mm resolution.

of z and the normalized standard deviation $\overline{\sigma(v_x)}$ as a function of the Grashof number.

When comparing $\sigma(v_x)$ as a function of z, the simulations generally exhibit higher values than the experiments, and there are stronger horizontal fluctuations along the centerlines. In addition, a sharp bend, as it can be found for experiments at $P_{HS} = 55.6\,\mathrm{W}$ is not visible in the simulations. Nevertheless the general agreement is considered good, especially when normalizing the data and evaluating it as a function of the Grashof number, as in Figure 3.41b.

As a general conclusion from this chapter, it can be summarized by stating that it is important to incorporate all values into a grid sensitivity and validation study that are intended to be evaluated later. As can be seen in Figure 3.39c, the 10 mm simulations show a very good agreement with the flow integrals measured in the experiments. However, for other characteristic values, as shown in Figure 3.39b and Figure 3.39a, the 10 mm simulations performed worst, because the general flow characteristics are not reproduced, as shown in Figure 3.37. The underlying reason is that the coarse mesh resolutions do not reproduce the transition from laminar to turbulent flow.

Therefore, whenever the turbulent nature of a flow is important, it must be guaranteed that this turbulent nature is reproduced in the respective simulations. Turbulence not only has an effect on the plume width but also on the entrainment of air, the mixing of fire products, and the dissipation of kinetic energy from larger scales into internal energy by viscous shear stress. Therefore, it has an immediate effect on important phenomena in fire safety engineering, for example when designing natural smoke ventilation systems or modeling the activation of smoke detectors.

Chapter 4

A spill plume emerging from a compartment opening

The setup described in this chapter is of more practical relevance for fire safety engineering than the previous setup. Many, if not most, of the fires that are dealt with in fire safety engineering are compartment fires. These fires are ventilated by compartment openings and the fire itself or its products spread through openings within these compartments. To mimic this setup in the experiments, the heat source is now placed inside a compartment with a single door-shaped opening.

This simple setup already includes many interesting and relevant phenomena. A buoyant plume rises from a heat source, impinges on the ceiling and spreads horizontally as a ceiling jet. After a short period of time, a hot upper and a colder lower layer develop. In the case of a real, sufficiently intense fire, the first would usually be smoke-filled while the latter would contain only a little smoke. This low-smoke lower layer is important to maintain, because it allows occupants to escape and fire fighters to take extinguishing measures. Due to the formation of the hot gas layer inside the compartment, an overpressure develops in the upper part of the compartment. The hot air flows out through the upper part of the door. This again causes a negative pressure at the lower part of the compartment, which sucks in ambient air from outside the compartment. Because there is only a single opening, both the outflow and inflow run through the same opening. This counterflow induces a shear flow at the neutral level. Mass is neither added nor extracted to or from the compartment elsewhere, so the mass balance of incoming and outgoing flow through the door has to be maintained at a steady state. This means that the incoming and outgoing mass flows are equal. Because the outflowing air is warmer and thus less dense than the inflowing air, the outgoing volume flow will be greater than the incoming volume flow. It therefore follows that the outflow runs at higher velocity and/or covers a larger area of the opening than the inflow.

The entire setup is based on the previously described open plume experiments: for example the same enclosure is used to confine the particles, the same equipment is applied, and temperatures are measured at the same positions. Therefore, in this chapter, only differences or additions to the former setup are described, both for the experiments and simulations.

4.1 Experiments

Due to its generic relevance for fire safety engineering, similar setups have already been investigated several times with different aspects. A widely recognized investigation on the subject was conducted in 1982 by Steckler et al. [46], who performed 55 full-scale steady state experiments to study the flow induced by a fire in a compartment. The geometrical setup in the present study is inspired by Steckler's experiments. For example, the dimensions of the room and the opening as well as the position of temperature measurements within the room are similar. The present study, however, is carried out in bench-scale, uses an electrical heat source instead of a real fire, and applies PIV instead of bidirectional velocity probes for measuring the flow through the opening.

4.1.1 Experimental setup and procedure

The heat source is now positioned in the middle of a compartment with a single door-shaped opening, as can be seen in Figure 4.1 and Figure 4.2. The compartment's inner dimensions are 300 mm × 300 mm × 240 mm ($l \times w \times h$). The walls and ceiling are made out of 10 mm thick polymethyl methacrylate (PMMA). The front wall, which includes the opening, is not glued but rather screwed to the compartment and thus removable. This allows different opening geometries and wall strengths to be investigated. In the present study, two doors of 80 mm and 40 mm width are investigated, both with a height of 200 mm. This results in a door lintel height of 40 mm (inner dimension).

Additional temperature measurements are taken in one corner of the compartment, at positions T_7 to T_{11}. They are placed at a distance of 30 mm to both adjacent walls and are 40 mm apart from each other. The distance from T_7 to the floor and T_{11} to the ceiling is also 40 mm. PIV measurements are taken outside the compartment in front of the door, as can be seen in Figure 4.3. Therefore, the laser light sheet is placed parallel to the predomi-

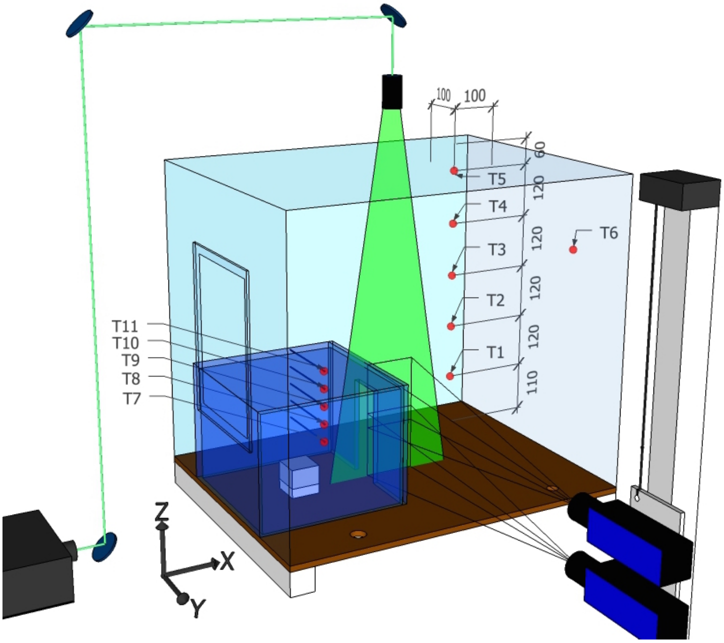
100
100
60
120
120
120
120
110
T5
T4
T3
T2
T1
T6
T11
T10
T9
T8
T7
Z
X
Y

Figure 4.1: Experimental setup: The heat source is placed inside a compartment with one opening. Pt100 devices measure the temperature at positions T_1 to T_{11}. The inflow and outflow through the opening is measured via PIV. Dimensions are given in mm, the coordinate origin is defined at the floor surface in the middle of the door, in alignment with the outer front wall of the compartment.

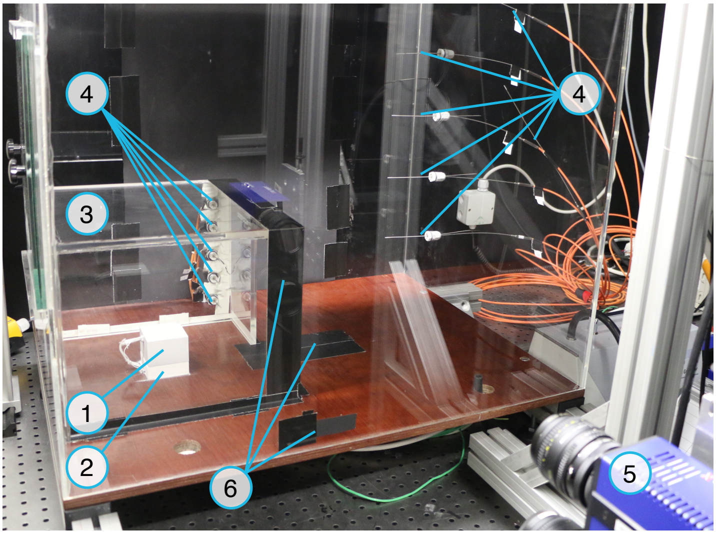

(a) The compartment is placed on the left side inside the enclosure.

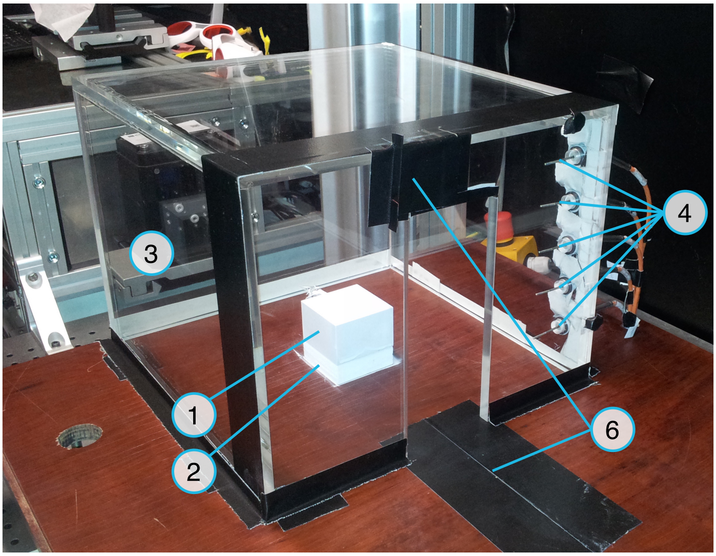

(b) Close-up of the compartment.

Figure 4.2: Experimental setup of the spill plume experiments. Shown are heat source (1), insulating base (2), compartment (3), Pt100 temperature devices (4), CCD Cameras (5), and black tape for reducing reflections (6).

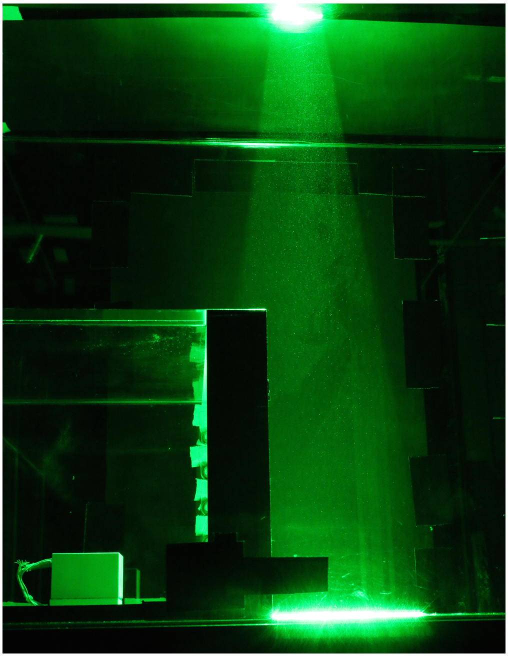

Figure 4.3: Laser light sheet in front of the compartment opening during the experiments. Note, this photograph has been taken with a standard SLR camera, not with the PIV cameras.

nant flow direction through the door, i.e. orthogonal to the front wall. This is important to reduce the loss-of-pairs due to out-of-plane movement of the particles.

In contrast to the previous open plume experiments, the cameras are no longer moved. Instead, they are set to a fixed position so that the viewing area of the lower camera begins just above the floor. Positioning a few millimeters above the floor is necessary to avoid laser light being reflected into the camera. Since the combined viewing area of both cameras is 246 mm high, the entire door height and the door lintel can be covered without having to move the cameras.

However, it is desirable to obtain PIV recordings not only in the center of the opening but also closer to the sides of the door. The flow in the center is expected to be faster than close to the sides, where it is slowed down by the friction with the door frame. So, in order to record the velocities at different positions in front of the opening, the entire enclosure is moved backwards

Table 4.1: Abridged overview over spill plume experiments with different heat inputs, P_{HS}, and the associated standard deviation. N is the number of experimental runs, t_m is the duration of each measurement and f is the camera frame rate.

Door width mm	P_{HS} W	T_{HS} °C	N	t_m s	f Hz
80	29.7 ± 0.0	150.0 ± 0.0	2	10	10
80	55.4 ± 0.1	218.0 ± 0.0	4	10	10
80	77.6 ± 0.3	270.0 ± 1.4	2	10	10
80	96.7 ± 1.0	306.3 ± 0.5	2 2	10 180	10 1
40	29.5 ± 0.0	150.7 ± 0.6	2 1	10 180	10 1
40	55.2 ± 0.1	218.7 ± 0.6	2 1	10 180	10 1
40	77.4 ± 0.1	269.7 ± 0.6	2 1	10 180	10 1
40	95.8 ± 0.4	306.0 ± 0.0	2 1	10 180	10 1

in discrete steps of 10 mm (at 80 mm door width) or 5 mm (at 40 mm door width). Moving the enclosure with the experimental setup inside is preferable to moving the cameras and the light sheet, so that the focus and calibration of the cameras are guaranteed to remain the same.

By doing so, four PIV measurements per experimental run are recorded, one at the center of the opening and three closer to the sides of the opening. The flow through the door is expected to be symmetrical, so only one half of the opening is scanned. Table 4.1 gives an abridged overview of all experimental runs conducted, a complete overview is provided in the appendix.

4.1.2 Image processing

The entire processing of the particle images into velocity vector fields is very similar to that of the open plume experiments. Again, the images are calibrated by placing a target at the position of the light sheet. Here, the coordinate origin is selected at the floor surface in the middle of the door, in

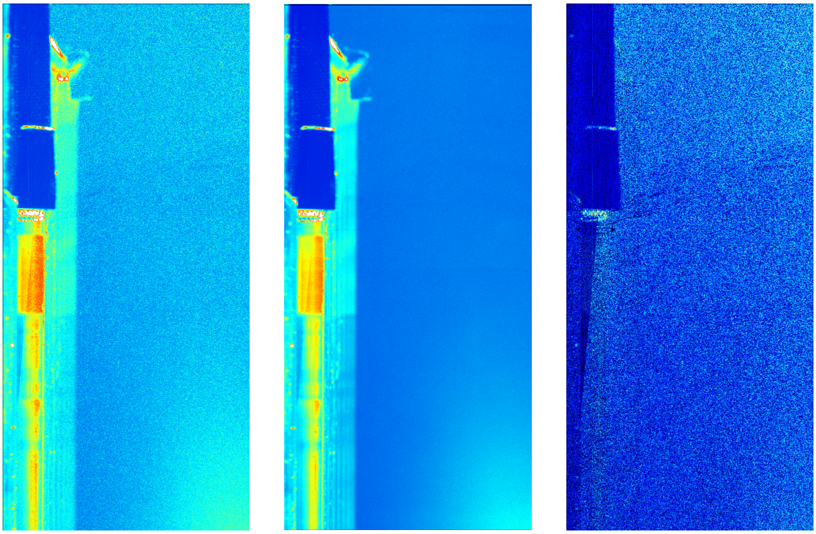

(a) Original (b) Background (c) Difference

Figure 4.4: Background subtraction from raw particle images. Illustrated by an image taken from the spill plume experiment 1.1. The background calculates as the minimum intensity image of all images at that position.

alignment with the outer front wall of the compartment. So, for example, the opening of the door of 80 mm width extends from $x = -10\,\text{mm}$ to $x = 0\,\text{mm}$, from $y = -40\,\text{mm}$ to $y = 40\,\text{mm}$, and from $z = 0\,\text{mm}$ to $z = 200\,\text{mm}$.

The subtraction of the background images is even more important here, because parts of the compartment geometry are visible in the background. By subtracting the minimum of all images at the same position, the quality of the particle images can be substantially improved, i.e. individual particles are easier to distinguish. An example of this can be seen in Figure 4.4.

Subsequently, an iterative multigrid approach is used for the vector calculation, with the interrogation window size being reduced from 128 pixels × 128 pixels to 64 pixels × 64 pixels. With an overlap of 50 %, this results in a final resolution of approximately 2.75 mm.

4.1.3 Experimental results

As a first step, the reproducibility of the experiments with regard to the ambient conditions is investigated. In Figure 4.5, the scattering of the heat

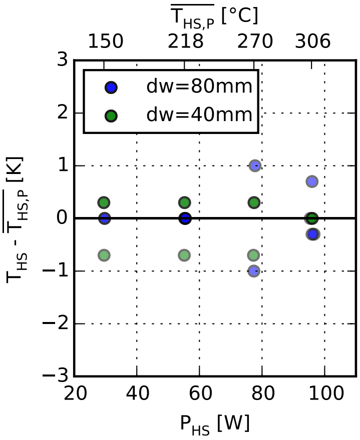

Figure 4.5: Scattering of heat source temperatures during the spill plume experiments. The figure displays the deviation of each heat source temperature from the mean heat source temperature at every power setting.

source temperatures is illustrated. For the experiments with both 80 mm and 40 mm door width, the heat source temperature does not deviate more than 1 K from the mean heat source temperature at each heat input.

In Figure 4.6, the temperature of the ambient air just outside the enclosure is shown. Similar to the open plume experiments, the temperatures here tend to be higher with increased heat input. This is not caused by the increased heat input itself but by the time schedule of the experiments. Runs with higher heat inputs have been carried out in the afternoon of the experimental days. By that time of day the testing facilities had heated up already. This effect is not adverse for the later simulations, because the ambient temperatures can be taken into account as boundary conditions. It is more important to keep the temperatures for all runs at a power setting as similar as possible to make them comparable with each other. This objective has been achieved; the largest deviation for experiments with identical heat input and door width is approximately 1 K.

The temperature profiles inside the enclosure at positions T_1 to T_5 are shown in Figure 4.7. As expected, the temperatures rise with increasing heat input. This is especially true for the experiments with a door width of 80 mm, which result in higher temperatures than the experiments with a door width of 40 mm. A narrower opening reduces the outflow of hot air

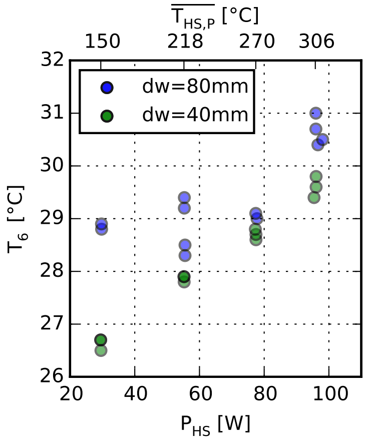

Figure 4.6: Ambient temperatures measured in a few centimeters distance to the enclosure at position T_6. The measurement error is less than 0.4 K.

from the compartment. A clear interface between hot upper and colder lower layer is not visible at both door widths, but instead the temperature rises continuously over the height. It thereby covers a temperature difference of 2 K to 6 K. The temperatures at $P_{HS} = 78\,\mathrm{W}$ and $dw = 80\,\mathrm{mm}$ seem to be lower than one would expect from a comparison with the temperatures at $P_{HS} = 78\,\mathrm{W}$ and $dw = 40\,\mathrm{mm}$. This is because, for these two runs, too little time has been given for heating up and reaching a stationary state.

For both door widths the temperature profiles of the same power setting lie very close together. This is because – with exception of the four runs at $P_{HS} = 55\,\mathrm{W}$ and $dw = 80\,\mathrm{mm}$ that have been carried out on two different days – all other runs have been conducted within a short period of time.

The air temperatures within the compartment, as shown in Figure 4.8, are considerably higher than the temperatures within the enclosure. While the highest temperature at position T_5 is about 43 °C, it is approximately 65 °C at position T_{11}. This is understandable, because the latter is measured close to the heat source. When comparing the temperature profiles inside the compartment for both door widths, higher temperatures are found with the narrower door. This is, again, because the outflow of hot air from the compartment is reduced by the smaller opening. For all experiments, there is a rapid increase in temperature between 80 mm and 120 mm, whereas the temperatures at heights greater than 120 mm show only a moderate increase.

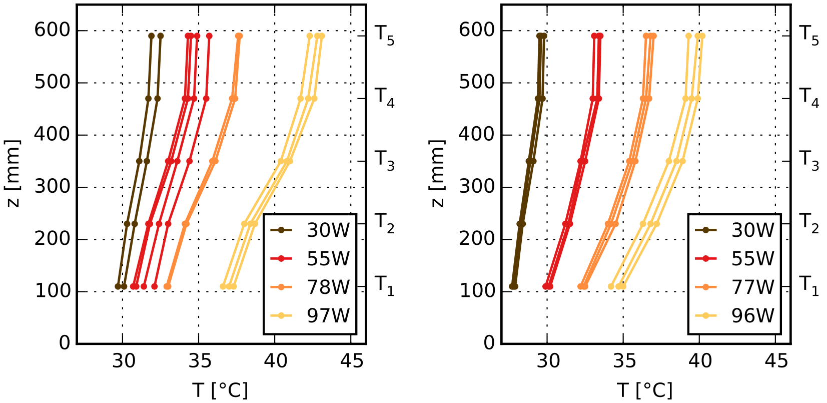

(a) Door width: 80 mm (b) Door width: 40 mm

Figure 4.7: Temperature stratification inside the enclosure measured by the devices T_1 to T_5. The enclosure's interior extends from $z = 0\,\text{mm}$ to $z = 650\,\text{mm}$. The measurement error is less than 0.5 K.

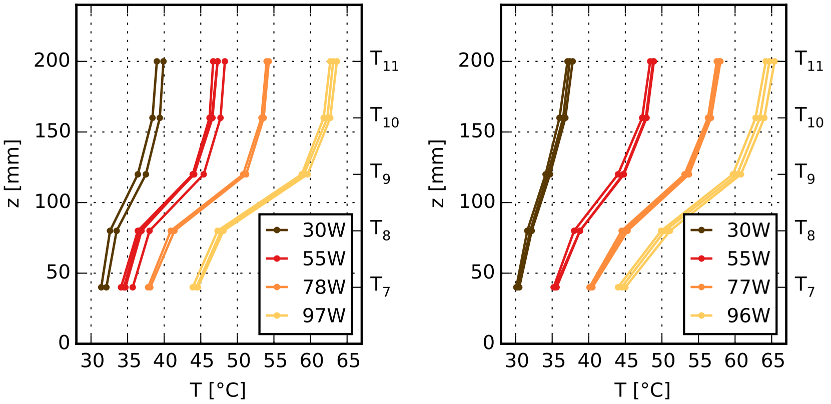

(a) Door width: 80 mm (b) Door width: 40 mm

Figure 4.8: Temperature stratification inside the compartment measured by the devices T_7 to T_{11}. The compartment's interior extends from $z = 0\,\text{mm}$ to $z = 240\,\text{mm}$. The measurement error is less than 0.6 K.

Flow pattern and centerlines

Typical instantaneous velocity fields at all investigated heat inputs and door widths are shown in Figure 4.9 and in Figure 4.10. The respective time-averaged velocity fields are shown in Figure 4.11 and in Figure 4.12. The compartment geometry and the opening are illustrated in sectional view by the areas shaded in gray. The recordings are taken at the center of the door (at $y = 0\,\mathrm{mm}$) and are time-averaged over 10 s and 100 images. Due to light reflections, measurements close to the floor (for $z < 5\,\mathrm{mm}$) and in front of the door lintel (for $0\,\mathrm{mm} < x < 12\,\mathrm{mm}$ and $200\,\mathrm{mm} < z < 250\,\mathrm{mm}$) have not been possible.

As expected, the air is flowing into the compartment (in negative x-direction) at the lower part of the door and out of the compartment (in positive x-direction) at the upper part of the door. The maximum velocities of the outflow are lower compared to those in the open plume experiments, because in this setup the flow is not flowing freely above the heat source, but instead is slowed down and deflected by the compartment ceiling and lintel. The maximum inflow velocities are much lower than the maximum outflow velocities. There are several reasons for this occurrence:

1. The inflow covers a larger area of the door and thus the same volume flow is achieved at a lower velocity.
2. The outgoing volume flow exceeds the incoming volume flow, because the outflowing air is warmer and thus less dense. Only the mass balance of incoming and outgoing flow is leveled, but the volume flows are not.
3. With increasing distance to the opening, the outflow is also accelerated by buoyancy, so the vertical velocity component v_z increases.
4. The outflow, which is pushed out of the compartment by the overpressure inside, has momentum towards a positive x-direction and therefore a jet develops. The inflow, however, is sucked in by the negative pressure gradient in the lower part of the compartment. Such an aspiration accelerates air in the entire region around the opening, also in the y-direction. In other words, while the outflow is mainly parallel to the measurement area, the inflow exhibits a stronger three-dimensional behavior. For that reason, with increasing distance to the opening, the inflow decreases at a greater rate than the outflow.

With increasing heat input, the outflow velocity increases. This is caused by the higher air temperatures, which increase the volume flow out of the compartment. In all experiments, the plume is clearly detached from the

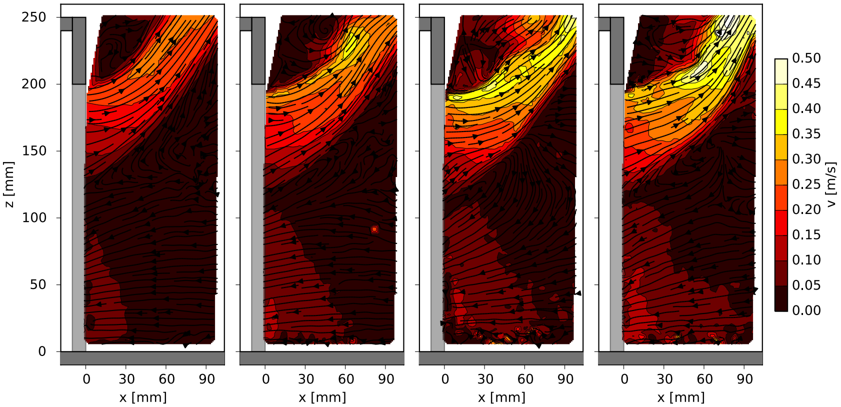

Figure 4.9: Typical instantaneous velocity fields in the center of the door with $dw = 80\,\mathrm{mm}$. From left to right heat inputs of 29.7 W, 55.5 W, 77.8 W and 96.6 W are shown.

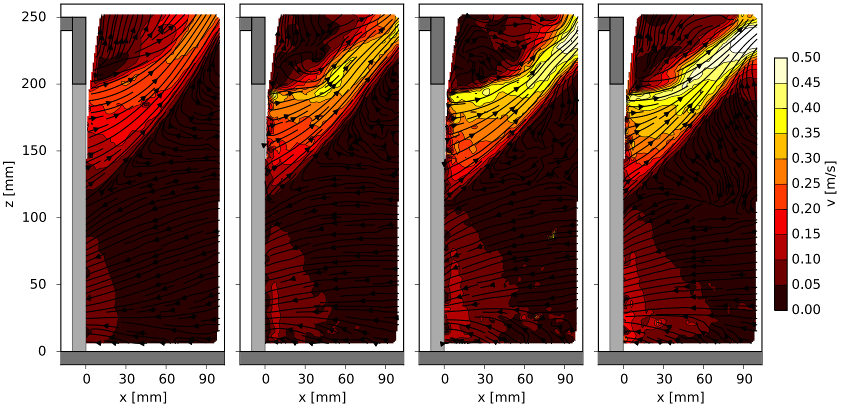

Figure 4.10: Typical instantaneous velocity fields in the center of the door with $dw = 40\,\mathrm{mm}$. From left to right heat inputs of 29.5 W, 55.3 W, 77.5 W and 96.0 W are shown.

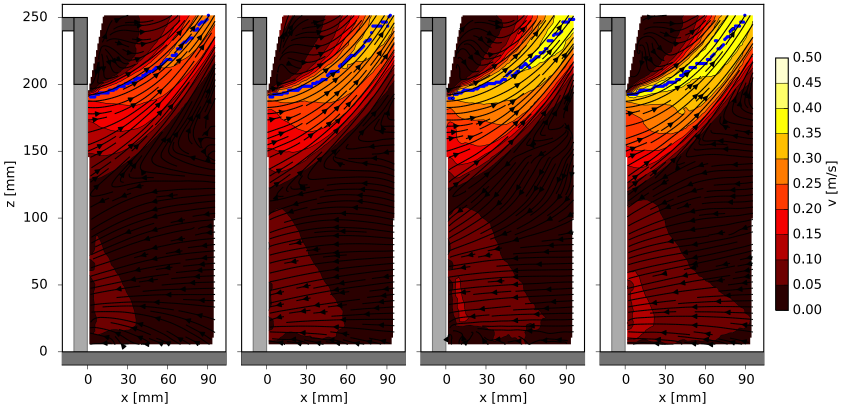

Figure 4.11: Velocity fields in the center of the door with $dw = 80$ mm, time-averaged over 10 s. From left to right heat inputs of 29.7 W, 55.5 W, 77.8 W and 96.6 W are shown. The blue dots indicate the centerline in the outflow.

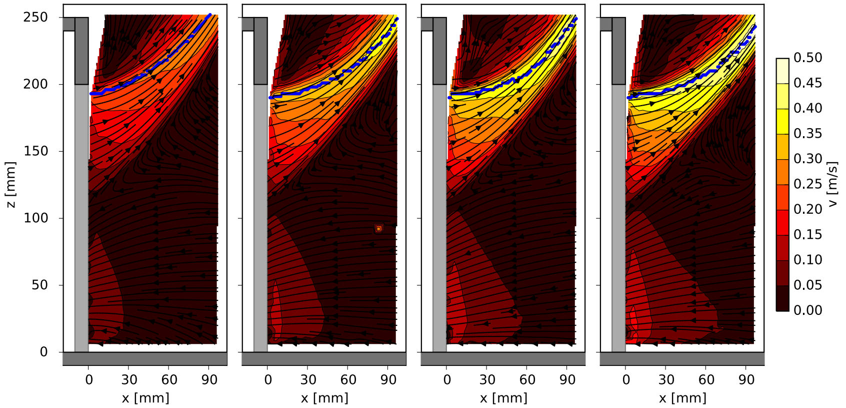

Figure 4.12: Velocity fields in the center of the door with $dw = 40$ mm, time-averaged over 10 s. From left to right heat inputs of 29.5 W, 55.3 W, 77.5 W and 96.0 W are shown.

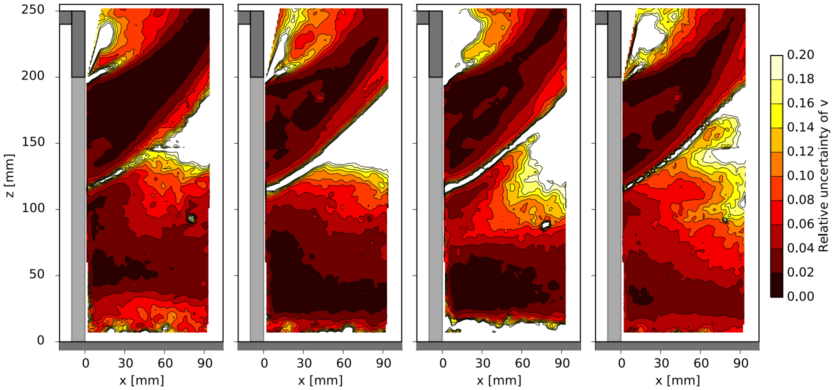

Figure 4.13: Relative measurement uncertainties belonging to Figure 4.11 with $dw = 80\,\text{mm}$. From left to right heat inputs of 29.7 W, 55.5 W, 77.8 W and 96.6 W are shown.

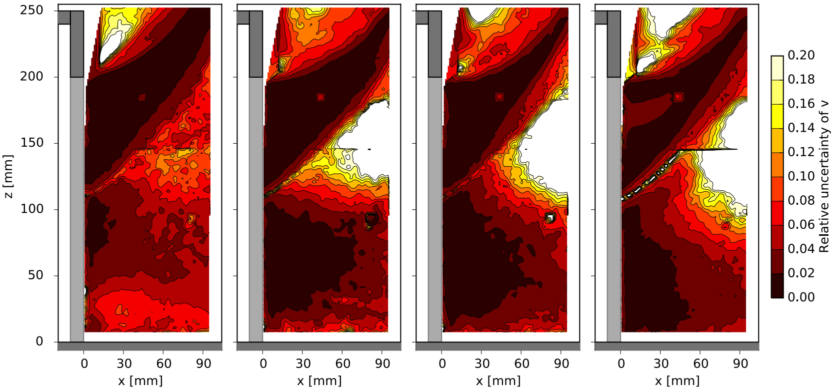

Figure 4.14: Relative measurement uncertainties belonging to Figure 4.12 with $dw = 40\,\text{mm}$. From left to right heat inputs of 29.5 W, 55.3 W, 77.5 W and 96.0 W are shown.

door lintel above the opening. This is in accordance with previous studies on plumes emerging from compartment openings [112–115]. These studies found that the aspect ratio (height to width) of the opening is crucial for the plume behavior. The wider the opening, the more likely it is that the plume attaches to the facade above. For narrower openings, such as the doors used in this study, the plume is usually detached from the lintel above.

For a closer investigation of the plume behavior, the centerlines are determined. Here, the maximum (absolute) velocity in the outflow is defined as the centerline. It is marked by blue dots in Figure 4.11 and in Figure 4.12. For the investigated setups, the position of the centerline appears to be independent of the heat input and the door width. This is more closely investigated for all experiments later in this section.

When comparing experiments at both door widths with each other, the narrower door of $dw = 40\,\text{mm}$ exhibits higher flow velocities at identical heat inputs. This is because the flow undergoes a stronger acceleration in the narrow opening. Another difference is the vertical extension of the outflow at some distance to the opening. Although the narrower door has the same height as the wider door, it leads to a more focused outflow, even in a vertical direction.

For both door widths the highest inflow velocity can be observed at approximately $x = 10\,\text{mm}$. This behavior cannot be physically explained, because a constant volume flow must have its highest velocity at its narrowest point. In the present setup this would be the door, and thus the highest velocity of the inflow should be observed at $x = 0\,\text{mm}$. This does not apply to the outflow, which undergoes a vertical acceleration in front of the opening due to its buoyancy. The reason why the inflow seems to decelerate inside the door can be seen in Figure 4.4. The doorjamb, which is in the background of the affected region, is illuminated by the laser light and outshines the particles. Although the background subtraction improves the image quality substantially, it is apparently not able to compensate it entirely.

This assumption is supported by the measurement uncertainties determined with DaVis [107,108], as shown in Figure 4.13 and in Figure 4.14. For some of the measurements the uncertainty is significantly increased close to the opening ($x < 10\,\text{mm}$). In addition to this area, an increased uncertainty can also be found at the borders of the plume and in the boundary layer between inflow and outflow. In this shear flow region, where the relatively fast-moving outflow interacts with the stationary ambient air and the inflow respectively, uncertainties of more than 20 % can be observed. However, one should keep in mind that the relative uncertainty is calculated by dividing the absolute measurement uncertainty by the absolute flow velocity. Therefore, in regions with low flow velocities – outside or at the borders of the

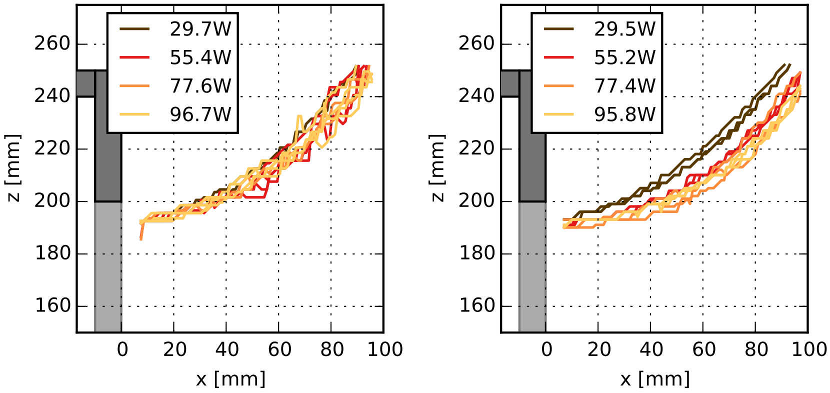

(a) Door width: 80 mm (b) Door width: 40 mm

Figure 4.15: Centerlines for 80 mm and 40 mm door width.

plume – the relative measurement uncertainty is high, although the absolute error is small. In the center of the outflow, where the centerlines are derived, the uncertainty is approximately 2 % to 4 %. In addition to the measurement error discussed above, another error is introduced by neglecting v_y, the velocity component normal to the measurement plane. One study that applied stereo PIV to investigate the effect of this simplification concluded that the introduced error is less than 5 % [49].

In Figure 4.15 the centerlines of all conducted experiments are displayed. The centerlines are defined as the maximum (absolute) velocity in the spill plume emerging from the compartment opening. For a door width of $dw = 80\,\text{mm}$, the centerlines are independent of the heat input, at least for the range of heat inputs investigated in this study. The centerlines at $dw = 40\,\text{mm}$ seem to be influenced by the heat input: Centerlines at higher heat inputs exhibit a slightly more horizontal path than the others. This might be caused by an increased horizontal momentum with an increased exit velocity of the outflow. The differences are small, however, and a larger sample size would be required to quantify this effect.

Significant differences can, however, be seen when comparing the flow velocities along the centerlines, as shown in Figure 4.16. Comparing different heat inputs, the average velocities of the centerlines differ by 0.3 m/s to 0.6 m/s. When comparing both door widths, the centerline velocities differ by approximately 0.1 m/s to 0.5 m/s at identical heat inputs. The flow

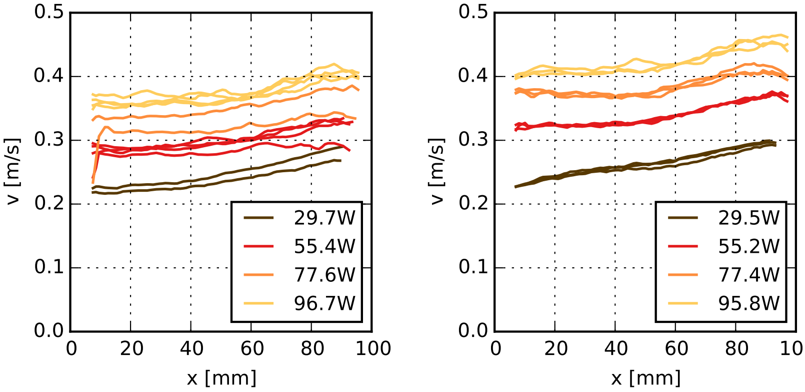

(a) Door width: 80 mm

(b) Door width: 40 mm

Figure 4.16: Flow velocities along the centerlines as a function of x.

velocity increases along every centerline, which is caused by the vertical acceleration due to buoyancy. A more detailed analysis of the individual velocity components of the centerlines is presented later on in Figure 4.27.

Volume flows in front of the opening

The velocity measurements recorded at different y positions in front of the opening are now used to estimate the volume flows that are moving into and out of the compartment. As described above, the measurements close to the opening are not considered to be reliable, so the volume flows at a distance of 10 mm to the opening are calculated. In Figure 4.17, the velocity fields for both door widths are shown.

The areas shaded in gray indicate the compartment geometry and the floor, with a white patch representing the opening. The vertical arrays of dots at y positions -30, -20, -10 and 0 for $dw = 80\,\mathrm{mm}$ and at -15, -10, -5 and 0 for $dw = 40\,\mathrm{mm}$ represent the positions of the measurement planes, which are perpendicular to the y-axis. The flow is expected to be symmetrical so, for practical reasons, measurements have only been recorded in one half of the door. Right at the doorjambs ($y = -40\,\mathrm{mm}$ and $y = -20\,\mathrm{mm}$, respectively) and at the floor ($z = 0\,\mathrm{mm}$), where measurements have not been possible due to light reflections, the velocity is set to 0. Values in between the data points are linearly interpolated, in order to allow for an estimation of the entire volume flow.

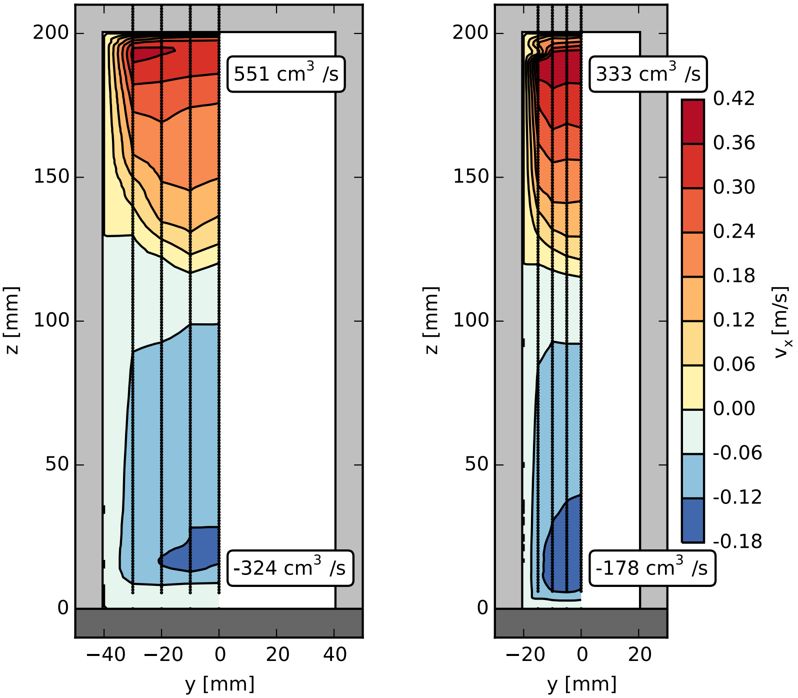

(a) Door width: 80 mm

(b) Door width: 40 mm

Figure 4.17: Volume flows in experimental runs 5.1 and 13.1 at $P_{HS} = 97\,\mathrm{W}$ and $P_{HS} = 96\,\mathrm{W}$ respectively, measured at position $x = 10\,\mathrm{mm}$. The vertical arrays of dots represent the positions of the measurement planes. Volume flows are given for half of the cross section.

As can be seen in Figure 4.17, the inflow covers a larger area of the door than the outflow. On the other hand, it flows at lower speeds. While the maximum velocities in the outflow are approximately 0.42 m/s, they do not exceed 0.18 m/s in the inflow. For the narrower door, the outflow is only about 60 % and the inflow only about 55 % of the volume flows of the 80 mm door.

In Figure 4.18 and in Figure 4.19, the velocity fields parallel to the opening for all investigated heat inputs are shown. Due to space considerations, only the half of each door that contains the measurements is plotted.

A quantitative comparison of all volume flows at $x = 10\,\mathrm{mm}$ is presented in Figure 4.20. These volume flows should not be mistaken for the true volume flows in the opening at $x = 0\,\mathrm{mm}$. The no-slip assumption at the doorjambs is only valid inside the opening. In front of the opening, the flow fans out because the horizontal velocity component v_y is non-zero. Therefore, the true volume flows inside the opening are likely to be higher. This underestimation will be greater for the inflow than for the outflow, because the inflow has a stronger three-dimensional character than the outflow has, as explained previously. A correction factor that allows for an estimation of the true volume flows inside the opening is derived based on the simulations, which are explained in the next section.

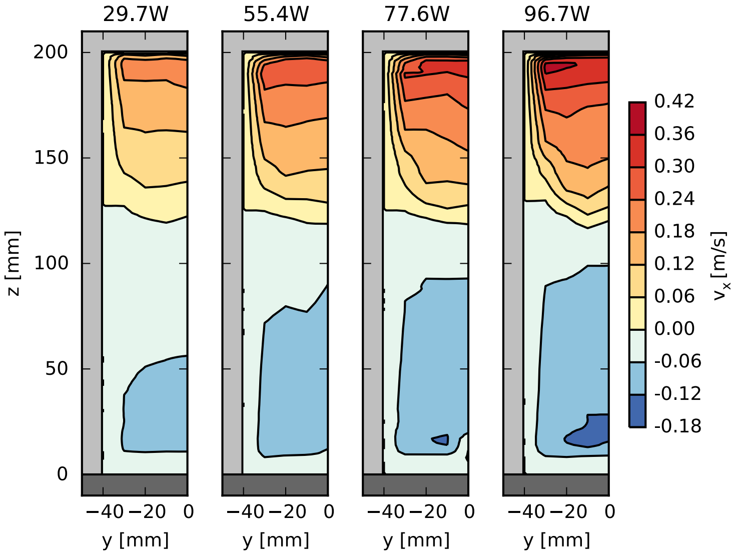

Figure 4.18: Velocity fields at $x = 10\,\text{mm}$ for a door width of 80 mm. Only one half of the door is shown.

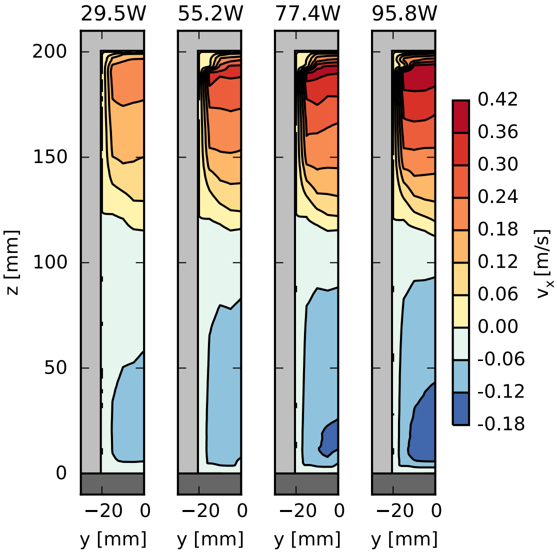

Figure 4.19: Velocity fields at $x = 10\,\text{mm}$ for a door width of 40 mm.

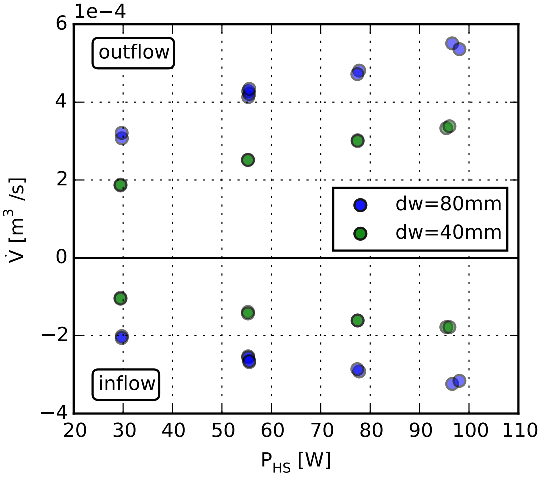

Figure 4.20: Overview of volume flows in all experiments, measured at position $x = 10\,\text{mm}$. Values are given for the half cross-section of the door.

4.2 Simulations with FDS

In the following section, the previously described experiments are modeled with the Fire Dynamics Simulator (FDS). Here, FDS version 6.3.2 is used for the simulations. The text structure is similar to that of Section 3.2, with the difference that only deviations to the former approach are explained here. A more detailed description of the fundamental simulation setup can therefore be found in Section 3.2.

4.2.1 Simulation setup

In addition to the open plume simulation setup, the compartment must also be considered in the spill plume simulations. Likewise with the enclosure, which is also made of PMMA; it is implemented with realistic material parameters in the simulations. In this way, the heat conduction through the compartment walls can be considered. The heat source's boundary condition is again prescribed as net heat flux, to guarantee that the correct amount of energy is brought into the enclosure and compartment. Additionally, the conductive losses to the wooden floor are considered according to the description on page 66.

Output values

The following quantities are recorded in addition to the output values of the open plume simulations:

- Vector slices for recording both temperature and velocity in the same positions as in the experiments, i.e. parallel to the outflow at various positions in front of the opening.
- The volume and heat flow through the door is measured by a slice file spanning the entire opening. Therefore, the flow out of and into the compartment is recorded separately.
- Inside the compartment, the air temperatures are recorded in positions T_7 to T_{11}.

Meshing and grid sensitivity

When setting up the meshes, the main focus lies on enclosing the region of primary interest with a single mesh. Here, the heat source, the compartment opening, and the region in front of the opening are most important for the flows to be observed. In order to incorporate them into a single mesh, the mesh distribution needs to be changed. The applied mesh distribution is illustrated in Figure 4.21. In order to make use of JURECA's architecture with 24 cores per node, it consists of 12 meshes. In this way, two cores per node are used for the computation of every mesh, with no core remaining idle.

The appropriate spatial resolution for the simulations is evaluated via a grid sensitivity study. Therefore, one setup is simulated in various resolutions. This is done to search for a cell size that is sufficiently high to provide resolution-independent results but as low as possible to save computation time. The results for some outputs of the spill plume setup are shown in Figure 4.22.

The temperature at position T_3 does not show a correlation with the grid resolution. Starting at about 40.5 °C, it decreases to around 38.5 °C for all cell sizes. The drop in temperature during the first 180 s already indicates that the simulations underestimate the experimental temperature at this position, because the experimental measurements have been prescribed as initial temperatures for the simulations.

The temperatures at position T_7 – the lowest temperature measurement within the compartment – show a strong correlation with the grid resolution. As shown in Figure 4.22b, a refinement of the grid leads to lower temperatures. The difference between the resolutions with 10 mm and 1.25 mm is

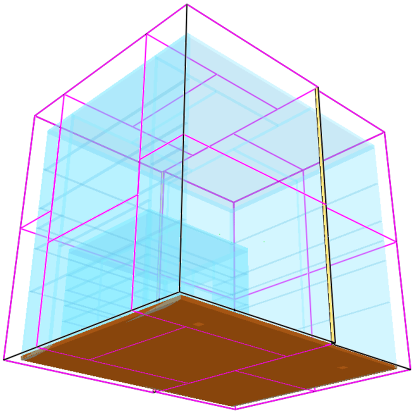

Figure 4.21: Mesh distribution for spill plume simulations.

about 6 K, which is significant for the observed temperature range. This is the most extreme case; in all other positions there is little to no correlation between temperature and grid resolution. Nevertheless, the simulation at 2.5 mm is considered the most appropriate resolution for the given setup, because it is very close to the finest resolved simulation at that position but is much faster to compute.

The volume and heat flow out of the compartment are shown in Figure 4.22c and in Figure 4.22d. Both of these measurements exhibit a peak in the first few seconds but quickly level out at a constant flow rate. There is no dependency visible on the grid resolution.

Required simulation time

Similar to the open plume simulations, the initial temperature stratification is predefined in the simulations to reduce the time required for reaching a steady state. For the spill plume experiments, the temperature profile inside the compartment has been prescribed, too. The prescribed temperature values originate from the temperature measurements observed during the experiments.

As can bee seen in Figure 4.22, due to the predefinition of air temperatures, a heat-up time of three minutes is sufficient here, too.

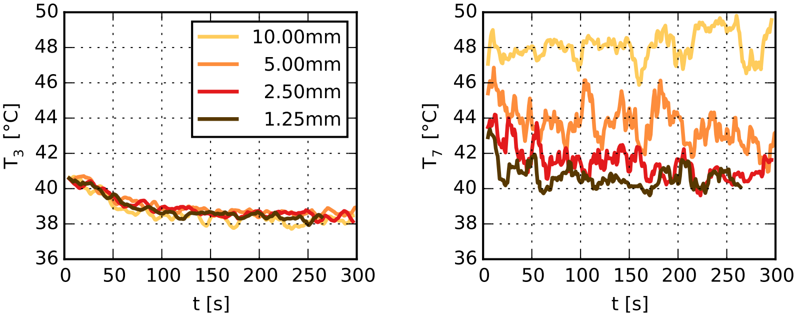

(a) Temperature at T_3.

(b) Temperature at T_7.

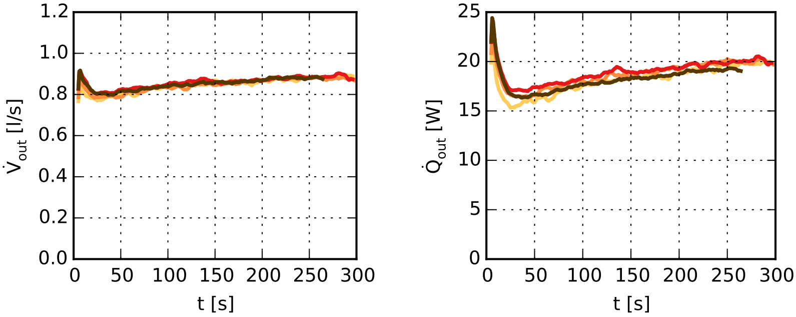

(c) Volume flow out of the door.

(d) Heat flow out of the door.

Figure 4.22: Grid sensitivity study for spill plume simulations with $P_{HS} = 96\,\mathrm{W}$ and $dw = 80\,\mathrm{mm}$. Important simulation results are compared for grid resolutions of 10 mm, 5 mm, 2.5 mm and 1.25 mm. The simulation with 1.25 mm resolution took too long to reach t_{end}, but achieved steady state. All data is smoothed with a moving average over 10 s.

Table 4.2: Compute times for the simulations with $P_{HS} = 96\,\mathrm{W}$ and $t_{end} = 300\,\mathrm{s}$.

Resolution central region	Resolution surrounding	Number of cells	Number of cores	Compute time
10.00 mm	10.00 mm	0.37×10^6	24	0.8 hours
5.00 mm	5.00 mm	2.95×10^6	24	11.0 hours
2.50 mm	2.50 mm	24.04×10^6	24	8.5 days
1.25 mm	1.25 mm	192.28×10^6	96	113.0 days

4.2.2 Execution and evaluation

The analysis of the experiments shows that the ambient temperatures as well as the heat inputs are sufficiently similar between experimental runs using the same power setting to allow for a common comparison with only one simulation. For the simulations, not only the initial temperature stratification inside the enclosure but also the ambient temperatures outside the enclosure is prescribed in accordance with the experimental measurements. As a result, the ambient temperatures can differ among simulations with different heat inputs. A total of eight simulations are required: four simulations per door width, with heat inputs of 29.7 W, 55.5 W, 77.6 W and 96.6 W for a door width of 80 mm and 29.5 W, 55.2 W, 77.5 W and 95.8 W for a door width of 40 mm.

FDSgeogen has been used for setting up the simulations. By doing so, the effort to maintain multiple input files and the possible sources of error when using manual input file generation have been eliminated. Additionally, the automatic evaluation of the simulations is simplified. The computation times given in Table 4.2 originate from the simulations with a door width of 80 mm, a heat input of $P_{HS} = 96\,\mathrm{W}$, and a simulation time of 300 s. Simulations with a resolution of 10 mm to 2.5 mm have been computed on a single node, and the simulation with 1.25 mm resolution has been computed on four nodes in parallel.

The simulation data recorded as FDS slice files has been exported as comma-separated values by *fds2ascii.f90* [14, page 275]. The resulting data can be processed similarly to the experimental data. Due to the increased number of simulations and slice files, this process has been automated for the spill plume simulations. The velocity fields for all heat inputs and door widths, which resulted from the simulation with 2.5 mm resolution, are shown in Figure 4.23 and in Figure 4.24. The overall flow pattern is very similar to the experimental measurements, which have been presented in Figure 4.11 and in Figure 4.12. However, a closer examination reveals differences between the two. The flow velocities are underestimated in the simulations and the centerline follows a stronger horizontal path. A detailed quantitative comparison of experiments and simulations follows in the next section.

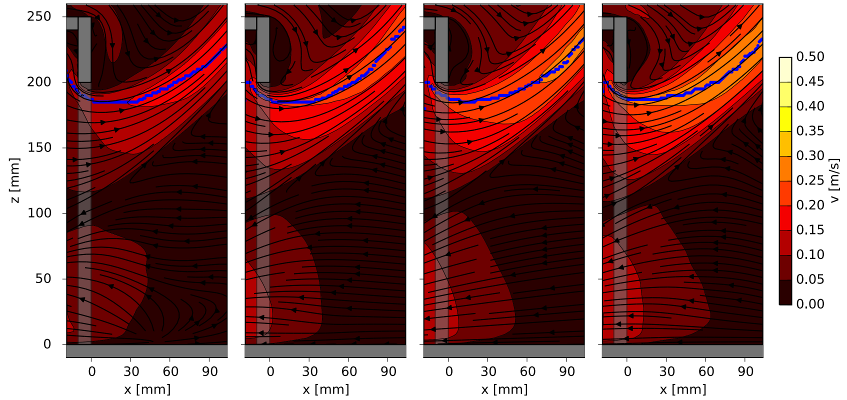

Figure 4.23: Velocity fields in the center of the door with $dw = 80\,\mathrm{mm}$. The results are obtained with a resolution of 2.5 mm and time-averaged over 10 s. From left to right heat inputs of 29.7 W, 55.5 W, 77.8 W and 96.6 W are shown. The blue dots indicate the maximum velocities in the outflow.

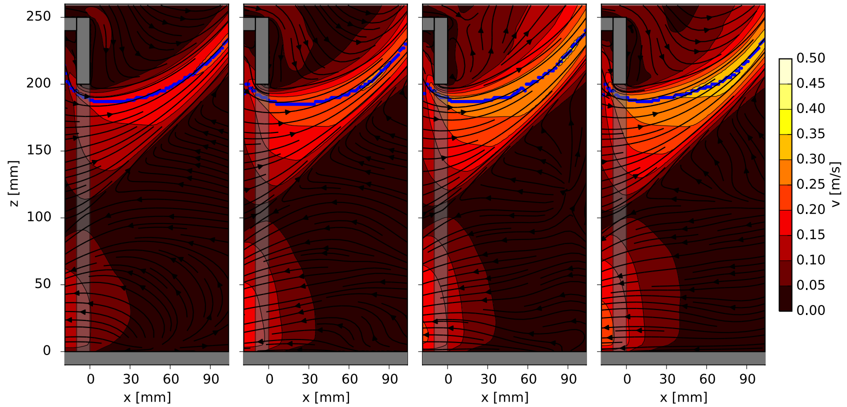

Figure 4.24: Velocity fields in the center of the door with $dw = 40\,\mathrm{mm}$, obtained with a resolution of 2.5 mm and time-averaged over 10 s. From left to right heat inputs of 29.5 W, 55.3 W, 77.5 W and 96.0 W are shown.

4.3 Comparison of experiments and simulations

In the following section, the experimental measurements and the FDS simulations are compared with each other. First the temperature stratification and the simulated centerlines are checked against the experiments. Then the interpolated volume flows in front of the compartment are compared in experiment and simulation. In the final step, the simulation results are used to derive a correction factor for estimating the volume and heat flows out of the opening at $x = 0\,\mathrm{mm}$.

4.3.1 Temperature stratification

The temperature stratification that develops over the course of the experiments and the simulations is compared in Figure 4.25. The upper plots show the recorded temperatures in the enclosure at a height of 110 mm to 590 mm and the lower plots show the temperatures inside the compartment at a height of 40 mm to 200 mm.

The differences are obvious: only those simulations and experimental results that are close to the floor match; above a height of approximately 100 mm to 200 mm, the simulations clearly underestimate the experimental temperatures. At position T_{11}, differences of up to 9 K can be observed, which is about one third of the total temperature rise at that position. Not only do the absolute values differ, but also the shape of the temperature profile in the compartment is different. In the experiments, the steepest temperature gradient is found at a height of 80 mm to 120 mm, whereas the simulations exhibit a strong temperature rise between 40 mm to 80 mm.

4.3.2 Centerlines

The spill plume centerlines have been defined as the maximum absolute velocity in the outflow. In Figure 4.26, the centerlines determined by experiment and simulation are compared. Only the highest and lowest heat input is shown representatively, but for intermediate heat inputs the same trend can be observed: in the simulations, the centerlines and thus the entire spill plume out of the opening are more horizontally oriented than in the experiments. With refined grid resolution, the simulations come closer to the experiments. However, as can be seen in Figure 4.26a, the simulations converge at a resolution of 2.5 mm. Therefore, further refinement does not lead to a better match with the experimental results.

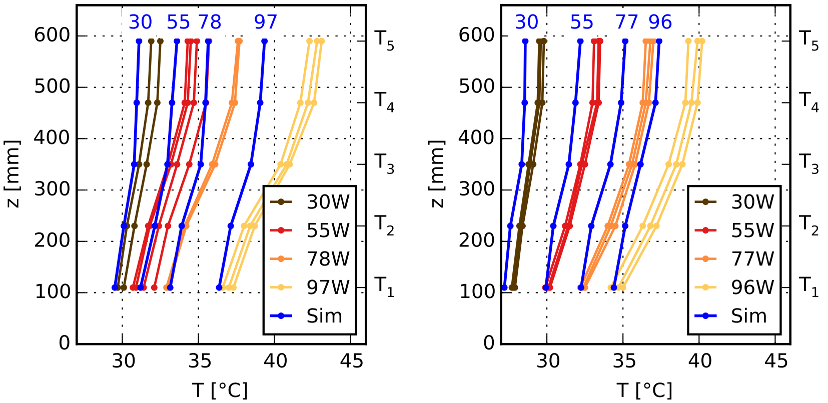

(a) Enclosure
dw = 80 mm

(b) Enclosure
dw = 40 mm

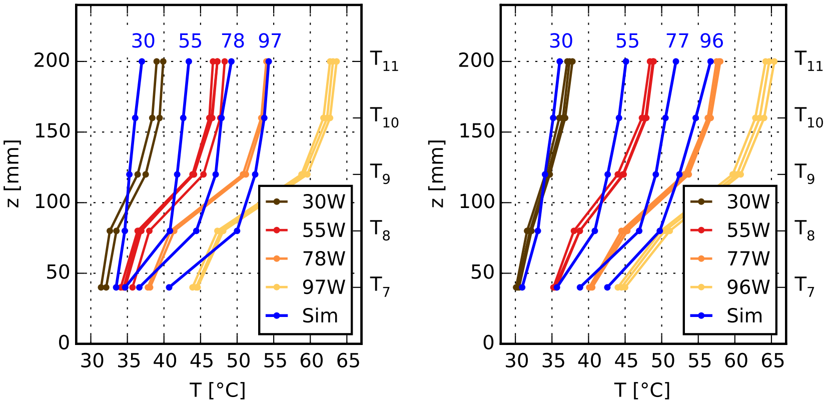

(c) Compartment
dw = 80 mm

(d) Compartment
dw = 40 mm

Figure 4.25: Temperature stratification inside the enclosure and the compartment. The enclosure's interior extends from $z = 0$ mm to $z = 650$ mm, the compartment's interior extends from $z = 0$ mm to $z = 240$ mm. The simulation with 2.5 mm resolution is shown, time-averaged from 180 s to 190 s.

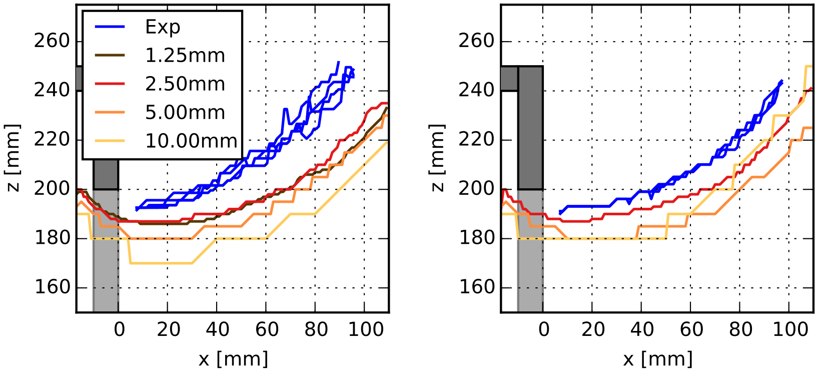

(a) $dw = 80\,\mathrm{mm}$
$P_{HS} = 97\,\mathrm{W}$

(b) $dw = 40\,\mathrm{mm}$
$P_{HS} = 96\,\mathrm{W}$

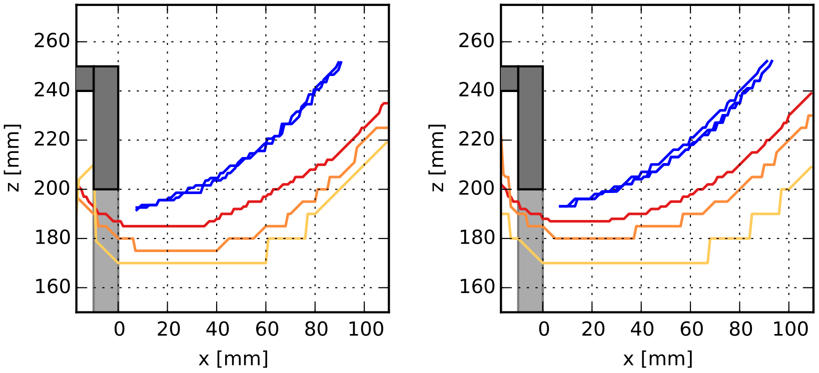

(c) $dw = 80\,\mathrm{mm}$
$P_{HS} = 30\,\mathrm{W}$

(d) $dw = 40\,\mathrm{mm}$
$P_{HS} = 30\,\mathrm{W}$

Figure 4.26: Comparison of centerlines for different heat inputs.

As representatives for all door widths and heat inputs, the centerlines at $P_{HS} = 97\,\mathrm{W}$ with a door width of $dw = 80\,\mathrm{mm}$ are analyzed in more detail in Figure 4.27. In Subfigure 4.27a, the absolute velocity v along the centerline as a function of x is shown. It is apparent that simulations clearly underestimate the velocities in the outflow. While there are velocities of 0.36 m/s to 0.41 m/s in the experiments, the simulations exhibit values of only 0.24 m/s to 0.28 m/s. This is a deviation of about one third, which is also typical for experiments at other heat inputs and door widths. What is notable is that the deviation is constant along the centerline.

A closer look at the horizontal and vertical velocity component v_x and v_z alone reveals a different picture. As can be seen in Figure 4.27c and in Figure 4.27d, the horizontal velocity v_x deviates stronger in close range of the opening, whereas v_z shows a greater deviation further along the centerline. The deceleration in the horizontal direction and the acceleration in the vertical direction are stronger in the experiments than in the simulations. The ratio of v_z to v_x, which is shown in Figure 4.27b, illustrates the gradient angle of the centerlines. Right from the start, the experiments have a larger gradient angle than the simulations, and it increases further along the centerline.

4.3.3 Volume flow in front of the opening

Analogous to the reduced centerline velocities, the volume flows are also smaller in the simulations than in the experiments. In Figure 4.28 both the inflows and outflows at a 10 mm distance to the opening are compared for both door widths. It should be noted that in the simulations the inflow is close to the experimental results, while the outflow differs significantly between experiment and simulation. On average, the outflow in the simulations is approximately 20 % to 25 % lower than in the experiments.

All these observations – higher gas temperatures in the hot upper layers, a higher exit velocity at the opening, and a stronger vertical acceleration along the centerline, resulting in a larger outflow out of the door – may possibly be explained, if the convective heat input in the experiments was higher than in the simulations. As already stated, during the experiments only the total heat input has been directly measured. The convective, radiative and conductive fraction of the total heat input are determined in the simulations, based on the measured emissivity and the flow pattern that develops around the heat source. If the resulting convective fraction, which is the only direct driver of the flow, is too low in the simulations, then lower gas temperatures might lead to different characteristics of the outflow. However, when comparing the centerlines from the simulations at $P_{HS} = 97\,\mathrm{W}$ (Figure 4.26a)

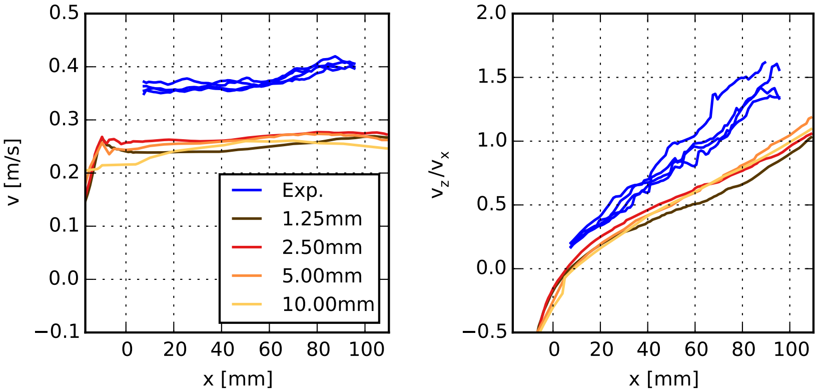

(a) $v(x)$ (b) $v_z/v_x(x)$

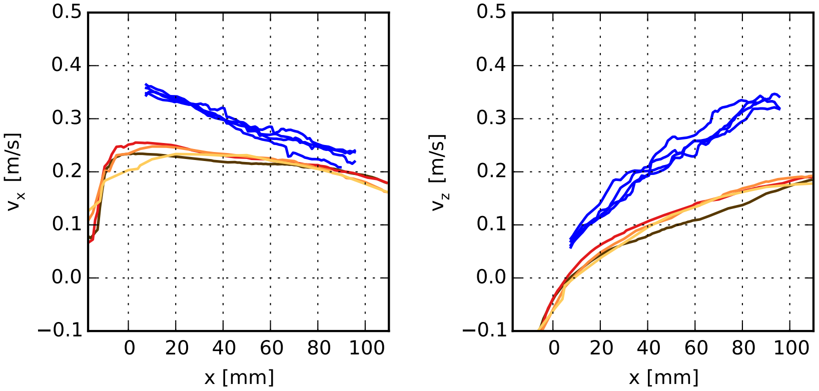

(c) $v_x(x)$ (d) $v_z(x)$

Figure 4.27: Analysis of centerlines at $P_{HS} = 97\,\mathrm{W}$ and $dw = 80\,\mathrm{mm}$.

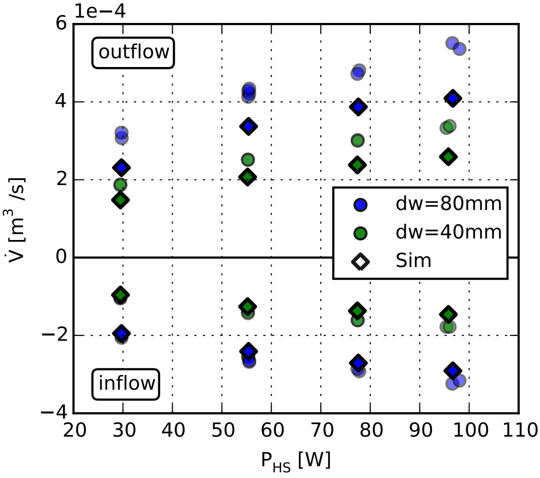

Figure 4.28: Overview of volume flows in experiments (circles) and simulations (diamonds) for both door widths. Values are given for the half cross-section of the door at position $x = 10\,\mathrm{mm}$.

with the centerlines from the experiments at $P_{HS} = 30\,\mathrm{W}$ (Figure 4.26c), it becomes clear that even a greatly increased heat input in the simulations does not lead to centerlines as steep as in the experiments.

Therefore, further experiments are required in order to determine the convective fraction more precisely and reduce the radiative heat flux as far as possible. It would also be advantageous to measure gas temperatures at various positions in the outflow for being able to determine the heat flow out of the compartment.

4.3.4 Heat flow out of the compartment

For now, the available experimental data will be used to estimate the heat flow out of the compartment. Fortunately the simulation data, which is (in comparison) easily available, allows the development and testing of this method so that its accuracy can be evaluated. For the determination of the net heat flow through the opening, the volume flow out of the opening and the temperatures of inflow and outflow are required. To determine the former, a correction factor is derived that allows the estimation of the outflow inside the opening ($x = 0\,\mathrm{mm}$) based on the measurements in front of the opening

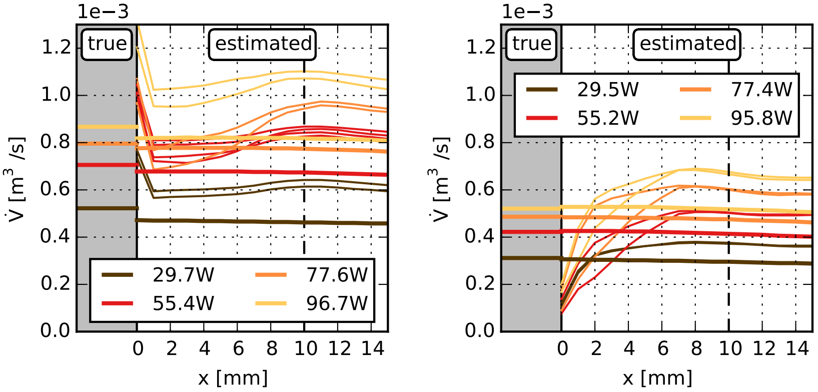

(a) Door width: 80 mm (b) Door width: 40 mm

Figure 4.29: Outflow in front of the opening as a function of x. Thick lines originate from the simulations, thin lines from the experiments. For $x > 10$ mm the experimental measurements are considered reliable (dashed line). Note: Values are given for complete cross section of the opening.

($x = 10$ mm). It can be concluded from the simulations that the averaged inflow and outflow temperatures are best resembled by the measurement positions T_1 and T_9.

Correction factor for volume flows

In Figure 4.29 the volume flows, as a function of the distance to the opening, are shown. The thick lines originate from the simulations with a resolution of 2.5 mm and are used as a reference here. In the left part of each plot a gray-shaded area shows the 'true' values obtained from the simulations. These 'true' values have been determined by a slice file that spans the entire opening and captures outflow with high precision. Such a measurement has not been possible in the experiments. In the right part of every plot, the estimated volume flow is shown as a function of x. These volume flows are – both for simulation and experiment – calculated based on the interpolation method described on page 105 and illustrated in Figure 4.17. For this method the area of the door is projected in front of the opening and only the flow through this area is considered. Because intermediate values between data points are linearly interpolated, the interpolation method does not necessarily yield the true volume flow at $x = 0$ mm.

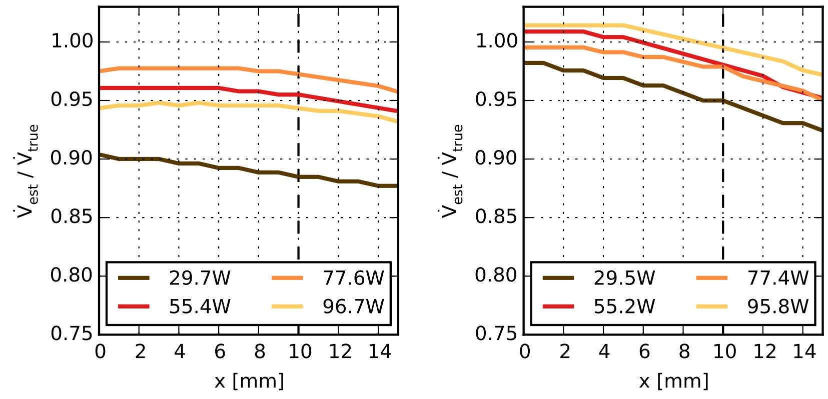

(a) Door width: 80 mm

(b) Door width: 40 mm

Figure 4.30: Ratio of estimated to true volume flows as derived from the simulations with a resolution of 2.5 mm. In the following referred to as correction factor, CF.

There are two main conclusions that can be drawn from this figure. First, for the available experimental data, a distance of approximately 10 mm to the opening is indeed necessary to obtain reasonable measurements. For $x < 10$ mm, unphysical behavior (decreasing volume flow despite the narrowing of the flow) can be observed, which is probably caused by erroneous measurements due to the illuminated doorjamb in the background. On page 103 a more detailed explanation is given. Second, for $x > 10$ mm, the curves from experiments and simulations run almost parallel. Thus, although experiment and simulation do not agree in absolute numbers, it can be assumed that they exhibit a similar relation between estimated volume flow in front the opening and true volume flow inside the opening. It seems therefore valid, to derive a correction factor from the simulations to be used for the experiments. In the experiments the estimated volume flows exhibit a slightly stronger decrease with increasing distance to the opening (for $x > 10$ mm). This means that a correction factor derived on the basis of the simulations can be applied for the experiments, but the true outflows in the experiments will probably be slightly underestimated when using this correction factor.

In order to derive the correction factor, the ratio of the estimated volume flow $\dot{V}_{est}$ to true volume flow $\dot{V}_{true}$ is plotted as a function of x in Figure 4.30. This can, of course, only be done on the basis of the simulations, because only for them is the true value known. From this figure the correction factors can be read off directly. For example, the true outflow through the opening at dw = 40 mm and $P_{HS} = 29.5\,\mathrm{W}$ is obtained by dividing the outflow at $x = 10\,\mathrm{mm}$ by a correction factor of 0.95.

Estimate of heat flows out of the opening

In order to determine the heat flow, the volume flow has to be converted into a mass flow. Therefore, the ideal gas law (Equation 4.1) can be used because, under the conditions of the experiments, air can be considered an ideal gas.

$$p \cdot V = m \cdot R_s \cdot T \tag{4.1}$$

By using the previously derived correction factor, CF, the mass flow in the experiments is determined by

$$\dot{m}_{out}^{0mm} = \frac{p}{R_s \cdot T_9} \cdot \frac{\dot{V}_{out}^{10mm}}{CF} \tag{4.2}$$

The convective net heat flow out of the opening is calculated by

$$\dot{Q} = \dot{m} \cdot c_p \cdot \Delta T \tag{4.3}$$

Substituting the mass flow and adapting the equation for the experiments described here, it follows

$$\dot{Q}_{out}^{0mm} = \frac{p}{R_s \cdot T_9} \cdot \frac{\dot{V}_{out}^{10mm}}{CF} \cdot c_p \cdot (T_9 - T_1) \tag{4.4}$$

with

R_s : specific gas constant, $287.058\,\mathrm{J\,kg^{-1}\,K^{-1}}$
T_1, T_9 : assumed inflow and outflow temperatures in K
CF : correction factor derived from the simulations, $\dot{V}_{est}^{10mm}/\dot{V}_{true}$
c_p : specific heat capacity (isobaric), $1005\,\mathrm{J\,kg^{-1}\,K^{-1}}$

From the simulations it can be concluded that the measurement positions T_1 and T_9 best resemble the inflow and outflow temperatures. In Table 4.3 and Table 4.4, the heat flow calculations based on Equation 4.2 and Equation 4.4 are shown. In order to assess the accuracy of the applied method, the simulation data can be used as a reference, by comparing the estimated heat flow value $\dot{Q}_{out}^{0mm}$ to the true heat flow value $\dot{Q}_{out}^{true}$. Both values agree very well for all simulation setups; the deviation is never more than 10 % and for most simulations it is less than 5 %. However, it should be noted that the correction factor was derived on the basis on the simulations, so the volume flow estimation inside the opening will inevitably yield correct results for the simulations. For the experiments, there is an additional uncertainty in this regard.

When comparing the heat flow $\dot{Q}_{out}^{0mm}$ to the total heat input P_{HS}, it is striking that only a small portion of the heat is convectively transferred through the opening. For a door width of 80 mm this portion is about 19 % to 28 % in the experiments and 10 % to 15 % in the simulations. For the narrower door, the convective fraction is even smaller: about 10 % to 19 % in the experiments and 8 % to 11 % in the simulations. Thermal radiation cannot penetrate the compartment walls, as was shown on page 52. Also, the area of the door is very small compared to that of the compartment walls, floor and ceiling ($< 3.5\,\%$), so that radiation cannot account for a major part of the overall heat flow out of the compartment. This means that most of the energy has to be transferred via conduction through the compartment walls, ceiling and floor, which are heated via convection and radiation from the inside.

The comparison of heat flows determined by experiment and simulation reveals huge differences. Although the volume flows of experiment and simulation are only 20 % to 25 % off, the heat flows in the simulations deviate by up to 45 % from the experimental values. This is due to higher gas temperatures in the experimental outflows, which further increase the amount of energy transferred. As was shown in Figure 4.29, the outflow in the experiments is likely to be slightly underestimated by the correction factor, because the experimental outflow exhibits a stronger dependency on the distance for $10\,\text{mm} < x < 15\,\text{mm}$ than the outflow in the simulations. Therefore, the heat flow is also likely to be slightly underestimated in the experiments, which would further increase the discrepancy between simulations and experiments.

Based on these findings, the different outflow velocities and positions in experiment and simulation are now better understandable. Although the different convective heat flows out of the opening are most likely not the only reason for the different outflow characteristics – otherwise the outflows of high energy simulations and low energy experiments should look more similar – it is self-evident that identical boundary conditions in experiment and simulation must be guaranteed for a valid comparison of both. Therefore, the next logical step would be to modify and repeat the experiments in order to make sure that the experimental boundary conditions are determined with the highest possible accuracy. This includes a reduction of the heat source's emissivity to a minimum, in order to reduce the radiative fraction of the heat source. In this way, almost the entire energy would be emitted convectively

Table 4.3: Calculation of heat flows for $dw = 80\,\text{mm}$.

P_{HS} W		T_1 °C	T_9 °C	$\dot{V}_{out}^{10mm}$ m^3/s	CF	$\dot{V}_{out}^{0mm}$ m^3/s	$\dot{m}_{out}^{0mm}$ kg/s	$\dot{Q}_{out}^{0mm}$ W	$\dot{Q}_{out}^{true}$ W
				$\times 10^{-4}$		$\times 10^{-4}$	$\times 10^{-4}$		
29.7	Exp	29.9	36.9	6.28	0.885	7.10	7.97	5.6	–
	Sim	29.5	35.3	4.62		5.22	5.90	3.4	3.1
55.4	Exp	31.3	44.3	8.48	0.955	8.88	9.74	12.7	–
	Sim	31.2	41.8	6.74		7.06	7.81	8.3	7.9
77.6	Exp	32.9	51.0	9.53	0.972	9.80	10.54	19.2	–
	Sim	33.1	47.1	7.74		7.96	8.66	12.2	11.4
96.7	Exp	36.9	59.2	10.87	0.943	11.53	12.08	27.1	–
	Sim	36.4	52.5	8.18		8.67	9.28	15.0	14.3

Table 4.4: Calculation of heat flows for $dw = 40\,\text{mm}$.

P_{HS} W		T_1 °C	T_9 °C	$\dot{V}_{out}^{10mm}$ m^3/s	CF	$\dot{V}_{out}^{0mm}$ m^3/s	$\dot{m}_{out}^{0mm}$ kg/s	$\dot{Q}_{out}^{0mm}$ W	$\dot{Q}_{out}^{true}$ W
				$\times 10^{-4}$		$\times 10^{-4}$	$\times 10^{-4}$		
29.5	Exp	27.8	34.4	3.74	0.950	3.94	4.46	3.0	–
	Sim	27.2	34.1	2.96		3.12	3.53	2.4	2.5
55.2	Exp	30.1	44.5	5.03	0.980	5.13	5.63	8.1	–
	Sim	29.9	42.6	4.14		4.22	4.66	5.9	5.8
77.4	Exp	32.4	53.4	6.02	0.979	6.15	6.56	13.8	–
	Sim	32.2	49.2	4.76		4.86	5.25	9.0	8.6
95.8	Exp	34.6	60.3	6.71	0.995	6.74	7.05	18.2	–
	Sim	34.4	52.4	5.18		5.21	5.57	10.1	10.4

by the heat source, so that the convective heat flow could be precisely measured by measuring the total electric power consumption of the heat source. In addition to that, a greater number of temperature measurements should be taken, both directly in the inflow and outflow as well as inside and on the surface of the compartment walls. Once these additional measurements are obtained, the convective, conductive and radiative heat flow could be determined with greater precision and the comparison of experiments and simulations should be repeated, possibly followed by an in-depth investigation of the remaining differences, if necessary. At the moment, the available experimental data is not sufficient to further investigate and explain the deviations between experiments and simulations.

Chapter 5

Conclusions

The aim of this study was to design and carry out bench-scale laboratory experiments specifically designed for the validation of fire models, and to use the experimental data for a validation study of the Fire Dynamics Simulator (FDS). The focus of the experiments was on one of the key components of fire models, the modeling of buoyancy-driven flows. The experimental setup was simplified by neglecting pyrolysis and combustion, and its objective was to achieve high precision and reproducibility. Therefore, an electrically heated block of copper (60 mm × 60 mm × 40 mm) was used as a heat source and particle image velocimetry was applied for measuring the flow velocities in the experiments. Two different setups were investigated: an undisturbed buoyant plume above the heat source (open plume) and a buoyant spill plume emerging from a compartment with one opening. For both setups, an enclosure made of acrylic glass (735 mm × 575 mm × 650 mm) constituted the experimental domain.

For the open plume setup, experiments with heat inputs from 30 W to 96 W were carried out, which led to heat source temperatures of 150 °C to 305 °C. The resulting flow was laminar for the lowest power setting and underwent a transition to turbulent flow for higher heat inputs. With increasing heat input, the point of transition from laminar to turbulent flow occurred at lower heights. An investigation of the vertical velocity and the scattering of the horizontal velocity along the plume centerline, and as a function of the Grashof number, was presented, in order to localize the point of transition. It was shown that the transition from laminar to turbulent flow occurs at Grashof numbers in the range of $4 \times 10^8 < Gr < 2 \times 10^9$. These values are in good agreement with previous studies. For the validation study, the transition to turbulent flow was used for the comparison of experiment and simulation, along with further flow characteristics such as maximum velocities in the plume, plume widths and flow integrals. The FDS simulations generally showed a good agreement with the experiments, provided that a sufficiently fine grid resolution of no more than 2.5 mm was used.

The spill plume experiments were carried out by positioning the same heat source inside a compartment (300 mm × 300 mm × 240 mm) that had a door as its only opening. For a variation of the scenario, two different door widths were investigated. Velocity fields were measured in various positions in front of the door so that both inflow and outflow were recorded. Flow characteristics compared in this scenario included the position and velocity of the spill plume centerline and the volume flows in front of the opening. The heat flow inside the opening could not be measured directly, therefore, an estimation method was developed based on the available data. When comparing experimental and simulation results, significant differences became apparent, both in terms of centerline characteristics and volume flows in front of the opening. In the simulations, the centerlines were more horizontally oriented and they exhibited lower absolute velocities than in the experiments. As a result, the volume flows in front of the opening were also underestimated by approximately 20 % to 25 % in the simulations. Using the heat flow estimation method, it could be shown that the convective heat flows out of the opening were also significantly lower in the simulations than in the experiments. The maximum observed deviation was almost 45 %, which is likely to be one, but not the only, reason for different centerline characteristics and volume flows. Why, however, the heat flows deviate so significantly, could not be explained using the available data.

For future experiments, a number of potential improvements have been identified. An important modification of both experimental setups would be, to reduce the emissivity of the heat source and therefore the radiative fraction as far as possible. In the experiments in this thesis, only a minor part of the overall energy input was convectively released by the heat source; the major part was radiatively transferred to the surrounding walls. Although this was considered in the simulations, it would be beneficial if the maximum possible proportion of the total heat input would be convectively emitted. The convective fraction could then be more precisely determined by measuring the total heat input. Furthermore, temperature measurements inside the plume and in various positions inside the compartment walls would help to make a more reliable estimate of the convective and conductive heat flows. Another advisable modification relates to the heating coil of the heat source. For future experiments, it should be inserted from underneath, to eliminate any disturbance of the flow.

Particle image velocimetry proved to be very well suited for these kinds of experiment, although it has rarely been used in fire safety engineering to date. The great technical effort is justified by the high resolution in space and time, the ability to measure the velocity in an entire plane with high accuracy, and the fact that the flow under investigation remains undisturbed. In future experiments, stereo PIV could be applied in order to further investigate the hollow or double plume structure, which has been observed in some of the open plume experiments. For the spill plume experiments, measurements with stereo PIV would allow the capture of the entire opening at once and the determination of the inflow and outflow without interpolation and thus with higher precision.

The investigations in this thesis, along with the number of possible improvements, lead to the conclusion: Although both scenarios are simplified, they are far from simple. There is still great potential for future research. Therefore, the author welcomes the fact that his work is already being continued. These and similar experiments in the future will further contribute to the development of fire models and will help to make them even more reliable tools for fire safety engineering.

Bibliography

[1] A. H. Buchanan, “Fire engineering for a performance based code,” *Fire Safety Journal*, vol. 23, no. 1, pp. 1–16, 1994. (Cited on page 1)

[2] B. J. Meacham, “The evolution of performance-based codes and fire safety design methods,” Tech. Rep. NIST-GCR-98-761, National Institute of Standards and Technology, Bethesda, Nov. 1998. (Cited on page 1)

[3] B. Meacham, R. Bowen, J. Traw, and A. Moore, “Performance-based building regulation: Current situation and future needs,” *Building Research & Information*, vol. 33, pp. 91–106, Mar. 2005. (Cited on page 1)

[4] L. A. Gritzo, P. E. Senseny, Y. Xin, and J. Russell Thomas, “The international FORUM of fire research directors: A position paper on verification and validation of numerical fire models,” *Fire Safety Journal*, vol. 40, pp. 485–490, July 2005. (Cited on pages 1 and 12)

[5] P. A. Croce, W. L. Grosshandler, R. W. Bukowski, and L. A. Gritzo, “The International FORUM of Fire Research Directors: A position paper on performance-based design for fire code applications,” *Fire Safety Journal*, vol. 43, pp. 234–236, Apr. 2008. (Cited on page 1)

[6] Y. Wang, I. Burgess, F. Wald, and M. Gillie, *Performance-Based Fire Engineering of Structures*. CRC Press, June 2012. (Cited on page 1)

[7] A. Alvarez, B. Meacham, N. Dembsey, and J. Thomas, “Twenty years of performance-based fire protection design: Challenges faced and a look ahead,” *Journal of Fire Protection Engineering*, vol. 23, pp. 249–276, Nov. 2013. (Cited on page 1)

[8] D. Hosser, “Leitfaden Ingenieurmethoden des Brandschutzes,” tech. rep., vfdb, Altenberge, Nov. 2013. (Cited on pages 1 and 6)

[9] C. Fleischmann, “Is Prescription the Future of Performance Based Design?,” *Fire Safety Science*, vol. 10, pp. 77–94, 2011. (Cited on page 1)

[10] B. J. Meacham, “Fire safety engineering at a crossroad,” *Case Studies in Fire Safety*, vol. 1, pp. 8–12, Mar. 2014. (Cited on pages 1 and 2)

[11] D. Geer, “Chip makers turn to multi-core processors,” *Computer*, vol. 38(5), no. 5, pp. 11 – 13, 2005. (Cited on pages 2 and 11)

[12] D. C. Brock and G. E. Moore, eds., *Understanding Moore’s Law: Four Decades of Innovation*. Philadelphia, Pa: Chemical Heritage Foundation, 2006. (Cited on page 2)

[13] S. Hostikka, *Development of Fire Simulation Models for Radiative Heat Transfer and Probabilistic Risk Assessment*. PhD thesis, VTT Technical Research Centre of Finland, Helsinki, 2008. (Cited on page 2)

[14] K. McGrattan, S. Hostikka, R. McDermott, J. Floyd, C. Weinschenk, and K. Overholt, *Fire Dynamics Simulator 6.3.2 User ’s Guide*. National Institute of Standards and Technology, Building and Fire Research Laboratory, Nov. 2015. (Cited on pages 2, 8, 9, 10, 11, 67, 68, 73, and 113)

[15] K. McGrattan, S. Hostikka, R. McDermott, J. Floyd, C. Weinschenk, and K. Overholt, *Fire Dynamics Simulator 6.3.2 Technical Reference Guide Volume 3: Validation*. National Institute of Standards and Technology, Building and Fire Research Laboratory, Nov. 2015. (Cited on pages 2, 9, 13, and 70)

[16] P. van Hees, “Validation and Verification of Fire Models for Fire Safety Engineering,” *Procedia Engineering*, vol. 62, pp. 154–168, 2013. (Cited on pages 2 and 12)

[17] M. Raffel, ed., *Particle Image Velocimetry: A Practical Guide*. Heidelberg; New York: Springer, 2nd ed ed., 2007. (Cited on pages 3, 13, 17, 18, 19, 20, 21, 22, 23, 24, and 26)

[18] ARGEBAU, “Musterbauordnung MBO - Fassung November 2002,” Sept. 2012. (Cited on page 5)

[19] VDI, *VDI Richtlinie 6019 - Blatt 1 - Ingenieurverfahren Zur Bemessung Der Rauchableitung Aus Gebäuden*. 2006. (Cited on page 6)

[20] VDI, *VDI Richtlinie 6019 - Blatt 2 - Ingenieurverfahren Zur Bemessung Der Rauchableitung Aus Gebäuden*. 2009. (Cited on page 6)

[21] E. E. Zukoski, T. Kubota, and B. Cetegen, “Entrainment in fire plumes,” *Fire Safety Journal*, vol. 3, pp. 107–121, Feb. 1981. (Cited on page 7)

[22] B. J. McCaffrey, “Momentum implications for buoyant diffusion flames,” *Combustion and Flame*, vol. 52, pp. 149–167, Jan. 1983. (Cited on page 7)

[23] G. Heskestad, “Virtual origins of fire plumes,” *Fire Safety Journal*, vol. 5, pp. 109–114, Jan. 1983. (Cited on page 7)

[24] G. Heskestad, “Engineering relations for fire plumes,” *Fire Safety Journal*, vol. 7, pp. 25–32, Jan. 1984. (Cited on page 7)

[25] R. D. Peacock, P. A. Reneke, and G. P. Forney, “CFAST –Consolidated Model of Fire Growth and Smoke Transport (Version 7) Volume 2: User’s Guide,” Tech. Rep. NIST TN 1889v2, National Institute of Standards and Technology, Dec. 2015. (Cited on page 7)

[26] C. Wade, G. Baker, K. Frank, A. Robbins, R. Harrison, M. Spearpoint, and C. Fleischmann, “B-RISK User Guide and Technical Manual,” Tech. Rep. SR 282, BRANZ Ltd., Porirua City, 2013. (Cited on page 7)

[27] H. K. Versteeg and W. Malalasekera, *An Introduction to Computational Fluid Dynamics: The Finite Volume Method.* Pearson Education, 2007. (Cited on pages 8 and 9)

[28] T. J. Chung, *Computational Fluid Dynamics.* Cambridge University Press, Sept. 2010. (Cited on pages 8 and 9)

[29] J. F. Wendt, J. D. Anderson, and Von Karman Institute for Fluid Dynamics, eds., *Computational Fluid Dynamics: An Introduction.* Berlin: Springer, 3rd ed ed., 2008. (Cited on pages 8 and 9)

[30] H. G. Weller, G. Tabor, H. Jasak, and C. Fureby, “A tensorial approach to computational continuum mechanics using object-oriented techniques,” *Computers in Physics*, vol. 12, pp. 620–631, Nov. 1998. (Cited on page 8)

[31] G. P. Forney, *Smokeview 6.3.2, A Tool for Visualizing Fire Dynamics Simulation Data Volume I: User’s Guide.* National Institute of Standards and Technology, Building and Fire Research Laboratory, Apr. 2015. (Cited on page 8)

[32] FDS Usergroup, "FDS Leitfaden 1.0.0," Nov. 2015. (Cited on page 9)

[33] "FDS and Smokeview Discussions - Google Groups." `https://groups.google.com/forum/?fromgroups#!forum/fds-smv`. (Cited on page 9)

[34] FDS Usergroup, "Shareideas." `http://www.shareideas.de/`. (Cited on page 9)

[35] K. McGrattan, S. Hostikka, R. McDermott, J. Floyd, C. Weinschenk, and K. Overholt, *Fire Dynamics Simulator 6.3.2 Technical Reference Guide Volume 4: Configuration Management.* National Institute of Standards and Technology, Building and Fire Research Laboratory, Nov. 2015. (Cited on page 9)

[36] K. McGrattan, S. Hostikka, R. McDermott, J. Floyd, C. Weinschenk, and K. Overholt, *Fire Dynamics Simulator 6.3.2 Technical Reference Guide Volume 1: Mathematical Model.* National Institute of Standards and Technology, Building and Fire Research Laboratory, Nov. 2015. (Cited on page 9)

[37] K. McGrattan, S. Hostikka, R. McDermott, J. Floyd, C. Weinschenk, and K. Overholt, *Fire Dynamics Simulator 6.3.2 Technical Reference Guide Volume 2: Verification.* National Institute of Standards and Technology, Building and Fire Research Laboratory, Nov. 2015. (Cited on page 9)

[38] G. H. Yeoh and K. K. Yuen, *Computational Fluid Dynamics in Fire Engineering.* 2009. (Cited on page 9)

[39] M. J. Hurley, D. T. Gottuk, J. R. Hall, K. Harada, E. D. Kuligowski, M. Puchovsky, J. L. Torero, J. M. Watts, and C. J. Wieczorek, eds., *SFPE Handbook of Fire Protection Engineering.* New York, NY: Springer New York, 2016. (Cited on page 9)

[40] D. Drysdale, *An Introduction to Fire Dynamics.* Chichester, UK: John Wiley & Sons, Ltd, Aug. 2011. (Cited on page 9)

[41] J. G. Quintiere, *Fundamentals of Fire Phenomena.* Chichester, UK: John Wiley & Sons, Ltd, Mar. 2006. (Cited on page 9)

[42] B. Karlsson and J. Quintiere, *Enclosure Fire Dynamics.* CRC Press, Sept. 1999. (Cited on page 9)

[43] J. W. Deardorff, "Stratocumulus-capped mixed layers derived from a three-dimensional model," *Boundary-Layer Meteorology*, vol. 18, pp. 495–527, June 1980. (Cited on page 10)

[44] D. Haarhoff and L. Arnold, "Performance Analysis and Shared Memory Parallelization of FDS," (Gaithersburg), 09/08/14. (Cited on pages 11 and 12)

[45] D. Haarhoff, "Hybrid Parallelisation of the CFD-software FDS," 2014. (Cited on page 12)

[46] K. Steckler, J. Quintiere, and W. Rinkinen, "Flow induced by fire in a compartment," Tech. Rep. NBSIR 82-2520, U.S. Department of Commerce, National Bureau of Standards, Washington, DC, Sept. 1982. (Cited on pages 12 and 90)

[47] T. J. O'Hern, E. J. Weckman, A. L. Gerhart, S. R. Tieszen, and R. W. Schefer, "Experimental study of a turbulent buoyant helium plume," *Journal of Fluid Mechanics*, vol. 544, p. 143, Nov. 2005. (Cited on page 13)

[48] R. A. Bryant, "A comparison of gas velocity measurements in a full-scale enclosure fire," *Fire Safety Journal*, vol. 44, pp. 793–800, July 2009. (Cited on pages 13 and 14)

[49] R. A. Bryant, "The application of stereoscopic PIV to measure the flow of air into an enclosure containing a fire," *Experiments in Fluids*, vol. 47, pp. 295–308, Aug. 2009. (Cited on pages 13, 14, and 104)

[50] R. A. Bryant, "Evaluating practical measurements of fire-induced vent flows with stereoscopic PIV," *Proceedings of the Combustion Institute*, vol. 33, no. 2, pp. 2481–2487, 2011. (Cited on pages 13 and 14)

[51] R. D. Keane and R. J. Adrian, "Optimization of particle image velocimeters. I. Double pulsed systems," *Measurement Science and Technology*, vol. 1, p. 1202, Nov. 1990. (Cited on pages 13 and 23)

[52] R. D. Keane and R. J. Adrian, "Theory of cross-correlation analysis of PIV images," *Applied Scientific Research*, vol. 49, pp. 191–215, July 1992. (Cited on pages 13 and 23)

[53] T. Persoons and T. S. O'Donovan, "High Dynamic Velocity Range Particle Image Velocimetry Using Multiple Pulse Separation Imaging," *Sensors (Basel, Switzerland)*, vol. 11, pp. 1–18, Dec. 2010. (Cited on page 13)

[54] X. C. Zhou and J. P. Gore, “Study of Entrainment and Flow Patterns in Pool Fires Using Particle Imaging Velocimetry,” Tech. Rep. NIST GCR 97-706, Mar. 1996. (Cited on page 13)

[55] G. Papadopoulos, R. Bryant, and W. Pitts, “Flow characterization of flickering methane/air diffusion flames using particle image velocimetry,” *Experiments in Fluids*, vol. 33, pp. 472–481, Sept. 2002. (Cited on page 13)

[56] S. Funatani, N. Fujisawa, and H. Ikeda, “Simultaneous measurement of temperature and velocity using two-colour LIF combined with PIV with a colour CCD camera and its application to the turbulent buoyant plume,” *Measurement Science and Technology*, vol. 15, no. 5, p. 983, 2004. (Cited on page 13)

[57] X. Zhou, L. Sun, S. Mahalingam, and D. R. Weise, “Thermal particle image velocity estimation of fire plume flow,” *Combustion Science and Technology*, vol. 175, pp. 1293–1316, July 2003. (Cited on page 13)

[58] L. Sun, X. Zhou, S. M. Mahalingam, and D. R. Weise, “Experimental investigation of the velocity field in buoyant diffusion flames using PIV and TPIV algorithm,” 2005. (Cited on page 13)

[59] B. P. Husted, *Experimental Measurements of Water Mist Systems and Implications for Modelling in CFD*. PhD thesis, Lund University, Lund, 2007. (Cited on page 14)

[60] B. P. Husted, P. Petersson, I. Lund, and G. Holmstedt, “Comparison of PIV and PDA droplet velocity measurement techniques on two high-pressure water mist nozzles,” *Fire Safety Journal*, vol. 44, pp. 1030–1045, Nov. 2009. (Cited on page 14)

[61] Y. Shoshin, G. Gorecki, J. Jarosinski, and T. Fodemski, “Experimental study of limit lean methane/air flame in a standard flammability tube using particle image velocimetry method,” *Combustion and Flame*, vol. 157, pp. 884–892, May 2010. (Cited on page 14)

[62] F. Morandini, X. Silvani, and A. Susset, “Feasibility of particle image velocimetry in vegetative fire spread experiments,” *Experiments in Fluids*, vol. 53, pp. 237–244, Mar. 2012. (Cited on page 14)

[63] F. Morandini, X. Silvani, D. Honoré, G. Boutin, A. Susset, and R. Vernet, “Slope effects on the fluid dynamics of a fire spreading across a

fuel bed: PIV measurements and OH* chemiluminescence imaging," *Experiments in Fluids*, vol. 55, pp. 1–12, July 2014. (Cited on page 14)

[64] R. A. Bryant, "Particle Image Velocimetry Measurements of Buoyancy Induced Flow Through a Doorway," Tech. Rep. NISTIR 7252, National Institute of Standards and Technology, Sept. 2005. (Cited on pages 14 and 18)

[65] S. Suard, A. Koched, H. Pretrel, and L. Audouin, "Numerical simulations of fire-induced doorway flows in a small scale enclosure," *International Journal of Heat and Mass Transfer*, vol. 81, pp. 578–590, Feb. 2015. (Cited on page 14)

[66] S. Suard, C. Lapuerta, F. Babik, and L. Rigollet, "Verification and validation of a CFD model for simulations of large-scale compartment fires," *Nuclear Engineering and Design*, vol. 241, pp. 3645–3657, Sept. 2011. (Cited on page 14)

[67] B. Schröder, L. Arnold, S. Schmidt, M. Brüne, and A. Meunders, "High parametric CFD-analysis of fire scenarios in underground train stations using statistical methods and climate modelling," in *Proceedings*, (Australia), Society of Fire Protection Engineers (SFPE), 2014. (Cited on page 15)

[68] Thunderhead Engineering, *PyroSim User Manual*. 2014. (Cited on page 15)

[69] L. Arnold, A. Meunders, B. Schröder, and J. Boltersdorf, "FDS-geogen," Mar. 2015. (Cited on page 15)

[70] L. Arnold, J. Boltersdorf, A. Meunders, and B. Schröder, "Automated FDS Input File Generation with fdsgeogen," Nov. 2015. (Cited on page 15)

[71] A. Meunders, L. Arnold, and B. Schröder, "Automated Generation and Evaluation of FDS Simulations for Optimizing Parameters with Dakota," (Magdeburg), Mar. 2015. (Cited on page 15)

[72] A. Meunders, L. Arnold, M. Spearpoint, and G. Baker, "Pyrolysis Parameter Optimization for the Modelling of Fire Spread with FDS," Feb. 2014. (Cited on page 15)

[73] A. Meunders, G. Baker, L. Arnold, B. Schröder, M. Spearpoint, and D. Pau, "Parameter Optimization and Sensitivity Analysis for Fire

Spread Modelling with FDS," (Australia), Society of Fire Protection Engineers (SFPE), Nov. 2014. (Cited on page 15)

[74] A. K. Prasad, "Particle image velocimetry," *Current Science*, vol. 79, July 2000. (Cited on pages 18, 19, 20, 21, 25, and 26)

[75] V. Weitbrecht, M. Muste, J.-D. Creutin, and G. H. Jirka, "Geschwindigkeitsmessungen mit Particle-Image-Velocimetry: Labor- und Feldmessungen," Tech. Rep. 90, Bundesanstalt für Wasserbau, 2007. (Cited on pages 18, 22, and 23)

[76] TOPAS, "Di-Ethyl-Hexyl-Sebacate," datasheet, Dresden. (Cited on pages 19, 36, and 74)

[77] A. Melling, "Tracer particles and seeding for particle image velocimetry," *Measurement Science and Technology*, vol. 8, p. 1406, Dec. 1997. (Cited on pages 19 and 23)

[78] M. Breuer, "Vertiefungspraktikum Strömungsmechanik: Particle Image Velocimetry," tech. rep., Helmut Schmidt Universität, Hamburg, Oct. 2014. (Cited on page 20)

[79] R. Hain, C. J. Kähler, and C. Tropea, "Comparison of CCD, CMOS and intensified cameras," *Experiments in Fluids*, vol. 42, pp. 403–411, Jan. 2007. (Cited on page 21)

[80] LaVision, "Phantom v series," datasheet, Oct. 2014. (Cited on page 22)

[81] F. Blumrich, "Optische korrelationsbasierte Messtechnik mittels zufälliger Punktemuster," 2009. (Cited on page 23)

[82] LaVision GmbH, "PIV Image Evaluation." `http://www.piv.de/piv/measurement_principle/page_1.php`. (Cited on page 24)

[83] J. Westerweel, *Digital Particle Image Velocimetry: Theory and Application.* PhD thesis, Delft University of Technology, Delft, June 1993. (Cited on pages 23, 24, and 26)

[84] U. Shavit, R. J. Lowe, and J. V. Steinbuck, "Intensity Capping: A simple method to improve cross-correlation PIV results," *Experiments in Fluids*, vol. 42, pp. 225–240, Dec. 2006. (Cited on page 24)

[85] F. Scarano and M. L. Riethmuller, "Iterative multigrid approach in PIV image processing with discrete window offset," *Experiments in Fluids*, vol. 26, pp. 513–523, May 1999. (Cited on pages 24 and 25)

[86] G. I. Roth and J. Katz, “Five techniques for increasing the speed and accuracy of PIV interrogation,” *Measurement Science and Technology*, vol. 12, p. 238, Mar. 2001. (Cited on page 25)

[87] A. Sciacchitano, B. Wieneke, and F. Scarano, “PIV uncertainty quantification by image matching,” *Measurement Science and Technology*, vol. 24, p. 045302, Apr. 2013. (Cited on pages 26 and 54)

[88] R. J. Adrian and J. Westerweel, *Particle Image Velocimetry.* No. 30 in Cambridge Aerospace Series, Cambridge ; New York: Cambridge University Press, 2011. (Cited on page 26)

[89] B. H. Timmins, B. W. Wilson, B. L. Smith, and P. P. Vlachos, “A method for automatic estimation of instantaneous local uncertainty in particle image velocimetry measurements,” *Experiments in Fluids*, vol. 53, pp. 1133–1147, July 2012. (Cited on page 26)

[90] A. Sciacchitano, D. R. Neal, B. L. Smith, S. O. Warner, P. P. Vlachos, B. Wieneke, and F. Scarano, “Collaborative framework for PIV uncertainty quantification: Comparative assessment of methods,” (Lisboa), July 2014. (Cited on page 26)

[91] D. R. Neal, A. Sciacchitano, B. L. Smith, and F. Scarano, “Collaborative framework for PIV uncertainty quantification: The experimental database,” (Lisboa), July 2014. (Cited on page 26)

[92] B. Wieneke, “Generic a-posteriori uncertainty quantification for PIV vector fields by correlation statistics,” (Lisboa), July 2014. (Cited on page 26)

[93] LaVision, “Introducing PIV uncertainty quantification (UQ) for 2D- and Stereo-PIV using the Correlation Statistics method,” Nov. 2014. (Cited on page 26)

[94] L. Rommeswinkel, “PIV-basierte Strömungsmessung im Modellmaßstab: Durchführung und Auswertung,” bachelor thesis, Bergische Universität Wuppertal, Wuppertal, Mar. 2015. (Cited on page 30)

[95] A. L. Tscherniewski, “PIV-basierte Strömungsmessung im Modellmaßstab: Simulation und Validierung,” bachelor thesis, Bergische Universität Wuppertal, Wuppertal, Mar. 2015. (Cited on page 30)

[96] A. Meunders, L. Arnold, A. Belt, and A. Hundhausen, “Velocity measurements of a bench scale buoyant plume applying particle image velocimetry (Preprint),” *International Journal of Heat and Mass Transfer*, 2016. (Cited on page 30)

[97] Promat International (Asia Pacific) Ltd., *Promat Handbook High Temperature Insulation.* Feb. 2011. (Cited on page 34)

[98] InnoLas Laser GmbH, “SpitLight PIV Compact - Double Rail Series - Datasheet,” 2013. (Cited on pages 35 and 36)

[99] TSI Incorporated, “Atomizer Aerosol Generator Model 3079,” 2012. (Cited on pages 36 and 38)

[100] LaVision, “Imager pro X 2M,” datasheet, Oct. 2013. (Cited on page 36)

[101] LaVision, “DaVis 8.2 Software Product Manual,” Nov. 2015. (Cited on page 40)

[102] LaVision, “DaVis 8.2 Imaging Tools Product Manual,” Feb. 2015. (Cited on page 42)

[103] “Python.org.” `https://www.python.org/`. (Cited on page 44)

[104] G. van Rossum, “Python Tutorial,” no. CS-R 9526, pp. 1 – 65, 1995. (Cited on page 44)

[105] Rössel Messtechnik GmbH, “Datasheet Pt100.” (Cited on page 50)

[106] Arkema Inc. - Altuglas International, “Plexiglas - Optical and Transmission Characteristics,” 2000. (Cited on page 52)

[107] LaVision, “DaVis 8.3 Software Product Manual,” Oct. 2015. (Cited on pages 54 and 103)

[108] B. Wieneke, “PIV uncertainty quantification from correlation statistics,” *Measurement Science and Technology*, vol. 26, no. 7, p. 074002, 2015. (Cited on pages 54 and 103)

[109] K. Noto, K. Teramoto, and T. Nakajima, “Spectra and Critical Grashof Numbers for Turbulent Transition in a Thermal Plume,” *Journal of Thermophysics and Heat Transfer*, vol. 13, pp. 82–90, Jan. 1999. (Cited on pages 62 and 63)

[110] D. Krause, “JURECA Jülich Research on Exascale Cluster Architectures,” Tech. Rep. FZJ-2015-04901, Jülich Supercomputing Center, 2015. (Cited on page 73)

[111] S. I. Woods, T. M. Jung, D. R. Sears, and J. Yu, “Emissivity of silver and stainless steel from 80 K to 300 K: Application to ITER thermal shields,” *Cryogenics*, vol. 60, pp. 44–48, Mar. 2014. (Cited on page 77)

[112] P. H. Thomas, “On the height of buoyant flames,” tech. rep., 1961. (Cited on page 103)

[113] P. H. Thomas and M. Law, “The Projection of Flames from Burning Buildings,” Tech. Rep. 921, 1972. (Cited on page 103)

[114] S. Yokoi, “Study on the Prevention of Fire-Spread Caused by Hot Upward Current,” tech. rep., 1960. (Cited on page 103)

[115] A. Meunders, C. Trettin, and F.-W. Wittbecker, “The capability of FDS to model flames and plumes emerging from compartment openings,” (Santander), Oct. 2012. (Cited on page 103)

Appendix A

Complete overview over open plume experiments

Table A.1: Complete overview of experimental runs with different heat inputs P_{HS}. Every line represents a recording of the entire plume, t_m is the duration of each measurement and f is the camera frame rate.

Name	t_m	f	P_{HS}	T_{HS}	T_1	T_2	T_3	T_4	T_5	T_6	T_7
	s	Hz	W	°C	°C	°C	°C	°C	°C	°C	°C
1.1	10	10	29.8	148.5	25.9	26.1	26.4	27.9	28.9	24.3	25.3
1.4	10	10	29.8	148.5	26.0	26.1	26.4	28.0	29.0	24.3	25.4
2.1.d	117	1	29.8	149.0	26.2	26.3	26.6	28.1	29.1	24.6	25.7
2.4.d	117	1	29.8	149.0	26.4	26.5	26.8	28.3	29.3	24.9	26.1
8.1	10	10	30.1	150.0	27.2	27.3	27.8	29.4	30.6	26.8	27.7
8.4	10	10	30.1	150.0	27.2	27.3	27.8	29.4	30.6	26.8	28.0
$\overline{x}$			29.9	149.2	26.5	26.6	27.0	28.5	29.6	25.3	26.4
σ			0.2	0.7	0.6	0.6	0.6	0.7	0.8	1.2	1.2
3.1	10	10	55.6	214.0	25.9	26.2	26.9	29.1	31.6	24.2	25.2
3.4	10	10	55.6	214.0	26.1	26.4	27.1	29.2	31.9	24.3	25.3
4.1.d	180	1	55.4	217.0	26.7	26.9	27.5	29.8	32.6	24.5	25.6
4.4.d	180	1	55.4	217.0	27.1	27.4	28.1	30.4	33.1	24.7	25.9
9.1	10	10	55.7	218.0	29.0	29.2	29.9	32.3	34.5	26.4	27.8
9.4	10	10	55.7	218.0	29.1	29.4	30.0	32.3	34.5	26.3	27.9
$\overline{x}$			55.6	216.3	27.3	27.6	28.2	30.5	33.0	25.1	26.3
σ			0.1	1.9	1.4	1.4	1.4	1.4	1.3	1.0	1.2
5.1	10	10	78.3	271.0	30.0	30.5	31.8	35.4	37.0	25.9	27.2
5.4	10	10	78.3	271.0	30.2	30.6	31.9	35.5	37.2	26.2	27.4
6.1.d	180	1	78.2	271.0	30.5	31.0	32.2	35.8	37.5	26.5	27.7
6.4.d	180	1	78.2	271.0	30.7	31.2	32.4	36.1	37.8	26.8	28.0
10.1	10	10	77.6	270.0	30.6	31.1	32.0	35.6	37.4	26.5	27.9
10.4	10	10	77.6	270.0	30.8	31.2	32.1	35.7	37.5	26.4	28.0
$\overline{x}$			78.0	270.7	30.5	30.9	32.1	35.7	37.4	26.4	27.7
σ			0.3	0.5	0.3	0.3	0.2	0.3	0.3	0.3	0.3
7.1	10	10	96.0	304.0	32.1	32.7	34.2	38.1	39.5	26.9	28.2
7.4	10	10	96.0	304.0	32.2	32.8	34.3	38.2	39.6	27.1	28.4
8.1.d	180	1	96.3	306.5	32.7	33.2	34.8	38.7	40.2	27.6	28.6
8.4.d	180	1	96.3	306.5	33.0	33.6	35.2	39.1	40.5	27.4	28.8
11.1	10	10	95.6	305.0	32.1	32.6	34.0	38.0	39.5	27.1	28.2
11.4	10	10	95.6	305.0	32.2	32.8	34.2	38.2	39.7	26.7	28.4
$\overline{x}$			96.0	305.2	32.4	33.0	34.4	38.4	39.9	27.1	28.4
σ			0.3	1.1	0.4	0.4	0.4	0.4	0.4	0.3	0.2

Appendix B

Complete overview over spill plume experiments

Table B.1: Complete overview over experimental runs of the spill plume setup with 80 mm door width. Every line represents a recording procedure at all four positions in the door. P_{HS} is the heat input, t_m is the duration of each measurement and f is the camera frame rate.

Name	Door mm	t_m s	f Hz	P_{HS} W	T_{HS} °C	T_1 °C	T_2 °C	T_3 °C	T_4 °C	T_5 °C	T_6 °C	T_7 °C	T_8 °C	T_9 °C	T_{10} °C	T_{11} °C
01.1	80	10	10	29.7	150.0	29.7	30.3	31.1	31.7	31.9	28.8	31.4	32.6	36.4	38.4	39.0
01.5	80	10	10	29.7	150.0	30.1	30.8	31.6	32.3	32.5	28.9	32.1	33.5	37.5	39.4	39.9
$\overline{x}$				29.7	150.0	29.9	30.6	31.3	32.0	32.2	28.9	31.8	33.0	36.9	38.9	39.4
σ				0.0	0.0	0.3	0.3	0.3	0.4	0.4	0.1	0.5	0.6	0.8	0.7	0.7
02.1	80	10	10	55.3	218.0	31.4	32.4	33.6	34.7	34.9	29.2	34.7	36.9	44.0	46.5	47.3
02.5	80	10	10	55.3	218.0	32.1	33.0	34.4	35.5	35.7	29.4	35.7	38.0	45.4	47.7	48.3
03.1	80	10	10	55.5	218.0	30.7	31.7	33.0	34.1	34.3	28.3	34.1	36.4	43.9	46.2	46.7
03.5	80	10	10	55.5	218.0	30.9	31.8	33.2	34.3	34.5	28.5	34.5	36.6	44.1	46.6	47.3
$\overline{x}$				55.4	218.0	31.3	32.2	33.6	34.7	34.9	28.8	34.7	37.0	44.3	46.8	47.4
σ				0.1	0.0	0.6	0.6	0.6	0.6	0.6	0.5	0.7	0.7	0.7	0.7	0.6
04.1	80	10	10	77.8	271.0	32.9	34.1	35.9	37.2	37.6	29.0	37.8	40.9	50.8	53.3	54.0
04.5	80	10	10	77.4	269.0	33.0	34.2	36.1	37.4	37.7	29.1	38.1	41.4	51.2	53.6	54.3
$\overline{x}$				77.6	270.0	32.9	34.1	36.0	37.3	37.6	29.1	37.9	41.2	51.0	53.5	54.2
σ				0.3	1.4	0.1	0.1	0.2	0.1	0.1	0.1	0.2	0.4	0.3	0.2	0.2

Continued on next page

Continued from previous page

Name	Door mm	t_m s	f Hz	P_{HS} W	T_{HS} °C	T_1 °C	T_2 °C	T_3 °C	T_4 °C	T_5 °C	T_6 °C	T_7 °C	T_8 °C	T_9 °C	T_{10} °C	T_{11} °C
05.1	80	10	10	96.6	306.0	36.6	38.0	40.4	41.7	42.3	30.4	43.9	47.3	58.8	61.8	62.7
05.5	80	10	10	98.1	306.0	36.8	38.2	40.5	42.0	42.5	30.5	44.1	47.7	59.2	61.9	62.7
06.1.d	80	180	1	96.0	306.0	37.0	38.4	40.8	42.2	42.8	30.7	44.4	47.8	59.1	62.3	63.1
06.2.d	80	180	1	96.0	307.0	37.3	38.7	41.0	42.6	43.1	31.0	44.6	48.1	59.6	62.7	63.6
$\overline{x}$				96.7	306.3	36.9	38.3	40.7	42.1	42.7	30.6	44.2	47.7	59.2	62.2	63.0
σ				1.0	0.5	0.3	0.3	0.3	0.3	0.3	0.3	0.3	0.3	0.3	0.4	0.4

Table B.2: Complete overview over experimental runs of the spill plume setup with 40 mm door width. Every line represents a recording procedure at all four positions in the door. P_{HS} is the heat input, t_m is the duration of each measurement and f is the camera frame rate.

Name	Door mm	t_m s	f Hz	P_{HS} W	T_{HS} °C	T_1 °C	T_2 °C	T_3 °C	T_4 °C	T_5 °C	T_6 °C	T_7 °C	T_8 °C	T_9 °C	T_{10} °C	T_{11} °C
07.1	40	10	10	29.5	151.0	27.7	28.2	28.8	29.4	29.5	26.7	30.1	31.6	34.1	36.0	37.1
07.5	40	10	10	29.5	151.0	27.8	28.3	28.9	29.5	29.6	26.7	30.3	32.0	34.4	36.5	37.4
08.1.d	40	180	1	29.6	150.0	27.9	28.4	29.1	29.7	29.8	26.5	30.5	32.2	34.7	36.8	37.8
$\overline{x}$				29.5	150.7	27.8	28.3	28.9	29.5	29.6	26.6	30.3	32.0	34.4	36.4	37.4
σ				0.0	0.6	0.1	0.1	0.1	0.2	0.2	0.1	0.2	0.3	0.3	0.4	0.3

Continued on next page

Continued from previous page

Name	Door mm	t_m s	f Hz	P_{HS} W	T_{HS} °C	T_1 °C	T_2 °C	T_3 °C	T_4 °C	T_5 °C	T_6 °C	T_7 °C	T_8 °C	T_9 °C	T_{10} °C	T_{11} °C
09.1	40	10	10	55.3	219.0	29.9	31.2	32.2	33.0	33.1	27.8	35.2	38.0	44.0	47.3	48.4
09.5	40	10	10	55.3	219.0	30.1	31.4	32.3	33.3	33.4	27.9	35.4	38.8	44.7	47.8	48.8
10.1.d	40	180	1	55.2	218.0	30.2	31.5	32.5	33.4	33.5	27.9	35.6	38.8	44.8	47.9	48.9
$\overline{x}$				55.2	218.7	30.1	31.3	32.4	33.2	33.4	27.9	35.4	38.5	44.5	47.7	48.7
σ				0.1	0.6	0.2	0.2	0.2	0.2	0.2	0.1	0.2	0.4	0.5	0.3	0.3
11.1	40	10	10	77.5	270.0	32.2	34.0	35.4	36.3	36.5	28.6	40.1	44.5	53.1	56.3	57.5
11.5	40	10	10	77.5	270.0	32.4	34.2	35.6	36.5	36.8	28.7	40.3	44.9	53.4	56.6	57.8
12.1.d	40	180	1	77.3	269.0	32.5	34.5	35.8	36.7	37.0	28.8	40.5	45.3	53.7	56.7	58.0
$\overline{x}$				77.4	269.7	32.4	34.2	35.6	36.5	36.8	28.7	40.3	44.9	53.4	56.5	57.8
σ				0.1	0.6	0.2	0.2	0.2	0.2	0.2	0.1	0.2	0.4	0.3	0.2	0.2
13.1	40	10	10	95.4	306.0	34.2	36.3	38.0	39.1	39.3	29.4	44.0	49.9	59.7	62.8	64.2
13.5	40	10	10	96.0	306.0	34.7	36.8	38.5	39.5	39.9	29.6	44.5	50.4	60.3	63.4	64.7
14.1.d	40	180	1	96.0	306.0	35.0	37.2	38.9	39.9	40.2	29.8	45.0	51.1	60.8	64.0	65.4
$\overline{x}$				95.8	306.0	34.6	36.8	38.5	39.5	39.8	29.6	44.5	50.5	60.3	63.4	64.8
σ				0.4	0.0	0.4	0.4	0.5	0.4	0.4	0.2	0.5	0.6	0.5	0.6	0.6

Band / Volume 19
Multiscale Modelling Methods for Applications in Materials Science
by I. Kondov, G. Sutmann (2013), 326 pages
ISBN: 978-3-89336-899-0
URN: urn:nbn:de:0001-2013090204

Band / Volume 20
High-resolution Simulations of Strongly Coupled Coulomb Systems with a Parallel Tree Code
by M. Winkel (2013), xvii, 196 pages
ISBN: 978-3-89336-901-0
URN: urn:nbn:de:0001-2013091802

Band / Volume 21
UNICORE Summit 2013
Proceedings, 18th June 2013 | Leipzig, Germany
edited by V. Huber, R. Müller-Pfefferkorn, M. Romberg (2013), iii, 94 pages
ISBN: 978-3-89336-910-2
URN: urn:nbn:de:0001-2013102109

Band / Volume 22
Three-dimensional Solute Transport Modeling in Coupled Soil and Plant Root Systems
by N. Schröder (2013), xii, 126 pages
ISBN: 978-3-89336-923-2
URN: urn:nbn:de:0001-2013112209

Band / Volume 23
Characterizing Load and Communication Imbalance in Parallel Applications
by D. Böhme (2014), xv, 111 pages
ISBN: 978-3-89336-940-9
URN: urn:nbn:de:0001-2014012708

Band / Volume 24
Automated Optimization Methods for Scientific Workflows in e-Science Infrastructures
by S. Holl (2014), xvi, 182 pages
ISBN: 978-3-89336-949-2
URN: urn:nbn:de:0001-2014022000

Band / Volume 25
Numerical simulation of gas-induced orbital decay of binary systems in young clusters
by A. C. Korntreff (2014), 98 pages
ISBN: 978-3-89336-979-9
URN: urn:nbn:de:0001-2014072202

Band / Volume 26
UNICORE Summit 2014
Proceedings, 24th June 2014 | Leipzig, Germany
edited by V. Huber, R. Müller-Pfefferkorn, M. Romberg (2014), iii, 60 pages
ISBN: 978-3-95806-004-3
URN: urn:nbn:de:0001-2014111408

Band / Volume 27
Automatische Erfassung präziser Trajektorien in Personenströmen hoher Dichte
by M. Boltes (2015), xii, 308 pages
ISBN: 978-3-95806-025-8
URN: urn:nbn:de:0001-2015011609

Band / Volume 28
Computational Trends in Solvation and Transport in Liquids
edited by G. Sutmann, J. Grotendorst, G. Gompper, D. Marx (2015)
ISBN: 978-3-95806-030-2
URN: urn:nbn:de:0001-2015020300

Band / Volume 29
Computer simulation of pedestrian dynamics at high densities
by C. Eilhardt (2015), viii, 142 pages
ISBN: 978-3-95806-032-6
URN: urn:nbn:de:0001-2015020502

Band / Volume 30
Efficient Task-Local I/O Operations of Massively Parallel Applications
by W. Frings (2016), xiv, 140 pages
ISBN: 978-3-95806-152-1
URN: urn:nbn:de:0001-2016062000

Band / Volume 31
A study on buoyancy-driven flows: Using particle image velocimetry for validating the Fire Dynamics Simulator
by A. Meunders (2016), xxi, 150 pages
ISBN: 978-3-95806-173-6
URN: urn:nbn:de:0001-2016091517

Weitere ***Schriften des Verlags im Forschungszentrum Jülich*** unter
http://wwwzb1.fz-juelich.de/verlagextern1/index.asp

IAS Series
Band / Volume 31
ISBN 978-3-95806-173-6

JÜLICH
FORSCHUNGSZENTRUM